

Structure of Dry Intrusions over western Europe on the basis of observational and model data

Master's Thesis in
Meteorology and Climate Physics
by

Christian Sperka

January 2024



INSTITUTE OF METEOROLOGY AND CLIMATE RESEARCH
KARLSRUHE INSTITUTE OF TECHNOLOGY (KIT)

Supervisor: Dr. Julian Quinting
Co-supervisor: Prof. Dr. Peter Knippertz



*This document is licenced under the Creative Commons
Attribution-ShareAlike 4.0 International Licence.*

Abstract

Dry Intrusions (DIs) are slantwise descending airstreams that descend from the upper troposphere towards the planetary boundary layer (PBL) (Raveh-Rubin, 2017; Ilotoviz et al., 2021). They are commonly associated with severe weather like wind gusts, heavy rain and thunderstorms (Young et al., 1987; Browning and Reynolds, 1994; Browning and Golding, 1995; Lagouvardos and Kotroni, 2000; James and Clark, 2003; Gao et al., 2010; Yang Shuai and Lingkun, 2009; Raveh-Rubin and Wernli, 2016) and are an important airflow component in extratropical cyclones (Danielsen, 1964; Carlson, 1980; Browning, 1997). In order to investigate DIs, among other dynamical processes, the measurement campaign NAWDIC was initiated and is currently scheduled for winter 2025/2026 around the North Atlantic, with station based measurements along the western European coastline (Grams et al., 2021; NAWDIC planning wiki). This study aims to quantify the climatological DI frequency over western Europe and to analyze the influence of DIs on the PBL. Further, the variety of the PBL modifications during DIs across different regions in western Europe and the representation of those modifications in numerical weather prediction models are investigated.

This thesis employs the Lagrangian DI definition of Raveh-Rubin (2017), namely the criterion of a pressure increase of at least 400 hPa in 48 hours. A scheme developed by Ilotoviz et al. (2021) that matches DIs with individual radiosonde stations is used to analyze DI impacts on the PBL. The DI data ranges from 1979 to 2022 and is matched with radiosonde data for the last several years from multiple stations across western Europe. In addition, DI case studies are analyzed in depth at the station Brest-Guipavas with DI trajectory, synop and ceilometer data. Moreover, a subset of radiosonde stations offers global ECMWF model background and analysis data which are compared to observations and examined for systematic biases during DI passages.

The climatological DI frequency reveals a strong seasonal dependence over western Europe, with the highest frequencies in winter and almost no DIs in summer. Highest numbers of DIs are generally observed over the North Atlantic and its coastlines with an additional area of enhanced DI frequencies over southern France, extending into the Mediterranean. The radiosonde profiles yield typical DI characteristics in the PBL like a cold, dry anomaly, a well-mixed PBL with potential instability and high wind speeds at the surface, although the high wind speeds occur usually before the DI onset. However, these signals vary in strength at different stations, probably due to local wind flow conditions around the stations that depend mostly on the surrounding topography. Case studies of individual DI events at the station Brest-Guipavas reveal that DIs can also be associated with anticyclones that cause a distinctly different PBL response, primarily due to the lack of a preceding cold front. In contrast, most DIs are associated with extratropical cyclones and thus with frontal systems. When DIs are coupled with a preceding cold front, the highest wind speeds typically occur in the preceding front. No consistent average biases during the passage of DIs are found in the model data. Possible DI-related biases at a station are outweighed by a general station specific bias that occurs during normal conditions.

These results highlight the wide variety of PBL impacts observed during the identified DIs, which is partially rooted in different dynamics of the DI trajectories themselves, depending on whether they are associated with an extratropical cyclone, an anticyclone or influenced by both. Therefore, clear signals of individual DIs may be obscured in an analysis of the average DI impacts. This underscores the importance of analyzing individual DI events, as planned during the measurement campaign NAWDIC, by conducting various detailed measurements, including ground-based measurements along the western European coastline.

Zusammenfassung

Dry Intrusions (DIs) sind schräg absinkende Luftströme, die von der oberen Troposphäre in Richtung der planetarischen Grenzschicht (PBL) absinken (Raveh-Rubin, 2017; Ilotoviz et al., 2021). Sie sind häufig mit unwetterartigen Windböen, Starkregen und Gewittern verbunden (Young et al., 1987; Browning and Reynolds, 1994; Browning and Golding, 1995; Lagouvardos and Kotroni, 2000; James and Clark, 2003; Gao et al., 2010; Yang Shuai and Lingkun, 2009; Raveh-Rubin and Wernli, 2016) und sind ein wichtiger Luftstrom in außertropischen Zyklonen (Danielsen, 1964; Carlson, 1980; Browning, 1997). Um DIs und andere dynamische Prozesse zu untersuchen wurde die Messkampagne NAWDIC gestartet, die derzeit für den Winter 2025/2026 rund um den Nordatlantik geplant ist, unter anderem mit bodengestützten Messungen entlang der westeuropäischen Küste (Grams et al., 2021; NAWDIC planning wiki). Ziel dieser Arbeit ist es, die klimatologische Häufigkeit von DIs über Westeuropa zu quantifizieren und den Einfluss von DIs auf die PBL zu analysieren. Darüber hinaus wird die Variabilität der PBL Veränderungen während DIs in verschiedenen Regionen Westeuropas und die Darstellung dieser Veränderungen in numerischen Wettervorhersagemodellen untersucht.

Diese Arbeit verwendet die DI Definition von Raveh-Rubin (2017), wonach ein Druckanstieg von mindestens 400 hPa in 48 Stunden als alleiniges Kriterium gilt. Die von Ilotoviz et al. (2021) entwickelte Methode der DI Zuordnung zu einzelnen Stationen wird benutzt, um die Auswirkungen von DIs auf die PBL zu analysieren. Die verwendeten DI Daten umfassen die Jahre 1979 bis 2022 und werden gemeinsam mit Radiosondendaten für die letzten mehreren Jahre von verschiedenen Stationen in Westeuropa analysiert. Darüber hinaus werden DI Fallstudien an der Station Brest-Guipavas mit DI Trajektorien-, Synop- und Ceilometerdaten eingehend analysiert. Zusätzlich stellt eine Gruppe von Radiosondenstationen globale ECMWF Modellhintergrund- und Analysedaten bereit, die mit Beobachtungen verglichen und auf systematische Fehler während DI Passagen untersucht werden.

Die klimatologische DI Häufigkeit zeigt eine starke jahreszeitliche Abhängigkeit über Westeuropa, mit den höchsten Häufigkeiten im Winter und fast keinen DIs im Sommer. Die höchste Anzahl an DIs wird im Allgemeinen über dem Nordatlantik und den westeuropäischen Küsten beobachtet, wobei ein zusätzliches Gebiet mit erhöhten DI Häufigkeiten über Südfrankreich liegt, das sich bis ins Mittelmeer erstreckt. Die Radiosondenprofile zeigen typische DI Merkmale in der PBL, z.B. eine kalte und trockene Anomalie, eine gut durchmischte PBL mit potenzieller Instabilität und höchste Windgeschwindigkeiten an der Oberfläche vor dem Beginn der DI an den meisten betrachteten Stationen. Diese Signale sind jedoch an den verschiedenen Stationen unterschiedlich stark ausgeprägt, was wahrscheinlich auf die lokalen Strömungsbedingungen um die Stationen herum zurückzuführen ist, die hauptsächlich von der umgebenden Topographie abhängen. Fallstudien einzelner DI Ereignisse an der Station Brest-Guipavas zeigen, dass DIs auch mit Antizyklen verbunden sein können, die eine deutlich andere PBL Reaktion hervorrufen, hauptsächlich aufgrund des Fehlens einer vorhergehenden Kaltfront. Dagegen sind die meisten DIs mit außertropischen Zyklonen und damit mit Frontensystemen verbunden. Wenn DIs mit einer vorausgehenden Kaltfront

gekoppelt sind, treten typischerweise die höchsten Windgeschwindigkeiten in der vorausgehenden Kaltfront auf. In den Modelldaten werden im Durchschnitt keine einheitlichen Abweichungen während des Durchgangs von DIs gefunden. Mögliche DI bedingte Abweichungen an einer Station werden durch eine allgemeine stationsspezifische Abweichung überwogen, die unter normalen Bedingungen auftritt.

Diese Ergebnisse verdeutlichen die große Variabilität an PBL Auswirkungen, die während der identifizierten DIs beobachtet wurde, was teilweise auf eine unterschiedliche Dynamik der DI Trajektorien selbst zurückzuführen ist. Diese hängt davon ab, ob die Trajektorien von einer außertropischen Zyklone, einer Antizyklone oder von beiden beeinflusst werden. Daher könnten in einer Analyse der durchschnittlichen DI Auswirkungen klare Signale einzelner DIs undeutlich werden. Dies unterstreicht die Bedeutung der Analyse einzelner Ereignisse, wie in der Planung der Messkampagne NAWDIC vorgesehen, mittels verschiedener detaillierter Messungen, einschließlich bodengestützter Messungen entlang der westeuropäischen Küste.

Contents

1	Introduction	1
2	Background Information	5
2.1	Dry Intrusion (DI) characteristics	5
2.2	DI influence on the planetary boundary layer	9
2.3	NAWDIC campaign	12
3	Data and Methods	15
3.1	DI data	15
3.1.1	DI outflow data	15
3.1.2	DI trajectory data	16
3.2	Radiosonde data	17
3.2.1	Observational data	17
3.2.2	Definition of DI events and classification	19
3.2.3	Background and analysis data	21
3.3	Synop data	21
3.4	Ceilometer data	22
4	Results	23
4.1	Representative DI case study at Brest	23
4.2	Climatological DI frequency in western Europe	34
4.3	Lower tropospheric structure during DIs at Brest	37
4.4	DI variability at Brest	45
4.4.1	DIs with lowest humidity at the surface	45
4.4.2	DIs with highest windspeeds at the surface	52
4.5	Lower tropospheric structure during DIs at other stations	61
4.6	Evaluation of numerical weather prediction model data	72
5	Conclusion and Discussion	81
	Bibliography	85

1 Introduction

Dry Intrusions (DIs) are slantwise descending airstreams that descend from the upper troposphere towards the planetary boundary layer (PBL) (Raveh-Rubin, 2017; Ilotoviz et al., 2021). They have been identified as an important airflow component in extratropical cyclones (Danielsen, 1964; Carlson, 1980; Browning, 1997). As such, they overrun surface fronts and create potential instability (Browning, 1997), causing climatologically more intense cold fronts (Catto and Raveh-Rubin, 2019; Raveh-Rubin and Catto, 2019). Further, DIs are commonly associated with severe weather like wind gusts, heavy rain and thunderstorms (Young et al., 1987; Browning and Reynolds, 1994; Browning and Golding, 1995; Lagouvardos and Kotroni, 2000; James and Clark, 2003; Gao et al., 2010; Yang Shuai and Lingkun, 2009; Raveh-Rubin and Wernli, 2016). Additional modifications of the PBL during DIs include enhanced surface fluxes and a higher PBL altitude (Raveh-Rubin, 2017; Ilotoviz et al., 2021). Due to their connection to high impact weather, DIs possess a high relevance for the prediction and improved understanding of those events. Therefore, the measurement campaign NAWDIC (North Atlantic Waveguide, Dry Intrusion, and Downstream Impact campaign) was initiated and is scheduled for winter 2025–2026 in western Europe (Grams et al., 2021; NAWDIC planning wiki). The NAWDIC campaign serves as an additional motivator for this study to analyze DI impacts especially around the northwest coast of Europe, the area where station based measurements as part of the NAWDIC campaign will most likely be conducted.

In order to analyze DI characteristics overall and not only specific case studies, Raveh-Rubin (2017) created the first global Lagrangian climatological dataset of DIs, by implementing the DI definition of a pressure increase of at least 400 hPa during 48 hours. This allowed the determination of DI frequencies and physical properties along their trajectories across different regions of the globe. However, due to the coarse global approach, variations inside the analyzed regions are not accounted for. Ilotoviz et al. (2021) focused on PBL changes during DIs, using the DI identification scheme developed by Raveh-Rubin (2017) and local observations of a station in the Azores. Grounded in this previous work, the following research questions remain open and will be analyzed in this study:

1. What is the climatological occurrence frequency of DIs over western Europe and how variable is it over different regions and seasons?
2. How is the PBL modified during the passage of DIs and how does it depend on the large-scale circulation?
3. How does the DI influence on the PBL vary across different regions in western Europe?

4. Is the modification of the PBL during DIs accurately represented in numerical weather prediction models or can systematic biases be identified?

To answer these questions, the same approach as in Raveh-Rubin (2017) is employed to identify DIs, but the wind fields used to calculate the trajectories are based on ERA5 data (Bell et al., 2021), instead of ERA-Interim (Dee et al., 2011) as in Raveh-Rubin (2017). Available DI data ranges from 3 January 1979 to 31 December 2022 and DI frequency over western Europe is calculated for different months and seasons, for example the average frequency of DIs in the winter months (Figure 1.1). The identified DIs are then matched with radiosonde data from several stations operated by Meteo-France and ECMWF with an analogical methodology as in Ilotoviz et al. (2021). Researching question 2 is the main focus of this thesis. To this end, synop and ceilometer data at the station Brest-Guipavas are used for in depth analyses of specific DI events that illustrate the variability of the PBL modifications during DIs. Moreover, detailed DI trajectory data provides information about large-scale circulation and the evolution of multiple variables along the trajectories. This station was selected due to ceilometer data availability, location and DI signal reasons. Located near the North Atlantic coast, Brest could be relevant for the NAWDIC campaign and average lower tropospheric structure at Brest reveals more pronounced DI characteristics than at other stations. Radiosonde observations at the other stations present the opportunity to analyze DI characteristics at different regions over western Europe with varying environments. The radiosonde dataset from ECMWF also provides background and analysis data from the global ECMWF model, parallel to the observations. This allows the identification of possible biases during DIs.

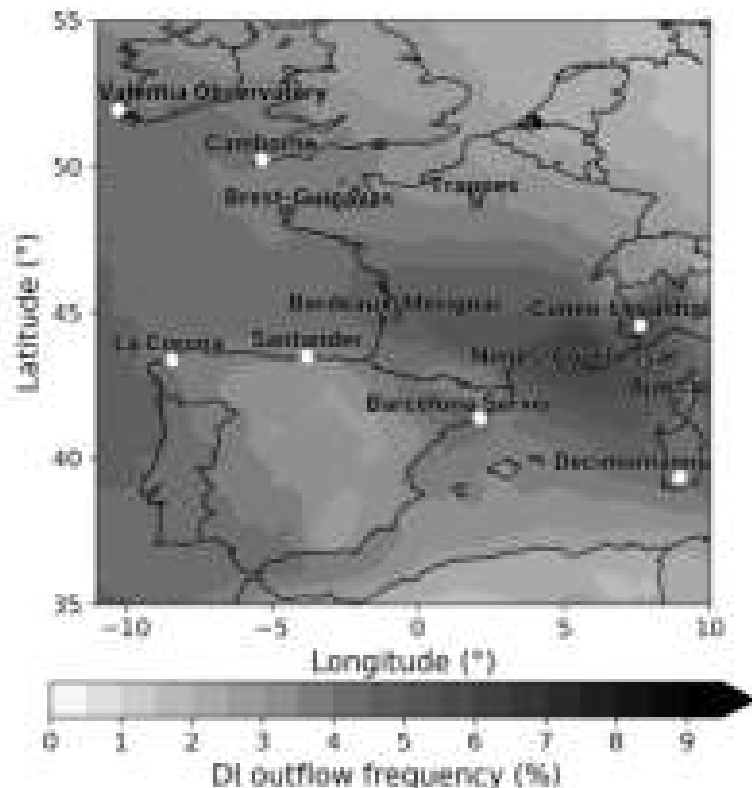


Figure 1.1: Average DI frequency in winter months December, January and February (DJF) from 3 January 1979 to 31 December 2022 across western Europe. Radiosonde stations with data from Meteo-France are marked blue and stations with data from ECMWF white.

This thesis is structured as follows: Chapter 2 provides background information about DI characteristics, the PBL and the DI influence on the PBL. Additionally, the most relevant points of the planned NAWDIC campaign for this study are described. In chapter 3, the utilized data and methods are explained in detail. The results are presented in chapter 4, starting with a representative DI case study at the radiosonde station Brest to illustrate the data and typical DI behaviour. Afterwards, the climatological DI frequency across western Europe is analyzed, followed by an investigation of the average lower tropospheric structure during DIs at Brest. Found variability in this structure is explored in the next section by investigating two different DI events, one associated with the lowest specific humidity and one with the highest windspeeds at the surface. Thereafter, the focus is the regional variability in the lower tropospheric structure during DIs at other radiosonde stations across western Europe before the last section evaluates numerical weather prediction model data during DIs. The last chapter summarises the main findings and offers suggestions for future research.

2 Background Information

This chapter provides background information on DIs and the PBL, starting with a summary of the characteristics of DIs (section 2.1). The section thereafter investigates the DI effect on the PBL (section 2.2) and the last section 2.3 in this chapter informs about the scheduled NAWDIC campaign.

2.1 Dry Intrusion (DI) characteristics

Descending dry airstreams have been the subject of research for over six decades, with the studies from Reed (1955) and Reed and Danielsen (1958) being the first to identify descending stratospheric air near the jet stream and suggesting their connection with rapid cyclogenesis. Due to low moisture content, descending dry airstreams can often be identified as dry slots in satellite imagery (Browning, 1993). The resulting dark bands in the water vapor imagery have been referred to as 'dry intrusions' (Rodgers et al., 1985; Young et al., 1987). The term 'dry intrusion' (DI) is also used to refer specifically to the flow of dry air of upper-level origin (e.g. Browning and Golding (1995)) and will be used in this way for the rest of this study. Dry air flows with the stratosphere as origin attracted interest for mixing processes and chemical transport between the stratosphere and the troposphere (Danielsen (1968), Škerlak et al. (2014)). Furthermore, deep stratospheric intrusions were found to modulate the ozone air surface concentrations in the western U.S. (Lin et al., 2015) and in the Alps (Stohl et al., 2000). DIs move in general equatorward, transporting dry air to lower latitudes and, if the DIs descend from the stratosphere, they also transport high potential vorticity (PV) air (Raveh-Rubin, 2017). Consequently, extratropical DIs that extend to the tropics can also intensify monsoon convection over west Africa (Roca et al., 2005). Moreover, DIs have been associated with synoptic environments that created wildfires in southern Australia (Mills, 2008), in the northeastern U.S. (Pollina et al., 2013) and Southern California (Langford et al., 2015).

The flow of DI trajectories interacting with extratropical cyclones and overrunning surface fronts was depicted as early as 1964 by Danielsen (1964). DIs have been identified as an important airflow component in extratropical cyclones (Carlson, 1980). Browning (1997) analyzed DIs in extratropical cyclone development in great detail, discussing DI airflows in both confluent and diffluent flow types of cyclogenesis (Figure 2.1). Both models include a primary and secondary warm conveyor belt (W1 and W2), a cold conveyor belt (CCB), a dry intrusion and different fronts.

In the confluent flow type, a bent back surface warm front is plotted conventionally with a part of the bent-back front plotted as a cold front. Between this cold front and the main surface cold front,

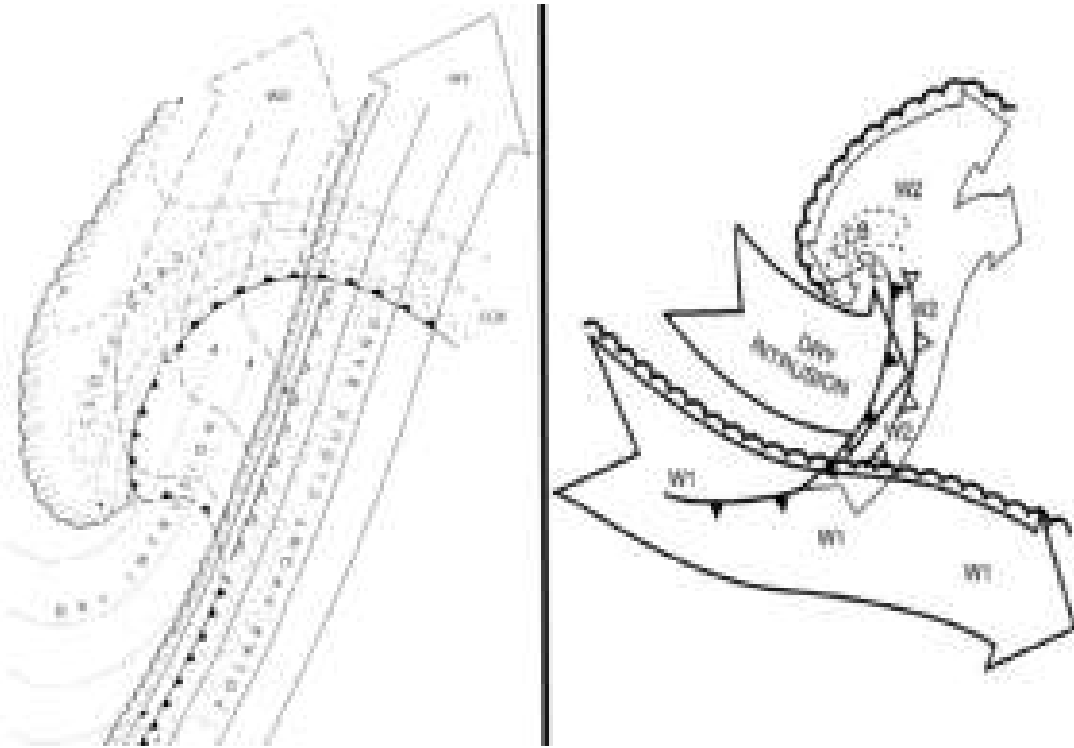


Figure 2.1: Extratropical cyclone structure with included DI. Left: Confluent flow type. Right: Diffluent flow type. The cyclone center (L) travels towards the top right. W1 and W2 denote the primary and secondary warm conveyor belt, respectively, and CCB the cold conveyor belt. Green stippled areas in the left figure indicate rain. Adapted from Browning (1997).

a diffuse surface cold front is drawn with widely spaced cold front symbols, located in front of W2 and both are overrun by the dry intrusion. This overrunning of the moist flow with dry air causes potential instability, producing an upper level cold front at the edge of the dry intrusion, plotted with open frontal symbols. Precipitation at the surface, marked as green stippled areas, can be seen along the left side of W1 and ahead of the bent back surface warm front. Due to the dry intrusion, a dry slot emerges between those two main areas of rain.

In the diffluent flow type, the two warm conveyor belts flow in diverging directions and the secondary warm conveyor belt W2 is overrun by the dry intrusion over a broader front. This creates an upper cold front at the leading edge of the dry intrusion. These cyclone models show that DIs can both inhibit and trigger precipitation, which is supported by numerous other studies. DIs can suppress precipitation by undercutting rain formed in a warm conveyor belt (Browning and Golding, 1995) and by evaporating falling rain (Browning and Roberts, 1994). However, DIs may also trigger convection when they overrun moist air flows, resulting in severe weather like strong winds, precipitation and thunderstorms (Young et al., 1987; Browning and Reynolds, 1994; Browning and Golding, 1995; Lagouvardos and Kotroni, 2000; James and Clark, 2003; Gao et al., 2010; Yang Shuai and Lingkun, 2009; Raveh-Rubin and Wernli, 2016).

After Wernli and Davies (1997) suggested a Lagrangian approach to obtain more detailed information of flow features in extratropical cyclones, Lagrangian based analyses were utilized for the investigation of DIs (Wernli, 1997; Stohl, 2001; Škerlak et al., 2014; Raveh-Rubin, 2017). In a case study, Wernli (1997) applied a selection criterion for dry descending trajectories of a descent of at

least 350 hPa in 48 h and used further criterions based upon the PV evolution over the course of the trajectories to discriminate stratospheric and tropospheric air. Results showed that the strongest descent occurred for tropospheric air parcels and that descent of trajectories originating from the stratosphere was weaker. Stohl (2001) presented a 1 year climatology of airstreams, based on an ensemble of forward trajectories in the Northern Hemisphere and identified DIs along with other types of airstreams. He concluded that DI activity is highest in winter and lowest in summer, with maxima over western North America and East Asia. Using a refined Lagrangian methodology, Škerlak et al. (2014) compiled a global 33-year climatology of stratosphere-troposphere exchange (STE) with a subset of deep STE, where stratospheric air reaches the PBL within 4 days or vice versa. They found the storm tracks over the North Atlantic, North Pacific, Southern Ocean and mountain ranges in the subtropics to be the main regions of STE.

The first global Lagrangian climatological dataset of DIs was constructed by Raveh-Rubin (2017) for the years 1979–2014 to quantify the global occurrence and variability of DIs. To calculate trajectories, Raveh-Rubin (2017) used the Lagrangian analysis tool (LAGRANTO) (Sprenger and Wernli, 2015), based on ERA-Interim data (Dee et al., 2011). For every 6 h time step between 00 UTC 4 January 1979 and 18 UTC 31 December 2014, 48 h long forward trajectories were initiated from a three-dimensional grid. Then the DI trajectories were selected according to a specific criterion. Raveh-Rubin (2017) tested different descent criteria to identify DIs, varying between a pressure increase of 350 and 500 hPa in a time window ranging between 24 and 96 h and found the criterion of a descent of 400 hPa in 48 hPa to be the most suitable. Reasons for this choice include computational considerations based on the typical number of selected trajectories and a synoptic time scale of descent that yields coherent sets of trajectories. Thus, this criterion is used to compile the global Lagrangian DI climatology, based on ERA-Interim data. This criterion is also used here and the present thesis therefore builds strongly on the work of Raveh-Rubin (2017). Additionally, a criterion that identified DIs with a stratospheric origin was also employed, requiring all DI trajectories to have PV values of at least 2 PVU during a 48 h time period before their descent. Moreover, to analyse thermodynamical and dynamical processes of DIs, multiple variables were traced along the selected DI trajectories. Results of Raveh-Rubin (2017) confirm the findings in Stohl (2001) that DI frequency is highest in winter and almost negligible in summer, especially in the Northern Hemisphere.

The evolution of the different variables traced along the DI trajectories is shown in Figure 2.2. It reveals large variability of the pressure (p) values of DIs. The vertical positions of 90 % of DIs differ by approximately 300 hPa at every time step during their descent, whereas this variability is almost doubled at time –48 h and even larger at time 120 h. This large variability might be partly explained by the fact that the DI data in the figure encompasses regional and seasonal differences in addition to the variability in a coherent set of DI trajectories. The potential temperature θ shows a small diabatic cooling of a few Kelvin, which is likely the result of radiative cooling or evaporation of water in the dry air mass (Raveh-Rubin, 2017). As observed in the specific humidity q , the amount of moisture in the DIs increases after 18–24 h. Based on the evolution of relative humidity RH, Raveh-Rubin (2017) suggests two typical stages of DI descent. In the first stage that lasts until 18 to 24 h, the DIs warm adiabatically and thereby cause minimal levels of RH. In the second stage, mixing with the moist PBL occurs, which increases the RH again and causes a large variability in

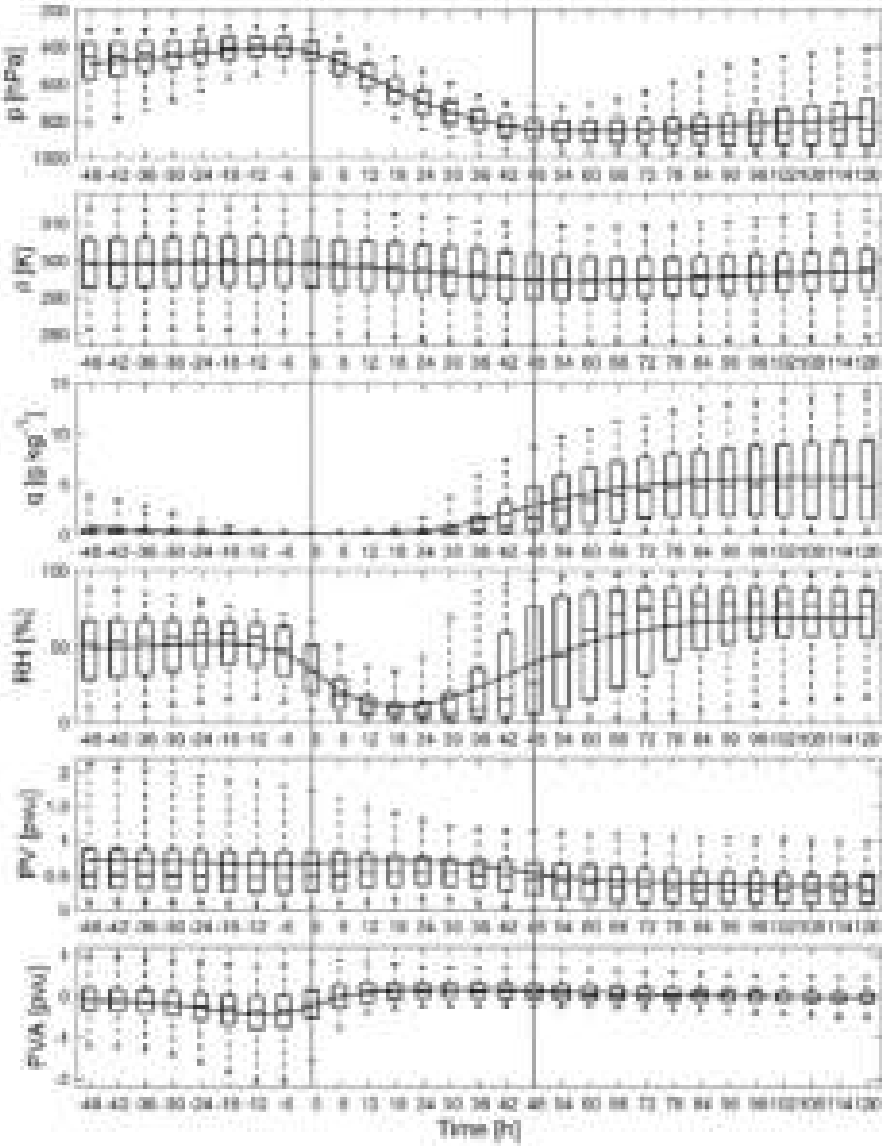


Figure 2.2: Evolution of p (hPa), θ (K), q (g kg^{-1}), RH (%), PV (PVU) and PVA (PVU) [PV and PVA values in the Southern Hemisphere are multiplied by -1] along DI trajectories. The box marks the median and interquartile range, the whiskers mark 5% and 95% of the distributions and the solid line connects the means from each time step. From Raveh-Rubin (2017).

RH, due to differences in the intensity of mixing and various characteristics of the PBL. The PV values, with Southern Hemisphere values multiplied by -1, are mostly below 2 PVU, indicating that most DIs originate and stay in the troposphere. While many studies focus on investigating the effects of stratospheric intrusions (e.g. Browning and Reynolds (1994); Danielsen (1968); Itoh and Narazaki (2016); Langford et al. (2015); Lin et al. (2015); Stohl et al. (2000)), the observed PV values reveal that those make up only 1.2 % of all DIs, with the remaining DIs all descending from below the tropopause. However, this small subset of DIs showed 50 % stronger PBL height anomalies on average than the overall DI impact. In addition to the PV, the potential vorticity anomaly PVA, with respect to the local long-term monthly climatology, is also traced along the trajectories. The PVA values show that high PV anomalies with magnitudes larger than 1 PVU

are rare. Raveh-Rubin (2017) notes that before the descent of the DIs most values are negative, indicating a location of DIs within a ridge in the upper troposphere.

2.2 DI influence on the planetary boundary layer

In the last section, the PBL was already mentioned briefly, for example the impact of DIs on the surface or that DIs mix with PBL air, but with an emphasis on the DIs themselves. In this section, the PBL is the main focus. The PBL is the part of the troposphere that is directly influenced by the surface and responds to surface forcings in about an hour or less (Stull, 1988). Mechanisms that shape the characteristics of the PBL include the exchanges of heat, momentum, moisture and chemical constituents between the surface and the free atmosphere (Ilotoviz et al., 2021). Since these processes vary greatly over different regions, Medeiros et al. (2005) identified several different PBL regimes. They found large land-sea contrasts, with dry convective boundary layers dominating over land and stratocumulus-topped boundary layers most common over ocean. Further, large diurnal and seasonal variations over land and virtually no diurnal variations over the global oceans were identified (Medeiros et al., 2005; von Engeln and Teixeira, 2013). Seasonal variations were found to lead to higher PBL heights in summer over land regions such as North Africa, the Middle East, North America, and Australia (von Engeln and Teixeira, 2013). According to McGrath-Spangler and Denning (2013), a higher PBL altitude in summer occurs over land regions in general, including Europe. In contrast, the Northern Hemisphere storm track regions over the oceans experience their maximum PBL height during winter, when cold air is advected over the warm western boundary currents, leading to an unstable lower atmosphere and resulting in the formation of a deep PBL (Medeiros et al., 2005). Idealized diurnal variations over land for midlatitudes in summer were illustrated by Lee (2018) in Figure 2.3.

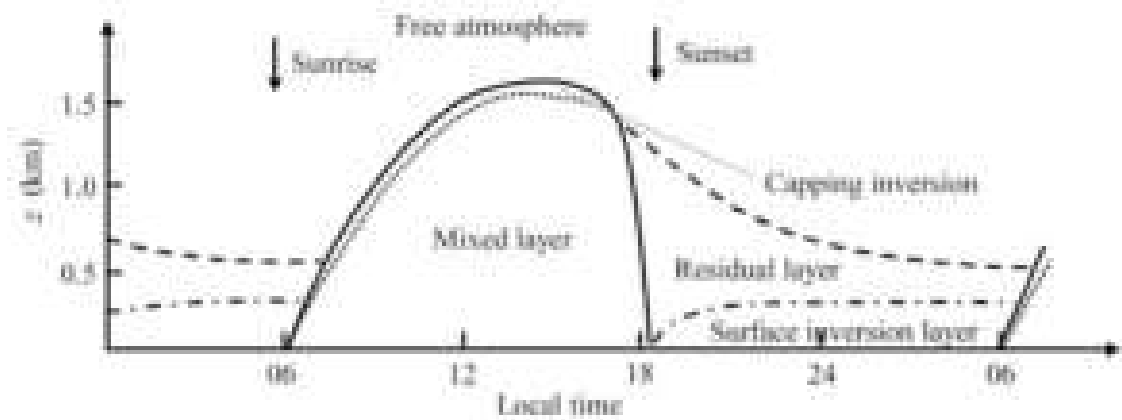


Figure 2.3: Diurnal evolution of the atmospheric boundary layer for midlatitudes in summer (Lee, 2018).

During nighttime, a surface inversion layer is present with a residual layer above. After sunrise, erosion of the surface inversion layer begins and a mixed layer starts forming. The mixed layer grows in altitude with time and reaches its maximum depth of approximately 1.5 km around 4 pm local time. As solar radiation decreases due to the approaching sunset, the buoyancy generation of turbulent kinetic energy weakens and the mixed layer collapses rapidly around 6 pm. At this

time, the residual layer, which can be identified from a uniform potential temperature profile (Lee, 2018), is quite deep and slowly shrinks due to mixing with tropospheric air from above and surface air from below. Shortly before sunset, a negative surface sensible heat flux emerges and marks the onset of the surface inversion layer. This inversion layer grows much slower than the mixed layer, reaching a depth of about 300 m at midnight. These large diurnal variations highlight the importance of analyzing PBL characteristics daytime-dependent over land.

However, the pattern in Figure 2.3 is often superimposed by synoptic weather events, such as fronts associated with extratropical cyclones. Cold fronts coupled with DIs behind them were associated with strong wind and precipitation impact in case studies (Carr and Millard, 1985; Browning and Reynolds, 1994). Globally, Catto and Raveh-Rubin (2019) found all cold fronts associated with DIs to have an increased impact, since those fronts featured a stronger temperature gradient, a higher average precipitation and a larger area. DIs were also associated with enhanced surface sensible and latent heat fluxes (Raveh-Rubin, 2017; Raveh-Rubin and Catto, 2019), demonstrating large influence on the PBL.

Ilotoviz et al. (2021) analyzed the impact of DIs on the PBL with measurements from the Atmospheric Radiation Measurements (ARM) program Eastern North Atlantic (ENA) site (Wood et al., 2015) on the island Graciosa in the Azores. Datasets include automatic surface weather station, ceilometer and radiosonde data for the months January, February and December of the years 2016–2018. For the identification of DIs, they used the Lagrangian DI criterion and same methodology as in Raveh-Rubin (2017). The front identification scheme from Catto and Raveh-Rubin (2019) is additionally applied. Moreover, they defined different classes to investigate the DI impact on the PBL before, during and after a DI. With a time resolution of 6 h, every time step before a DI was termed as "Pre-DI front", since all DIs at the station were preceded by detectable fronts. If at least one DI trajectory was detected within a radius of 1 ° around the station with a pressure level of at least 700 hPa at a time step, then that time step was defined as "DI". Time steps up to 24 h after the last occurrence of a DI were classified as "Post-DIs", provided that no front or DI occurs during this period. The remaining time steps are divided into "Non-DI fronts", when a cold front at the side was detected without a DI behind it, and "Non-DIs", when neither a cold front nor a DI was detected at the site. An analogous methodology is applied in this thesis, therefore some results of the study of Ilotoviz et al. (2021) will be described in detail in the following.

The 12-hourly available radiosonde profiles with 10 m vertical interpolation are averaged for each class and shown in Figure 2.4 up to 5 km. Those vertical profiles of the PBL include temperature, potential temperature θ , equivalent potential temperature θ_e , specific humidity q , relative humidity RH and wind speed. The temperature profiles (Figure 2.4, a) reveal the presence of a marine inversion layer during DIs and Post-DIs, with the DIs featuring the highest inversion located above 1.5 km and a sharp temperature gradient above this level. Compared to DIs, the Post-DI inversion altitude decreases to 1.2–1.3 km and weakens, but is still stronger and at a higher altitude than at Non-DIs. Interestingly, the coldest temperatures in the lowest 3 km occurs under DIs. An almost constant profile of θ (Figure 2.4, b) is observed during DIs in the lowest 1.5 km. This suggests a deeper well mixed layer in comparison to the other categories. Large differences among the classes emerge in the θ_e profile (Figure 2.4, c) due to the combined effect of temperature and

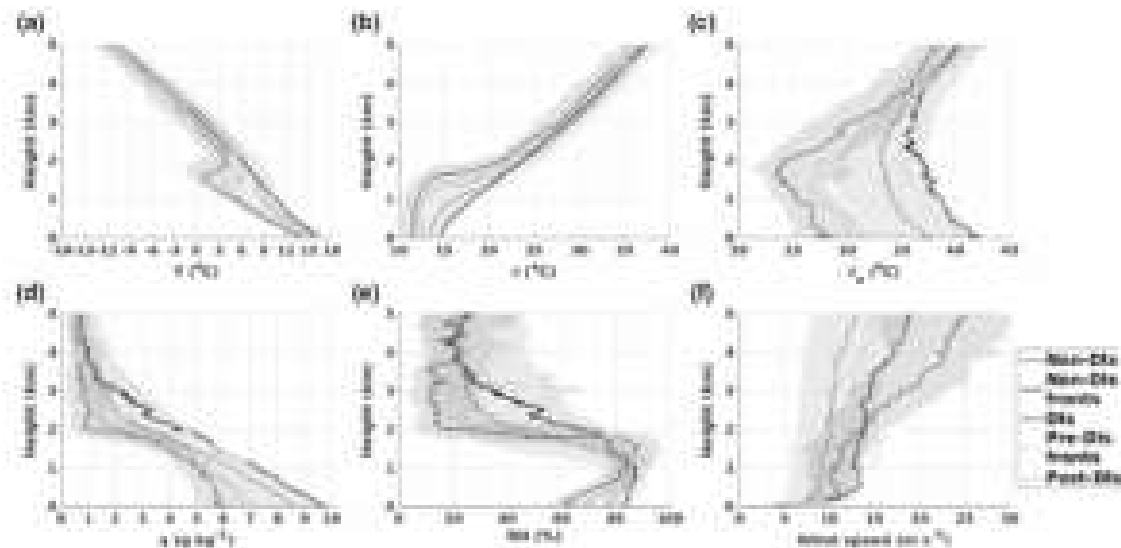


Figure 2.4: Vertical profiles of (a) air temperature, (b) potential temperature, (c) equivalent potential temperature, (d) water vapor mixing ratio, (e) relative humidity, and (f) horizontal wind speed based on radiosondes. The solid lines are the median value at each height and category, and the shaded area marks the range between the 25th and 75th percentiles of the Non-DIs and DIs distributions. From Ilotoviz et al. (2021).

humidity. Non-DI fronts feature the highest values, whereas DIs show the smallest values. The vertical gradient of θ_e indicates potential instability below the inversion layer. Above this layer, θ_e increases most strongly under DIs, reducing the difference between classes substantially above 3.5–4 km. Specific humidity profiles (Figure 2.4, d) reveal DIs as the driest class throughout the atmospheric column, with a dry free troposphere above 2 km and a sharp rise below it, caused by mixing with the moister PBL air. In contrast, Pre-DI fronts display almost the same amount of moisture as Non-DI fronts and more than during Non-DIs, while Post-DIs present the second lowest specific humidity values after DIs. DI and Post-DI relative humidity (Figure 2.4, e) increases up to the inversion layer, whereas the other categories stay relatively constant. Above that layer all classes experience a reduction in RH, but the sharpest drop occurs during DIs from >80 % to about 15 %. Following the relative humidity values, DIs are expected to feature the lowest cloud fraction below 1 km and the highest at 1.5 km, since DIs exhibit the lowest and highest relative humidity values at those heights, respectively. This assumption is verified by additional measurements from a vertical pointing Doppler cloud radar operating at 35 GHz. According to those measurements, cloud fraction peaked with almost 40 % at 1.5 km during DIs, while also the lowest cloud fraction below 1 km was found during DIs. Wind speed profiles (Figure 2.4, f) show the largest values near the surface in front-related categories, followed by DIs. However, the DI wind speed increases strongly with height and becomes the strongest wind speed above 3 km, while the other classes show only a slight increase. The weakest wind speeds occur during Non-DIs.

Based on the radiosonde wind data, Ilotoviz et al. (2021) created wind direction histograms at 50 m above ground level (Figure 2.5) to analyze the prevailing wind directions during the different classes. The normal climatological wind directions (Non-DIs, a) are south and south-westerly, while the front-related classes (b,c) both show south-west as the dominant wind direction. However, during DIs (d) the wind direction shifts to north-westerly with almost no southerly winds. The largest



Figure 2.5: Wind directions histograms from radiosondes at 50 m above ground level for the categories (a) Non-DIs, (b) Non-DIs fronts, (c) Pre-DIs fronts, (d) DIs, and (e) Post-DIs. From Ilotoviz et al. (2021).

variability of wind directions is observed in Post-DIs (e) with winds from almost all directions, though the large peak in south-westerly winds suggests a slow return to climatology.

Ilotoviz et al. (2021) conclude, also based on further results, that DIs influence the ENA site for about 21 % of the time, when Pre- and Post-DI stages are also considered. During DI events, a substantial deepening of the well-mixed PBL was observed, coupled with changes in cloud, precipitation and thermodynamic properties. Strong surface sensible and latent heat fluxes occurred during DIs, induced by a substantially cooler and drier lower troposphere.

2.3 NAWDIC campaign

NAWDIC is a planned international field campaign around the North Atlantic, currently scheduled for winter 2025/2026. As this time lies in the distant future during the writing of this study, the information presented here, based on the NAWDIC planning wiki website and an international science plan (Grams et al., 2021), is preliminary and can still change. The acronym NAWDIC stands for “North Atlantic Waveguide, Dry Intrusion and Downstream Impact Campaign” and was originally defined for the planned German component with the High Altitude and Long Range Research Aircraft (HALO). HALO is currently scheduled for January/February 2026. However, several components have been added by different groups, which are planned as independent measurement campaigns, but are coordinated under the umbrella of NAWDIC. Motivations for NAWDIC are centered around the desire to obtain detailed observations of the mesoscale tropopause structure, the dry intrusion airstream, the PBL and high impact weather (HIW). These observations are intended to improve the understanding of these phenomena, their relation and ultimately their modelling and forecasting.

The idealized schematic in Figure 2.6 from Grams et al. (2021) illustrates the atmospheric features desired for investigation, e.g. a dry intrusion, along with the potential deployment of research aircraft and ground-based observational facilities. Near North America, a NOAA/NCAR aircraft is planned to provide airborne observations. In the vicinity of Europe, airborne observations from HALO are combined with a ground-based observation network that is expected to be operated in impacted countries across western Europe, for example France and UK.

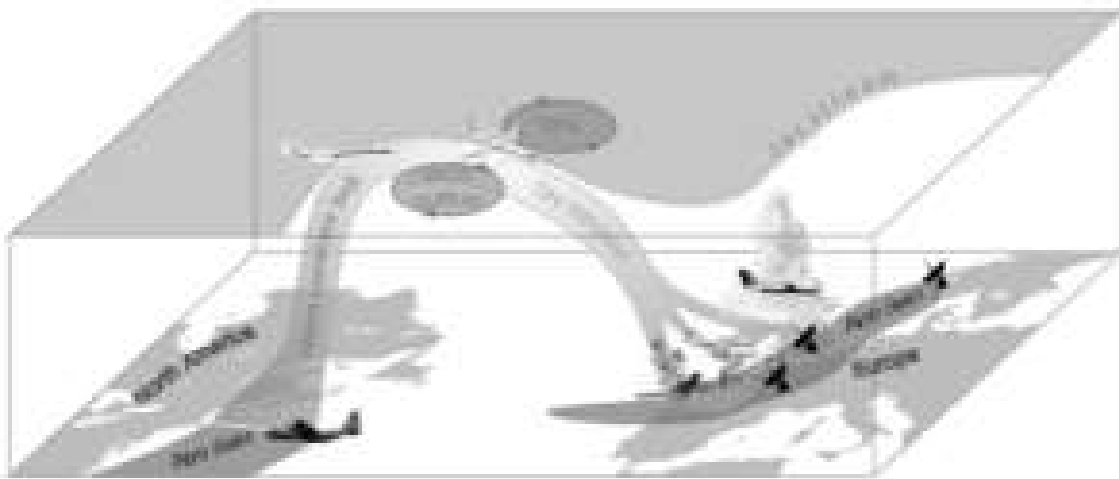


Figure 2.6: Idealized schematic showing the potential deployment of research aircraft and ground-based observational facilities during NAWDIC (Grams et al. (2021))

The research in NAWDIC is organised around 3 scientific goals (Grams et al., 2021). The first goal is to obtain measurements of the mesoscale structure of the cloud and wind field, especially near jet streaks and in locations where the DI descent begins. The second goal focuses on improved understanding of momentum transport into the PBL and its connection to severe wind gusts and convection. To achieve this, high-resolution observations of wind, temperature, all phases of water, cloud microphysical properties where DIs reach the top of the PBL, the PBL, the surface and cold fronts are planned. Lastly, the third goal is to analyze surface fluxes in the cold sector and near fronts of extratropical cyclones to quantify their importance in model representations for HIW and cyclogenesis, especially over the ocean. Therefore, detailed measurements of turbulent heat, moisture and momentum fluxes at the air-sea interface are envisaged.

This thesis is partially motivated by NAWDIC and part of preparatory work for the campaign. To find optimal positions for the ground-based measurement network intended to observe DI impacts, DI frequencies over western Europe are analyzed. However, this thesis is overall independent of NAWDIC and the main motivation is the scientific relevance of DIs, as elucidated in the previous sections. In addition to the DI frequencies, the passage of DIs at several stations over western Europe and the associated impacts on the PBL are explored. To achieve this, similar methodologies as in Raveh-Rubin (2017) and Ilotoviz et al. (2021) are employed. The utilized data and methods are explained in detail in the following chapter.

3 Data and Methods

3.1 DI data

Two different datasets of DI data are employed in this study, both provided by Shira Raveh-Rubin from Weizmann Institute of Science in Israel. The first dataset contains gridded DI outflow data and the second dataset includes DI trajectories and various variables along them.

3.1.1 DI outflow data

The DI data ranges from 3 January 1979 00 UTC to 31 December 2022 21 UTC and is available 3-hourly at a grid spacing of 0.5° for the whole globe. DIs are identified with the Lagrangian analysis tool LAGRANTO (Sprenger and Wernli, 2015) that calculates trajectories using ERA5 gridded wind field data (Bell et al., 2021). Like all trajectory tools, LAGRANTO solves numerically the trajectory equation

$$\frac{Dx}{Dt} = u(x), \quad (3.1)$$

where x is the position vector and u is the three-dimensional wind vector. One important feature of LAGRANTO is the possible selection of trajectories based on objective criteria. Every 3-hours, 48 h long forward trajectories are started from a three-dimensional grid, with 60 km horizontal spacing and 30 hPa vertical spacing above the 600 hPa level. This is a crucial difference to the DI data in the paper of Raveh-Rubin (2017), where a starting grid with 80 km horizontal and 20 hPa vertical resolution above 600 hPa was used, based on ERA-Interim data (Dee et al., 2011). As DI selection criterion, a pressure increase of at least 400 hPa during 48 h is applied, similarly as in Raveh-Rubin (2017). Since a trajectory could also fulfill this DI criterion in a timeframe shorter than 48 h, an additional filter is employed which deletes those trajectories. With this approach, multiple trajectories representing the same air mass are prevented. In this dataset, DI outflow denotes DI trajectories that are located below 700 hPa and the number of those DIs per km^2 is stored in the grid.

A randomly selected DI event on 3 January 2020 at 15 UTC over western Europe illustrates the DI outflow data (Figure 3.1). At this timestamp, a broad swath of DIs below 700 hPa is observed that stretches from northern Germany over southern UK and northern France towards the open Atlantic. Within this DI outflow area the numbers of DIs per square kilometer vary from smaller than 0.001 to 0.005. However, for the DI definition that is explained in detail in 3.2, all values above 0 are equally important.

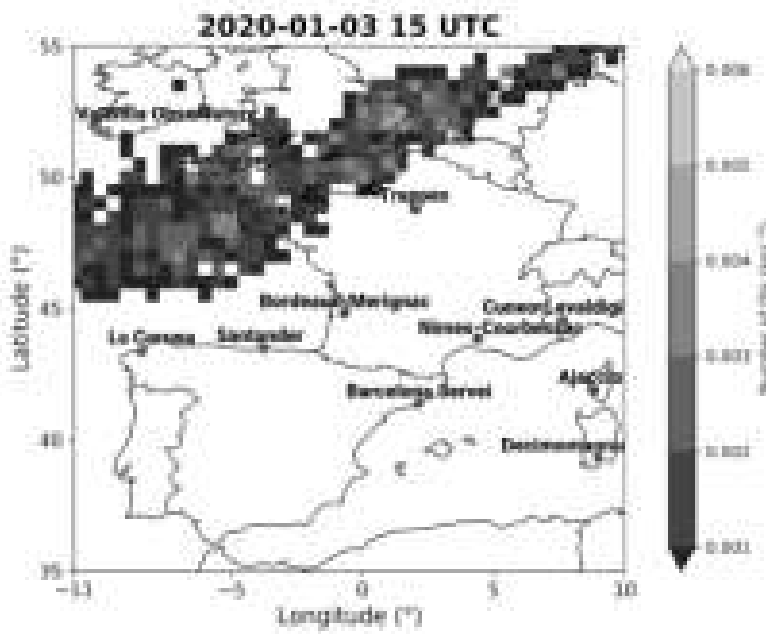


Figure 3.1: DI density on 3 January 2020, 15 UTC over western Europe. The labelled radiosonde stations from Meteo-France are marked blue and the stations from ECMWF are marked brown.

3.1.2 DI trajectory data

The raw DI trajectory data contains the location of the individual trajectories and different variables that are traced along the trajectory from 1 January 2016 to 31 December 2022 in 3-hourly intervals. This timeframe is selected to match the radiosonde data availability in order to provide additional information about DIs for specific case studies. The DI trajectories that were selected with LAGRANTO, are expanded 48 h backward and 72 h forward in time, with the 48 h descending period in the center. This yields a total DI trajectory length of 7 days. However, the start of the descending period is assigned time 0, so that all trajectories start at the relative time -48 h and end at +120 h, with available data in 3-hour intervals. Each 3-hourly data file contains all DI trajectories that started their descending period at the same real time, therefore the number of DI trajectories in each file varies.

The location of each trajectory is specified by latitude, longitude and pressure, with a precision of two decimal places for latitude and longitude in degrees and zero decimal places for pressure in hPa. Moreover, the variables that are traced along the trajectories can be divided into three-dimensional and two-dimensional fields. The three-dimensional fields include the specific humidity, potential temperature, potential vorticity, relative humidity and velocity and are interpolated to the trajectory location at every time step. In contrast, the two-dimensional variables that consist of the surface sensible and surface latent heat fluxes, are interpolated only to the horizontal location of the DI trajectory.

To identify DIs at the radiosonde stations on the basis of raw DI trajectory data, multiple criteria are implemented. The first criterion is about the selected time period. Since the trajectories were

extended to 7 days, with 2 days added before their descending period and 3 days after, only the 48 h descending period is selected. Secondly, to be defined as a DI at a station, the trajectory needs to be located inside a 1° radius of the respective station. Finally, the trajectory is required to exhibit pressure values of at least 700 hPa. This pressure criterion is selected to be equal to the DI outflow dataset. However, the location and pressure criterion need to be fulfilled both at the same time for at least one timestep in the descending period. If at least one timestep of a trajectory fulfills all criteria, then the whole DI trajectory is classified as a DI at a particular station.

Naturally, it would be easiest to group the trajectories of each 3-hourly file when analyzing a DI occurrence at a particular station. But since the trajectories in each file are only sorted by the start of the descending period, the time when they reach the station with a pressure value of at least 700 hPa may differ for each trajectory. Therefore, the trajectories are grouped according to their first arrival time inside the 1° radius of the analyzed station with a pressure value of at least 700 hPa. This approach allows the combination of trajectories from multiple data files. One disadvantage from this method is that the real time now refers to the time when the trajectories first fulfill all criterions and not the start of the descending period at relative time 0. This time when the trajectories first reach the station may happen at different relative times, mostly between 36 – 48 h, though this point is also valid if trajectories were grouped by data file. To achieve that the real time when the trajectories reach the station occurs at the same relative trajectory time for all trajectories, the relative times would need to be redefined. However, this would in turn mix the descending period at different relative times. Therefore, the arrival time of DI trajectories at the station at different relative times is accepted, in order to keep the descending period of all selected trajectories between 0 and 48 h relative time.

Additionally, ERA5 data (Bell et al., 2021) of mean sea level pressure are utilized for the analysis of DI trajectories, to provide information about the large scale circulation. Only the mean sea level pressure data at the time when all trajectories first fulfill the station and pressure criteria are selected. This implies that the ERA5 pressure data is only valid for the trajectories when they are close to the station and should not be used for interpretation near the start or end of the trajectories, as the trajectories span 7 days in total.

3.2 Radiosonde data

3.2.1 Observational data

Radiosonde data are retrieved from Meteo-France (2023) for the winter period between 1 December 2016 to 31 December 2022 with a frequency interval of 12 hours. This period is chosen because by the end of 2016 radiosonde data were archived in BUFR format at higher vertical resolution. The selected sounding stations from Meteo-France are Brest-Guipavas (ID 07110), Bordeaux-Mérignac (ID 07510), Nîmes-Courbessac (ID 07645), Trappes (ID 07145) and Ajaccio (ID 07761) (Figure 3.1). Radiosonde measurements include pressure, altitude, temperature, dew point, wind direction and wind speed. Although the vertical resolution can be quite irregular, the usual vertical resolution

amounts to values of 10 to 15 m. The radiosonde data is interpolated to a regularly spaced vertical grid with a height interval of 10 m and a height up to 5 km. Additional quantities are then calculated from this data, namely potential temperature, equivalent potential temperature, specific humidity and relative humidity. Some of these variables allow an estimation of the PBL height based on their vertical gradients. According to von Engeln and Teixeira (2013), the PBL height is determined as the minimum gradient of relative or specific humidity and the maximum gradient of potential temperature.

Potential temperature is the temperature a parcel of air attains when it is adiabatically brought down to a standard reference pressure, which is set to 1000 hPa in this study. Potential temperature is conserved for dry adiabatic processes and the vertical gradient describes the static stability of an unsaturated atmosphere (Kurz, 1990). A potential temperature increasing with height indicates stable conditions, a constant potential temperature neutral and a decreasing potential temperature unstable stratification.

Equivalent potential temperature is the temperature a parcel of air attains when it is lifted dry adiabatically to its lifting condensation level, then pseudo-wet adiabatically until all water vapor in the air parcel condensed and dropped out, and finally brought down dry adiabatically to 1000 hPa (Bolton, 1980). In contrast to potential temperature, the equivalent potential temperature is also conserved for saturated vertical motions. The vertical gradient of the equivalent potential temperature yields the same information about stability as the potential temperature gradient, but in a saturated atmosphere (Kurz, 1990). A situation in which the equivalent potential temperature decreases with height in an unsaturated layer of air is called potentially unstable, as it would become unstable if lifted to its saturation level.

Additional radiosonde data for 7 stations are provided by David Lavers from ECMWF, encompassing a period from 1 December 2019 to 28 February 2023 with the same frequency interval of 12 hours as the radiosonde stations from Meteo-France. Due to missing DI data after the start of 2023, only the radiosonde measurements until 31 December 2022 are utilized in this study. The 7 new radiosonde stations are spread over several countries and include Camborne (ID 03808) in England, Valentia Observatory (ID 03953) in Ireland, La Coruna (ID 08001), Santander (ID 08023) and Barcelona Servei (ID 08190) in Spain, Cuneo-Levaldigi (ID 16113) and Decimomannu (ID 16546) in Italy. ECMWF radiosonde measurements include, beside the positional parameters latitude, longitude and pressure, the variables temperature, specific humidity, zonal wind component and meridional wind component.

However, the geometric height in m is missing. Accordingly, we calculate the geometric height based on the pressure values. For this purpose, the following formula is used:

$$h = \frac{288.15 \text{ K}}{0.0065 \frac{\text{K}}{\text{m}}} \cdot \left(1 - \left(\frac{p(h)}{p_0} \right)^{\frac{1}{5.255}} \right) + h_0. \quad (3.2)$$

with the pressure values $p(h)$, the first pressure value in the radiosonde measurements p_0 and the station height h_0 . The temperature value of 288.15 K and the temperature gradient of $0.0065 \frac{\text{K}}{\text{m}}$ are from the international standard atmosphere. A few spot-checks with the Meteo-France data,

which provides both pressure and altitude in m, revealed a difference in 5 km height of about ± 100 m, i.e. a relative difference of 2%. This is considered acceptable but needs to be noted during the comparison of the different station sets. Similarly to the Meteo-France radiosonde data, the ECMWF dataset's vertical resolution is non equidistant. In general, the vertical resolution is lower than in the Meteo-France dataset with only about 25–30 m and up to 40 m vertical resolution above 2–3 km.

3.2.2 Definition of DI events and classification

For the analysis of DI effects on the boundary layer, DI-related classes are defined analogous to Ilotoviz et al. (2021). Since the radiosonde data is only available in 12 hour intervals, the definitions of Pre- and Post-DIs are changed slightly for this study. The timestep 12 hours before a DI is defined as Pre-DI and the timestep 12 hours after a DI as Post-DI, as shown in Figure 3.2. In case a DI event lasts several timesteps, only the timesteps 12 hours before and after that event are classified as a Pre-DI and Post-DI, respectively. Timesteps are classified as DIs for a particular station, if gridded DI outflow density values larger than zero occur within a radius of 1° around that station. All other timesteps are assigned the term Non-DI. A special case occurs if a timestep of a radiosounding is located between two DI timesteps, then it is classified both as a Pre- and Post-DI.

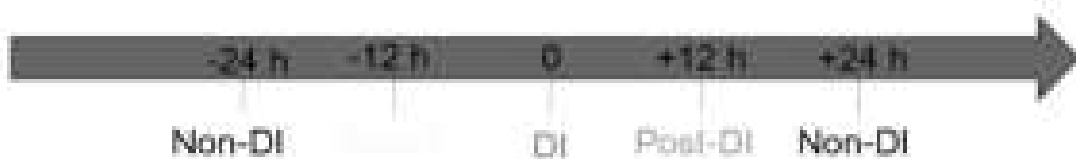


Figure 3.2: DI classification scheme.

A caveat arising from this identification method is the large frequency interval of 12 hours that is necessary due to the frequency of radiosonde ascents. This implies that DI values at a station in the 3-hourly DI outflow data at e.g. 9 or 15 UTC, are not considered and the radiosonde ascent at 12 UTC would be classified as Non-DI, if there is no DI at 12 UTC and no DI 12 hours before and after in the station radius.

The radius of 1° around each station can include a different number of grid points, due to the comparably coarse resolution of 0.5° grid spacing of the DI outflow data, as Figure 3.3 illustrates with the station radii in yellow.

In contrast to a round circle, the radii at the stations have various shapes and a different amount of grid points that form the radius. The radius around Brest-Guipavas occupies the least amount of grid points with 11 grid points in total, whereas the radii of Ajaccio and Valentia-Observatory occupy the most grid points with 14 in total. Naturally, the total radius area in km^2 also depends on the latitude, since the distance between two longitude points decreases with latitude. Therefore, the station Ajaccio possesses the largest radius with an area of approximately 32200 km^2 , whereas Brest owns the smallest radius with about 22600 km^2 . Since the number of total DIs per square kilometer is not considered in the DI classification scheme, a larger radius should also lead to more

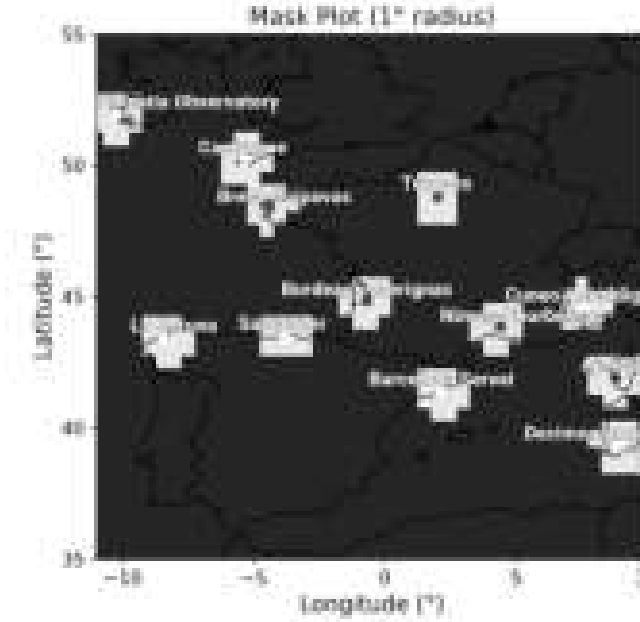


Figure 3.3: All radiosonde stations with their respective 1° radius colored in yellow. Meteo-France stations are marked with a blue dot and ECMWF stations with a white dot.

identified DI events. Therefore, the radius area size needs to be considered in a station comparison of the absolute number of identified DI regimes.

In order to observe changes in the PBL during the occurrence of DIs, the radiosonde data is divided into 00 UTC and 12 UTC data, since the PBL typically displays a large diurnal variability that could significantly influence the results. One disadvantage of this method might be that DI events are separated because the Pre and Post-DIs at 00 UTC are related to DIs occurring at 12 UTC, but are compared with DIs at 00 UTC.

At a later stage of this thesis, radiosonde data from ECMWF was additionally obtained for the station Brest, allowing a direct comparison of the ECMWF and Meteo-France radiosonde dataset at Brest. For this comparison, the typical depiction of vertical profiles is used (e.g. Figure 4.9), but based on data from 1 December 2019 to 31 December 2022 from both datasets. The median lines of the different classes defined above reveal a surprisingly good agreement overall (not shown). In general, the median lines based on ECMWF data appear slightly smoother, probably due to the coarser vertical resolution than in the Meteo-France data. Above 1.5 km the ECMWF medians are increasingly shifted upward, compared to the Meteo-France medians, but only about 100 m at most. Interestingly, the temperature and humidity values directly at the station surface deviate more from the adjacent values above in the Meteo-France dataset, as they feature for example colder temperatures at 00 UTC, indicating a stronger temperature inversion, and warmer temperatures at 12 UTC.

3.2.3 Background and analysis data

In addition to the observations, the radiosonde measurements from the ECMWF dataset also offer background and analysis data based on the global ECMWF model parallel to the observation of the four variables, at the same pressure levels. The Integrated Forecast System (IFS) from ECMWF that provides this data changes over time with different cycles. At the start of the ECMWF dataset on 1 December 2019, IFS Cycle 46r1 was active and during the utilized measurement period the model cycles 47r1-3 were implemented (ECMWF, 2023a). However, all active models use a horizontal resolution of 9 km and 137 vertical levels, with 41 levels in the considered lowest 5 km of the troposphere. This data is interpolated to the location of the radiosonde at every observation.

Since the employed data assimilation method 4D-Var is a complex topic, only the basic concepts of data assimilation like background and analysis will be described, because those quantities are provided in the radiosonde data. For a detailed description of each model version the reader is referred to the IFS documentation (ECMWF, 2023b).

The background or first guess is an a priori estimate of the model state, which is generated by a short-term model forecast (Bouttier and Courtier, 2002). Alternatively, the background information can also be a climatology or be generated from the output of a previous analysis. The analysis is a model representation of the true state of the atmosphere at a given time and is produced by utilizing a collection of observed values provided by observations of the true state (Bouttier and Courtier, 2002). This data allows the identification of model biases by subtracting the model data from the observation. Krüger et al. (2023) investigated the influence of radiosonde observations on the sharpness and altitude of the midlatitude tropopause in the ECMWF IFS. They used the terms innovation and residual to refer to the departures of the observations (O) from the first guess or background (B) and the analysis (A), respectively. These terms are calculated as follows:

$$\text{Innovation} = O - B, \text{Residual} = O - A. \quad (3.3)$$

This approach of Krüger et al. (2023) is utilized in this thesis to compare the radiosonde observations with the data from the global ECMWF model.

3.3 Synop data

Synop data is retrieved from NOAA's integrated surface database (ISD) for the different radiosonde stations (NOAA, National Centers for Environmental Information, 2018b). This data is formatted in a special synop code which is explained in the corresponding documentation (NOAA, National Centers for Environmental Information, 2018a). From this data, the following hourly surface observations are selected: wind direction, wind speed, air temperature, dew point temperature, pressure and precipitation. This data is used to find special DI events, namely the DI events associated with the highest wind speed, highest specific humidity and lowest specific humidity values at the surface, by matching those values with previously determined DI occurrences at the considered station. Further, this data provides important surface observations during selected DI

events and is therefore an integral part of the illustration of DI impacts on surface weather. Since DI frequency is generally highest in the analyzed region in winter, only the data for the months December, January and February is analyzed.

3.4 Ceilometer data

Ceilometer data measured with the ceilometer model CL31 (firmware version 205) was obtained from the CEDA archive (Centre for Environmental Data Analysis (CEDA), 2023) for Brest. This data is available from 8 February 2019 to 20 February 2021. However, often a few days are missing in the selected period. Thus, this data is suitable for analyzing certain DI events but not for creating an average over the whole period. Data files are available approximately every 5 minutes, with one file containing observations for one timestamp, reaching from the surface height up to about 7500 m with a vertical resolution of roughly 30 m. According to the variable description in the data files, the Ceilometer CL31 uses a laser with a wavelength of 910 nm. Further, the data files contain a variable called 'quality_flag' with possible values of 0, 1, 2 and the associated meanings are OK, do not use and to be defined, respectively. Thus, only the data assigned with quality flag 0 is used. Unfortunately, the processing steps that led to this quality flag are unknown.

Ceilometer measurements are influenced by various factors. The CL31 model has internally generated artefacts from the instruments software that could create differences in backscattered attenuation compared to other sensors (Emeis et al., 2009). The backscattered signal in ceilometer measurements consists of contributions from actual atmospheric attenuation, but also from the background signal associated with scattered solar radiation and an instrument-related background signal (Cao et al., 2013). Despite those few caveats, ceilometers are widely used to identify cloud base heights, rainfall and boundary layer dynamics like mixing height and the formation of residual layers (Kotthaus et al., 2016). The height of the mixing layer or PBL can be identified as a shift from a relatively strong backscatter inside the mixed layer to a lower backscatter above it, since the mixed layer air generally has a higher burden of scattering aerosols than the air above (Steyn et al., 1999; Münkel et al., 2007).

4 Results

This chapter presents the results by starting with a representative DI case study at Brest (section 4.1). Afterwards, the climatological DI frequency in western Europe is analyzed in section 4.2 before the following section 4.3 focuses on the lower tropospheric structure during DIs at Brest. Reasons for this strong focus on Brest include the suitable location for NAWDIC and the availability of ceilometer measurements. However, the crucial factor is that Brest exhibits on average the most pronounced DI characteristics of any station in the longer Meteo-France dataset, though with a large variability. This variability is investigated in the next section 4.4. Section 4.5 analyzes the variability of the DI influence on the PBL at other stations. Lastly, section 4.6 evaluates the numerical weather prediction model data during DIs.

4.1 Representative DI case study at Brest

Based on typical DI features discussed in the background information chapter about the DI characteristics and influence on the PBL, a characteristic DI event in Brest is selected to analyze and illustrate the data and methods. The DI event started on 20 February 2020 at 15 UTC and lasted to the next day at 12 UTC at Brest. Trajectory data show how the DIs start their descent shortly after passing the southern tip of Greenland (Figure 4.1).

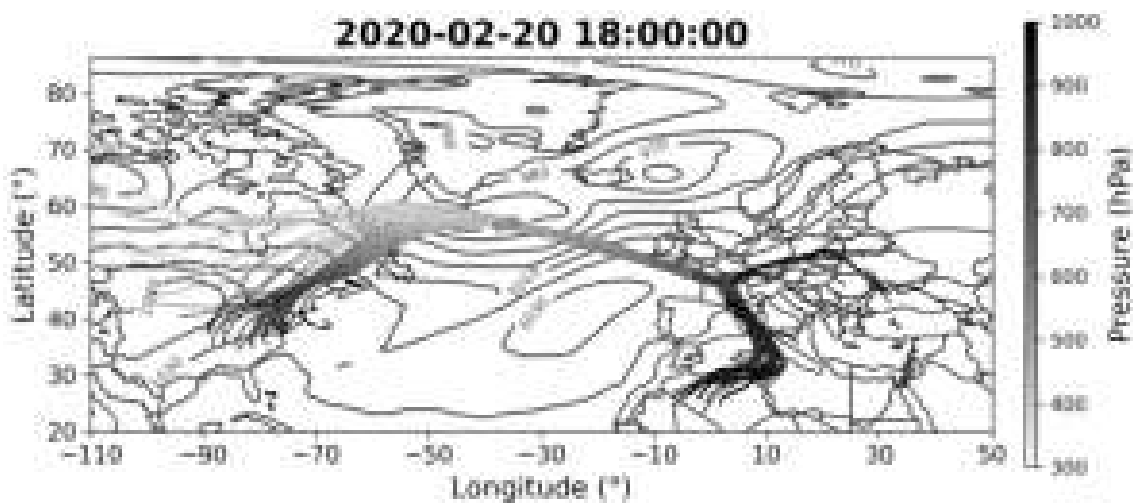


Figure 4.1: DI trajectories reaching Brest on 20 February 2020 at 18 UTC, colored according to their pressure in hPa. Additionally, isobars show the mean sea level pressure valid for the same time in blue and pressure values in hPa. The green circle marks the 1 ° radius around Brest.

The trajectories exhibit a large variety of starting points, reaching from southeast of New York City towards central Canada. A large cluster of trajectory starting points over the eastern U. S. exhibits a pressure greater than 800 hPa, while the other trajectories over Canada start rather high with pressure values below 500 hPa. The lower cluster ascends over the United States and Newfoundland before it eventually unites with the higher cluster at the southern tip of Greenland at a pressure level of about 400–500 hPa. Then, the trajectories descend on the way to the station Brest and reach it with a pressure level of about 800 to 900 hPa on 20 February 2020 at 18 UTC. Brest is marked in the trajectory Figure 4.1 by a green circle with a radius of 1 °. An interesting feature is the close resemblance of the lower trajectory cluster pathway with the idealized pathway in the NAWDIC schematic (Figure 2.6). After passing Brest, the trajectories continue descending while moving into central France, where they split in two clusters. The larger cluster turns southeastward and moves over the Mediterranean into northern Africa, where most trajectories reach a pressure level greater than 1000 hPa over Algeria. The smaller cluster consists of trajectories that are already located at higher pressure levels over central France close to 1000 hPa as they turn northeastward and move over Germany before turning southeastward over Poland and finally ending over the Black Sea.

Beside the DI trajectories, isobars of mean sea level pressure at the time when the trajectories first reach Brest with a pressure level above 700 hPa are also shown. It is important to note that those isobars are only valid for the timestamp 18 UTC on 20 February 2020, when the trajectories are inside the 1 ° radius around Brest. Since the trajectory data covers 7 days overall, namely 2 days before the descent, the 2 day long descent of at least 400 hPa and 3 days after the descent, only the trajectory flow close to the station Brest should be interpreted with the surface pressure value. This segmentation of the trajectories suggests that the trajectories move with high velocity during the first four days as they travel a longer distance and slow down substantially during the last 3 days after passing Brest. During the first four days, the trajectories are transported with the upper-level jet at about 400–500 hPa, which is associated with higher wind speeds than at the surface levels. The displayed isobars show a pronounced Azores high and a distinct low just east of Iceland. These large air pressure contrasts cause a region of strong pressure gradient just north of the trajectories when they reach Brest. Over southern Europe, the pressure gradient is weaker, explaining the lower velocity displayed by the trajectories. The curvature of the trajectories can also be explained by the isobars. As the large cluster is influenced more by the Azores high, it exhibits an anticyclonic curvature, whereas the smaller cluster is more influenced by the deeper pressure values northward caused by the Icelandic low.

This DI trajectory arrival time in Brest is selected because it features by far the most trajectories and different trajectory flows, compared to the other timestamps of this DI event at Brest. The timestamp before with trajectory arrival in Brest at 15 UTC mostly shows trajectories with the origin in Canada and the final destination in Algeria. In contrast, timestamps from 18 UTC until the end of the DI event in Brest at 12 UTC on the next day start also mostly in Canada but end up deep inside Russia as the trajectories are caught in a strong west-northwest flow after passing Brest (not shown). This is caused by an expansion of the Azores high with the 1030 hPa isobar moving over central France from 00 UTC 21 February 2022 onwards, creating a more zonal flow around Brest.

Additionally to the trajectory location and pressure level, multiple other variables are also traced along the trajectories and are depicted as a function of relative time in Figure 4.2. Time 0 h marks the start of the descending period and it is important to note that the trajectories do not necessarily reach Brest only at time 48 h, but could also arrive a few hours earlier, since the criteria for the trajectories involve to be inside the 1 ° radius around Brest with a pressure value of at least 700 hPa during the descending period (0 to 48 h). This implies that at relative time 0 h, the actual time could be different for different trajectories, since 18 UTC on 20 February 2020 is the time when all criteria are first fulfilled.

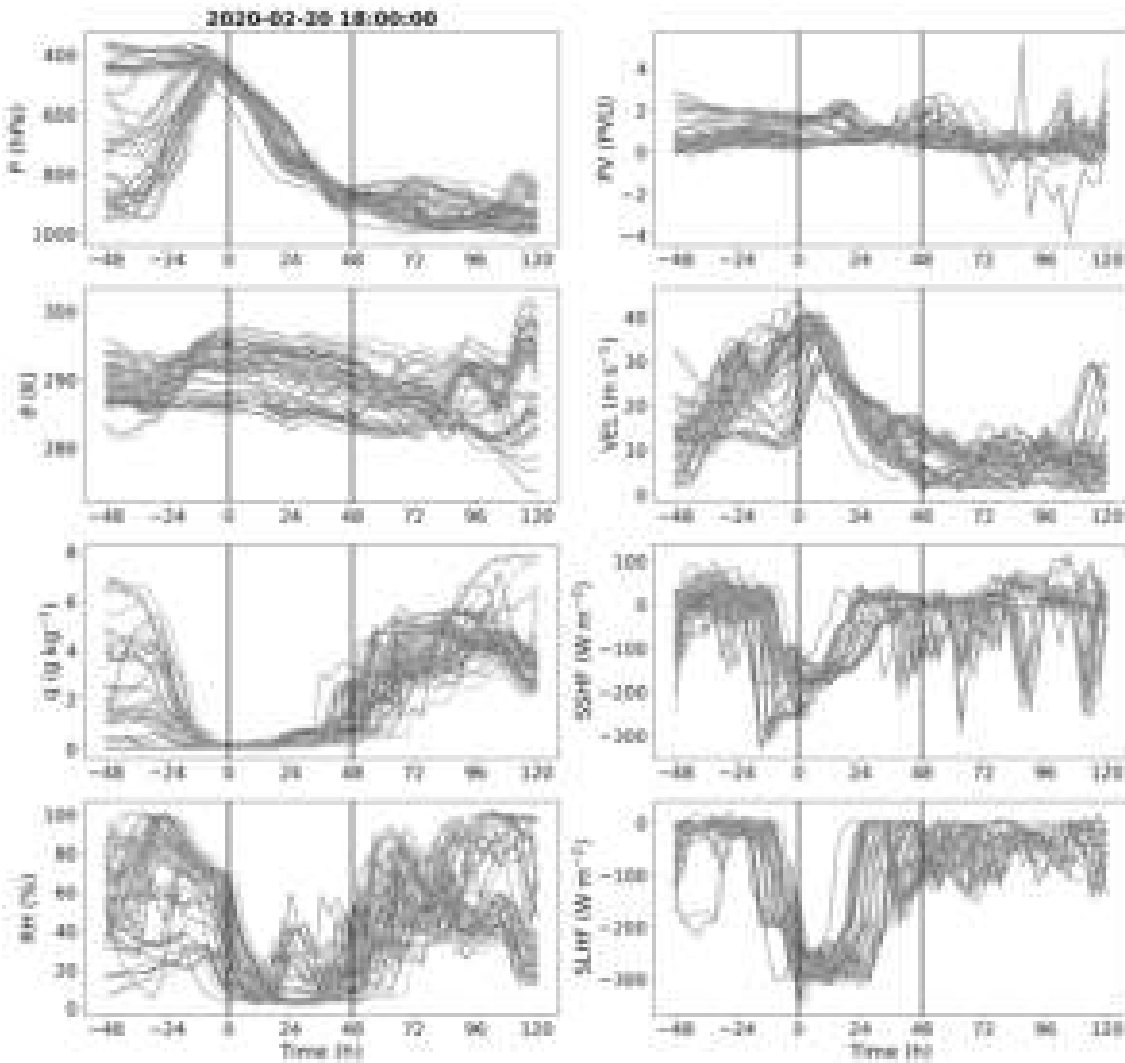


Figure 4.2: Variables traced along the DI trajectories as a function of relative time in hours with each line representing a trajectory. Variables include the pressure P (hPa), potential temperature θ (K), specific humidity q (g kg^{-1}), relative humidity RH (%), potential vorticity PV (PVU), velocity VEL (m s^{-1}), surface sensible heat flux SSHF (W m^{-2}) and surface latent heat flux SLHF (W m^{-2}). Time 0 h marks the start of the descending period and time 48 h the end, both timestamps are marked with a vertical line in each plot. All shown trajectories reach Brest during the descending period with a pressure value of at least 700 hPa first on 20 February 2020, at 18 UTC.

The pressure values at time -48 h exhibit a large spread that was already described in the trajectory pathway plot (Figure 4.1). The trajectories with the higher pressure values are located around the eastern U. S., while the trajectories at lower pressure levels originate from central Canada. In the

period -48 to 0 h, the trajectories near the surface rise considerably to roughly the same level of the other trajectories of about 500 hPa at time 0 h. The bulk of trajectories descends most strongly in the first 24 hours of the descending period with roughly 300 hPa, whereas in the second half of that period a slower sinking is observed of about 100 hPa. At the end of the descending period, most trajectories are located at or slightly above the 900 hPa level, indicating that they penetrated into the PBL but did not reach the surface around the radiosonde station Brest. Due to this pressure increase a substantial adiabatic warming is expected. In the remaining 3 days the trajectories stay between the 800 and 1000 hPa level. Upon closer examination a small group can be identified nearing 1000 hPa between time 72 and 96 h, rising up towards 800 hPa again between 96 and 120 h. This group probably represents the small cluster of trajectories that turned northeastward over France. The majority of the other trajectories continues to descend and reaches a final pressure value between 900 and 1000 hPa at time 120 h.

During the first two days before the descending period, the trajectories that start near the surface at lower potential temperature values experience a strong increase in potential temperature, probably caused by diabatic warming due to the release of latent heat during the ascent. The other group of trajectories show a continuous decline in potential temperature, which could indicate radiative cooling. At time 0 h, the potential temperature of the group that was near the surface generally surpasses that of the other group. Starting at 0 h, most trajectories experience a steady decrease in potential temperature of about $1\text{--}2$ K day $^{-1}$, which could be caused by clear-sky radiative cooling, since typical radiative cooling rates are of the same order (Savijärvi, 2006). Another reason for the observed diabatic cooling might be the evaporation of water into the dry airmass, as the DIs begin mixing with moister ambient air. After 48 h, irregularities emerge that get larger with time, leading to the largest spread at the end of the time series.

Similar to the pressure, a large spread is also observed in the specific humidity at the start with some trajectories exhibiting values of 0 g kg $^{-1}$ and the highest values up to about 7 g kg $^{-1}$. However, in the period -48 to 0 h, the specific humidity of all trajectories decreases to almost 0 g kg $^{-1}$, due to the high altitude of about 500 hPa. Around 24 h in the descending period, specific humidity starts to increase again along a few trajectories, although they remain at low values between 0 and 1 g kg $^{-1}$. After 36 h, most trajectories display increases with some up to 3 g kg $^{-1}$, but a few trajectories acquire almost no additional humidity at the end of the descending period at 48 h. This illustrates a high variability of mixing with the ambient, more humid air, since the trajectories are still bundled near Brest at this point in time and should experience a relatively similar environment. Beginning at time 48 h, all trajectories experience a strong moistening up to 96 h with most values slightly above 4 g kg $^{-1}$. Variability increases drastically at this point due to differences in the intensity of mixing. Subsequently, the majority of the trajectories shows a small decrease in specific humidity that leads to values below 4 g kg $^{-1}$, while a few outliers continue to gain humidity and end up near 8 g kg $^{-1}$. The relative humidity RH follows generally the evolution of specific humidity, although it presents a broader distribution. This is especially evident during the descending period (0 – 48 h) and underlines the variability of mixing with ambient, moister air.

Potential vorticity features mostly values between 0 and 1 PVU, but also a few outliers of up to 3 PVU between -48 and 0 h. Such high values could indicate a stratospheric origin. For instance,

Raveh-Rubin (2017) used a PV based criterion to identify stratospheric DIs and found that they constitute only 1.2 % of all identified DIs globally between 1979 and 2014. The criterion is that the PV magnitude of a DI remains above 2 PVU during the two days before descending (i.e. between -48 and 0 h). However, the usage of this strict criterion from Raveh-Rubin (2017) would yield 0 stratospheric DIs in Figure 4.2, since no trajectory maintains PV values larger than 2 PVU during the period from -48 to 0 h. The majority of trajectories stays between values of 0 and 1 PVU throughout the whole time series. Slight decreases of PV could be caused by mixing into the low PV air in the lower troposphere. Strong negative values, as shown by a few outliers, may be explained by the respective DI trajectory interacting with orography.

While the velocity also shows a large spread at the start, nearly all trajectories display a pronounced increase up to about 30 m s^{-1} between 0–12 h. Thereafter, the trajectory velocity decreases substantially until the end of the descending period at time 48 h and remains below 15 m s^{-1} for most trajectories. This pattern supports the previous statements about the velocity based on covered distance in the trajectory map. The high wind speeds around 0 h can be explained by the influence of the jet stream, which flowed parallel to the trajectories at this time.

The sensible and latent heat flux at the surface both show a pronounced drop beginning shortly before 0 h and rising to previous levels around 24 hours. Interestingly, those enhanced surface fluxes occur already before the trajectories reach Brest and while they are still located at lower pressure levels in the atmosphere. However, the location over the ocean could contribute to enhanced heat surface fluxes, especially the surface latent heat flux, due to the abundance of moisture and higher winds in absence of land friction processes. The rest of both time series shows a relatively large spread between the different trajectories. In the last 3 days in the surface sensible heat flux, multiple shorter drops can be identified, but only in a few trajectories, once again demonstrating the large variability in the trajectories even within the same DI event.

Large changes in trajectory variables in a short amount of time illustrate the problem of the long 12 hour interval between radiosonde observations. This problem becomes even clearer when satellite imagery is considered. DIs are visible in satellite water vapour imagery as dry slots and a narrow dry slot is visible in a water vapour image for this DI event, on 20 February, at 15:30 UTC over Brest (Figure 4.3). The image displays the moisture in the upper atmosphere around 9000 m (Kachelmann GmbH, 2020). Dry values are colored in yellow to red and wet values in white to green. The dry slot stretches from southern UK over northwestern France towards a weak cut off low west of Gibraltar over the Atlantic with very dry values. This dry slot is also characterised by enhanced PV values, with the highest values around the cut off low with up to 8 PVU and considerably lower values between the cut-off low and Brest with mostly about 2 PVU (not shown). Brest is also located in a region with higher PV, since it is just at the southern tip of a trough. However, as this yellow dry slot is rather narrow, it is located over Brest only for a short amount of time from about 13:45 to 16:45 UTC. But since the 3-hourly DI data revealed that the DI event lasted from 15 UTC until 12 UTC on the next day in Brest, the dry intrusion air masses are probably located too low in the atmosphere to be detected by the satellite water vapor and are masked by a more humid air mass.

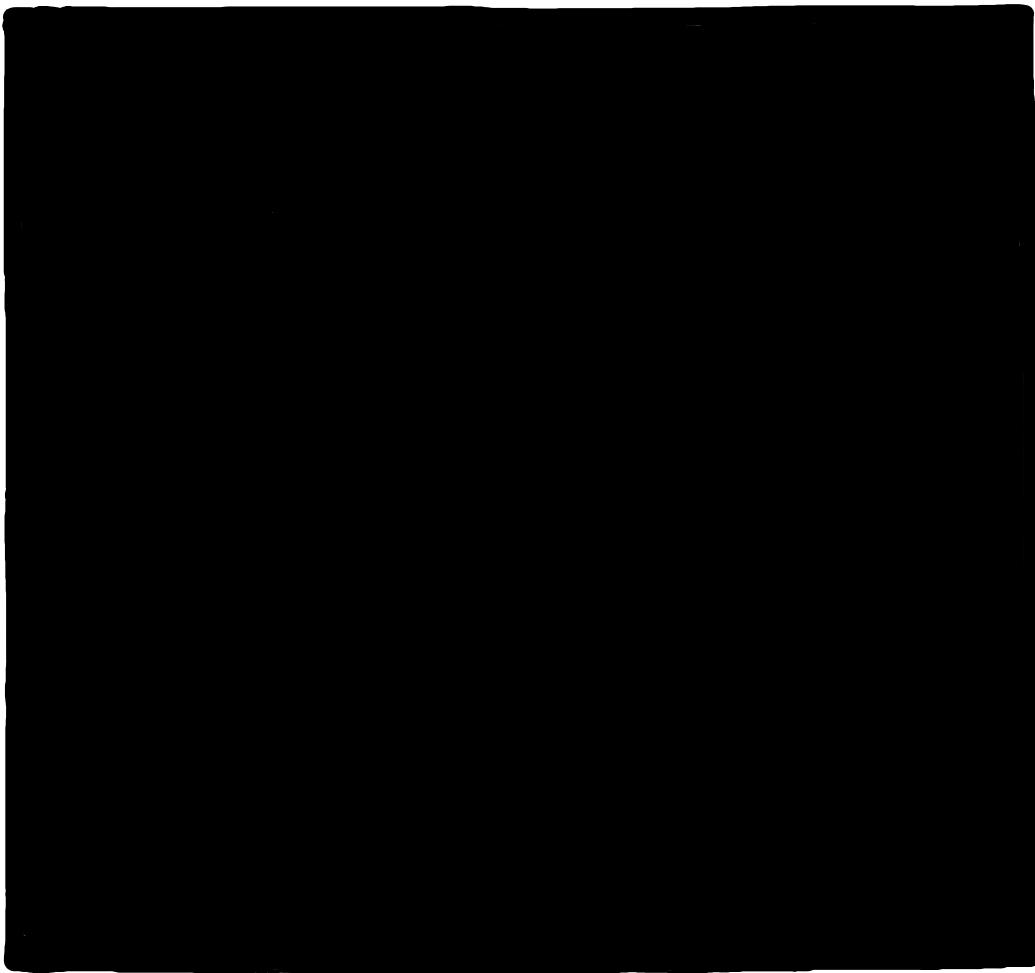


Figure 4.3: Satellite water vapor image over Europe on 20 February 2020, at 15:30 UTC (Kachelmann GmbH, 2020). This Figure is only available in the printed version.

Naturally, a radiosonde ascent at the time of the dry slot over Brest would be desirable, but because of the large interval of 12 hours between the radiosonde ascents, this is not possible. Due to this interval, only the radiosonde ascents on 21 February at 00 UTC and 12 UTC are classified as DIs, while the radiosonde ascent on 20 February 12 UTC is classified as a Pre-DI and the ascent on 22 February as a Post-DI. Additionally, one more radiosonde ascent before the Pre-DI is selected, classified as a Non-DI. The mentioned ascents are displayed in Figure 4.4, colored according to their classification and their time. The second DI profile is colored in a darker red than the first DI profile. For simplicity, when referring to the time of a radiosonde profile (e.g. 20 February 00 UTC), the year will be omitted in the following, since all radiosonde observations date back to February 2020.

The vertical profiles of temperature (Figure 4.4, a) mark the presence of an inversion layer in all cases, although the inversion for the Pre-DI on 20 February 12 UTC between 2.5 and 3 km appears more like a temporary fluctuation. As the temperature of the Pre-DI already decreased to about 270 K at this point, those fluctuations might be caused by snow that attached itself onto the radiosonde. The strongest inversion layer in terms of magnitude occurs during the Non-DI on 20 February 00 UTC around 1.5 km. Slightly above that is the inversion layer of the first DI on 21 February 00 UTC, which is the weakest inversion of all shown profiles. With increasing time,

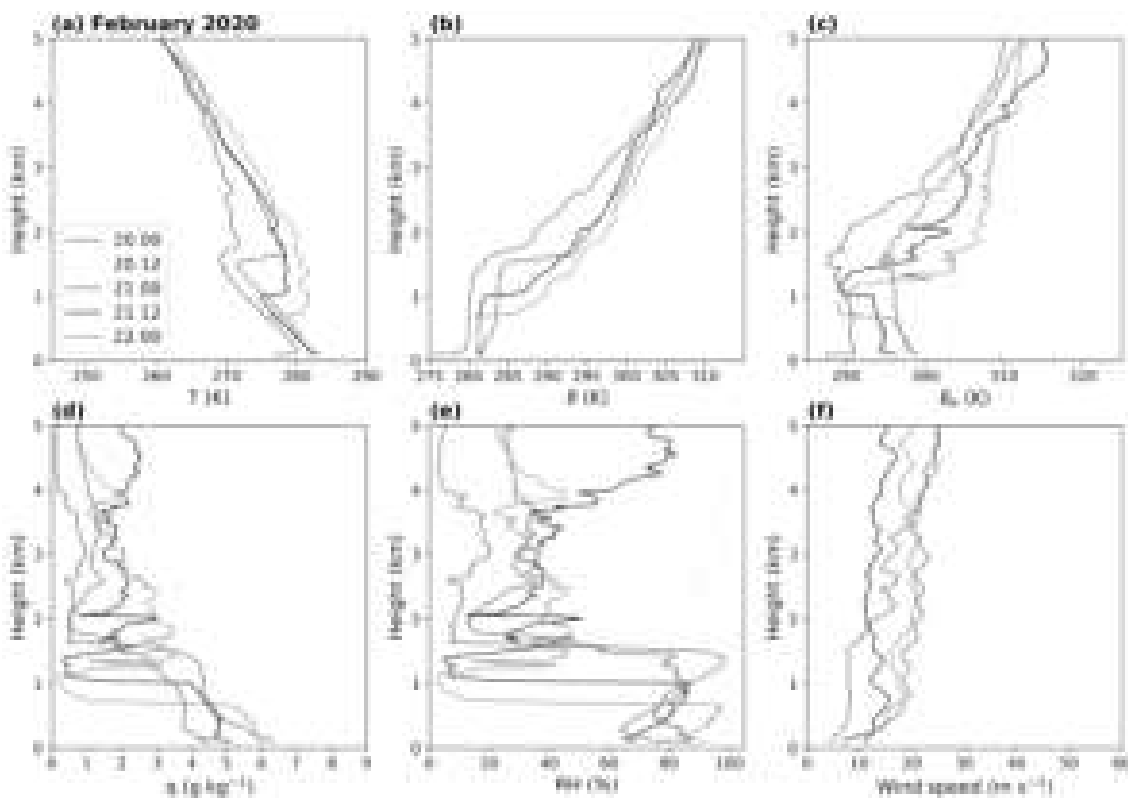


Figure 4.4: Vertical profiles of (a) temperature T (K), (b) potential temperature θ (K), (c) equivalent potential temperature θ_e (K), (d) specific humidity q (g kg^{-1}), (e) relative humidity RH (%) and (f) wind speed (m s^{-1}) based on radiosonde ascents in February 2020 from 20 00 UTC to 22 00 UTC. The numbers in the legend denote day and time of the profiles in the format DD HH.

this inversion descends downward and becomes stronger, leading to the inversion with the lowest altitude around 750 m and the sharpest temperature gradient which is observed on 22 February 00 UTC and classified as Post-DI. Such inversions could mark the top of the PBL (Lee, 2018). Large differences are especially visible between the two different DIs, with the later one on 21 February 12 UTC being consistently warmer in the lower 4 km and almost being as warm at the surface as the Pre-DI. In contrast, the earlier DI at 00 UTC features a strong surface inversion and is the coldest profile in the lower 2 km. This nocturnal inversion is expected according to the diurnal PBL evolution illustrated by Lee (2018). One reason for this could be an increased radiative cooling at the surface, due to the dryness of the lower troposphere and low wind speeds.

The inversion layers at higher altitudes in the PBL are a typical feature of DIs, as shown in Ilotoviz et al. (2021), and a reason why this event was chosen as case study, since other DI events sometimes do not feature those inversion layers at all (section 4.4.2). However, the DI-related inversion layers are still smaller than the inversion layer during the Non-DI at 20 February 00 UTC. These differences to Ilotoviz et al. (2021) may be explained by the fact that the shown profiles here are just one event, whereas Ilotoviz et al. (2021) show averages for the winter months in the years 2016–2018. The main reason could be geographical differences, since the station on the island Graciosa in Ilotoviz et al. (2021) is both influenced by subtropical and midlatitude synoptic systems, whereas Brest is probably not influenced by subtropical systems.

In the vertical profiles of potential temperature (Figure 4.4, b), almost constant values with height are observed in the lower troposphere in every radiosonde ascent, except for the Pre-DI, which increases almost monotonically, only interrupted by the fluctuations already mentioned in the temperature profiles. This moist adiabatic stratification in the Pre-DI profile is caused by rainfall during the corresponding radiosonde ascent on 20 February 2020 at 12 UTC (Figure 4.5, f). During the Non-DI, the potential temperature is relatively constant up to 1.5 km, although it is slightly increasing near the surface. After strongly increasing near the surface due to the inversion, the first DI ascent also shows constant θ up to 1.5 km, indicating a similarly deep but even better mixed layer than during the Non-DI. Since the sharp increase in θ begins where the inversion layer is located, the second DI and Post-DI exhibit considerably shallower well mixed layers with an altitude of about 1 km for the second DI and about 750 m for the Post-DI profile. As the first DI occurs at midnight with a strong surface inversion, the mentioned layer could also be the residual layer, because potential temperature in the residual layer often lacks a vertical gradient, leaving the impression that the air is well mixed (Lee, 2018). Thus, this could theoretically also indicate nearly absent turbulent mixing, if the features of the mixed layer at daytime are retained. But since the Pre-DI profile shows an increasing potential temperature during the day, the near constant vertical gradient during the first DI cannot be a remnant from the previous day and therefore indicates indeed a well mixed layer.

Due to the combination of temperature and humidity, θ_e (Figure 4.4, c) reveals the largest differences between the various radiosonde ascents so far. The largest values near the surface are observed during the Pre-DI, but since it stays relatively constant with altitude, it is the profile with the lowest values at 5 km. The other extreme is the first DI, which presents the lowest values near the surface. Both the first DI and the Non-DI feature a small decrease in θ_e with height, up to the inversion height of about 1.5 km, suggesting weak potential instability below the inversion layer. The second DI and Post-DI not only show the potential instability at lower altitudes, as expected due to the height of the inversion, but also a pronounced layer of low θ_e values, limited by sharp gradients. As this behaviour is not seen in temperature, it must be caused by the humidity profiles.

Indeed, the specific humidity profiles (Figure 4.4, d) reveal extremely dry layers in the DI-related profiles. While the first DI profile is driest near the surface, followed by the second DI and Post-DI profile, it also features a dry layer around 2 km. In the following radiosonde ascents, this dry layer descends and becomes even drier with a much sharper gradient, with q values close to zero around 1 km in the Post-DI. Although it seems that this dry layer would soon reach the surface, the following radiosonde ascent after 12 hours on 22 February 12 UTC (not shown) yields the same q values near the surface as the Pre-DI, which is by far the wettest category. Notably, the radiosonde ascent classified as Non-DI becomes extremely dry above the inversion layer at 1.5 km and remains the driest category above that height. However, this should not be confused with climatological values, as this is only one vertical profile on 20 February 00 UTC.

The mentioned dry layers are also discernible in the vertical profiles of relative humidity (Figure 4.4, e), albeit with a larger variability. The extremely sharp gradients occur at about the same height as the temperature inversion and the sudden increases of θ , demonstrating that RH is also suitable for identifying the PBL height. One exception is the Pre-DI RH profile, which stays constant at

about 100% RH up to 2.5 km, where the temperature fluctuations occur. Even above that level the Pre-DI has the highest RH values, since the temperatures are also the lowest above 3 km.

In terms of wind speed (Figure 4.4, f), the first DI is the profile with the lowest values near the surface which could help to explain the formation of the surface inversion, due to a lack of turbulent heat transport that favors radiative cooling (Kurz, 1990). On the other hand, the Pre-DI radiosonde ascent features the highest wind speeds throughout the whole 5 km, increasing with height. A possible reason for this might be the association of the Pre-DI with a cold front, since they are coupled with enhanced wind speeds and Ilotoviz et al. (2021) found all DIs preceded by detectable fronts. The wind speed values for the Post-DI and Non-DI profiles are relatively similar. Compared with those profiles, the second DI shows higher wind speeds in a shallow layer near the surface, but lower values above 500 m, due to a near constant wind speed with altitude.

To observe the evolution of the atmosphere near the surface, 1-hourly synop observations at Brest are utilized, ranging from 00 UTC on 20 February 2020 to 00 UTC on 22 February 2020 (Figure 4.5). The sea level pressure (Figure 4.5, a) decreases slightly at the beginning of the time series, only to start a large increase at about 20 February 12 UTC until 21 February 00 UTC to approximately 1030 hPa. This increase in pressure is expected, since the Azores high pressure system, visible in Figure 4.1, expanded towards Brest. After 21 12 UTC, the pressure slowly decreases. Throughout the whole DI event, the sea level pressure remains at relatively high values.

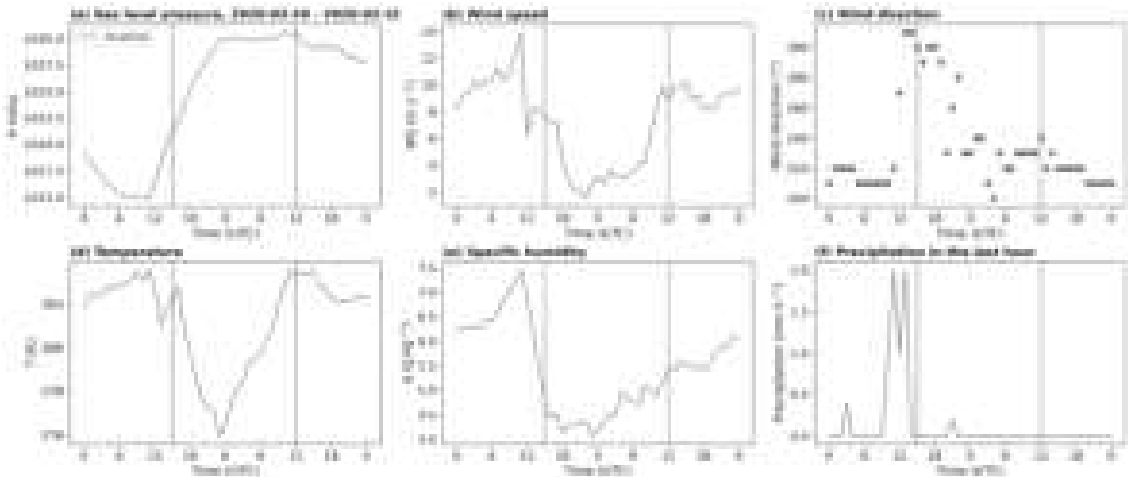


Figure 4.5: Synop observations at Brest from 00 UTC on 20 February to 00 UTC on 22 February 2020. Displayed variables include (a) sea level pressure (hPa), (b) wind speed (m s^{-1}), (c) wind direction ($^{\circ}$), (d) temperature (K), (e) specific humidity (g kg^{-1}) and (f) hourly precipitation (mm h^{-1}). The onset and end of the DI event are marked by red vertical lines.

A strong peak in wind speed (Figure 4.5, b) with a value of about 14 m s^{-1} on 20 February at 10 UTC is detected, followed by a decline in wind speed that continues until 22 UTC on the same day. After 21 February 06 UTC the wind speed increases again to about 9 m s^{-1} at 12 UTC and for the rest of the time series. This observed wind behaviour matches roughly the surface values of the corresponding radiosonde observations, with the highest wind speed before the DI and the lowest during the first DI radiosonde ascent. But the detailed synop observations reveal larger wind speed differences, especially during midnights. The minimum below 2 m s^{-1} on 22 UTC supports the hypothesis that the wind speed values play a key role in the formation of the observed surface

inversion in the radiosonde ascent on 21 February 00 UTC. Since the wind speed on 20 February 00 UTC and 22 February 00 UTC was much larger, no surface inversion formed at those times.

The wind direction time series (Figure 4.5, c) reveals a large wind shift shortly before the onset of the DI event. The wind direction changes from a southwesterly flow (220°) during the start of the time series to a northwesterly flow (300°) at about 20 February 12 UTC, which is indicative of a cold front passage (Kurz, 1990). After the next 12 hours, the wind direction returned to southwesterly flow (about 220°) for the remaining period. The timing of the wind direction shift is critical for the radiosonde ascents. At the Pre-DI ascent on 20 February at 12 UTC, the wind direction is due west, whereas for the radiosonde ascents of the first and second DI on 21 February 00 UTC and 21 February 12 UTC respectively, the wind direction returned to southwesterly flow already. This illustrates the limitations of the analysis based on radiosonde profiles, as the northwesterly wind direction would be missing due to the large 12 hour interval between radiosonde ascents.

The cold front passage hypothesis is further supported by the temperature behaviour (Figure 4.5, d), as it features a pronounced decrease after 20 February 16 UTC, coinciding with the drop in wind speed, shift in wind direction and the formation of the nightly inversion. On 20 February at 23 UTC, the minimum is reached with 276 K, followed by an increase in temperature up to 21 February 12 UTC to approximately 283 K. As expected due to the nightly inversion, the time series of wind speed and temperature show a similar progression.

Like the wind speed time series, the specific humidity (Figure 4.5, e) also features a strong peak at approximately 7.5 g kg^{-1} between 20 February 06 and 12 UTC, which coincides with the beginning of a precipitation period (Figure 4.5, f), though the rain intensity is rather weak with a maximum of 2 mm h^{-1} . Thus, the cold front probably reaches Brest within this time period. This is confirmed by mean sea level pressure analysis charts with fronts, air pressure and weather observations by the German Weather Service (Deutscher Wetterdienst, 2020). The chart on 20 February 2020 at 12 UTC reveals a surface cold front that just passed Brest and travels southeastward (not shown). After the peak in specific humidity, a sharp decrease follows to values of $4\text{--}4.5 \text{ g kg}^{-1}$ at the first DI occurrence at the station, marked by the first red vertical line. From that time, precipitation ceased for the rest of the time series, with one exception being a very weak intensity rain of 0.2 mm h^{-1} on 20 February at 21 UTC. The specific humidity slowly recovers during the next day, so that at the last time of a DI over Brest, marked by the second red vertical line, it rose back to about 5.5 g kg^{-1} and continued to rise.

An additional instrument for analyzing the PBL is the ceilometer. At Brest, a Vaisala CL31 Ceilometer is employed by Meteo-France, which measures the attenuated backscatter. Based on the observed backscatter profile during the event (Figure 4.6), the PBL height can be identified as a shift from a relatively strong backscatter to a lower backscatter above it. A conspicuous feature in the attenuated backscatter profile are the whitespaces that become dominant over 2 km. These are caused by data filtering according to the quality flag, meaning that a bad quality was assigned to the values in the whitespaces. Like the radiosonde profiles in Figure 4.4, the backscatter values also show a white gap above 0 m, since the station Brest is located at about 90 m above sea level and the observations start therefore at 90 m.

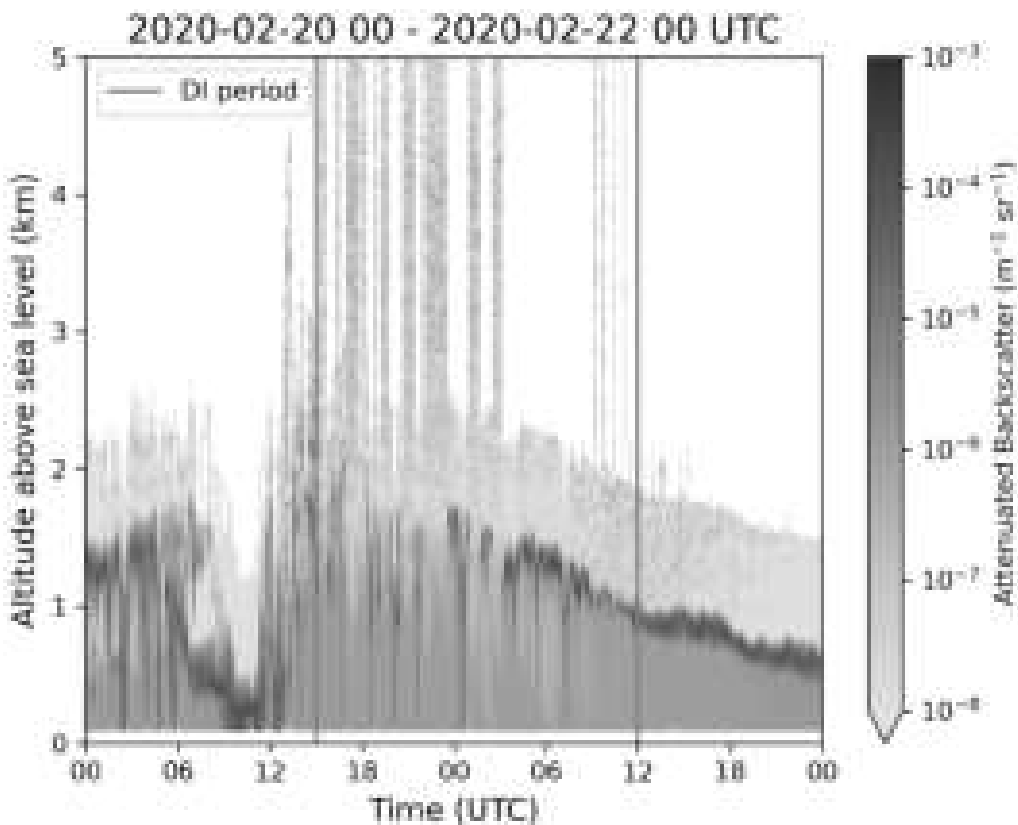


Figure 4.6: Attenuated backscatter profile ($\text{m}^{-1} \text{sr}^{-1}$) plotted with a logarithmic scale based on ceilometer measurements at Brest from 20 February 00 UTC to 22 February 2020 00 UTC. The red vertical lines mark the start and end of the DI event.

At the beginning of the time series, the PBL height is relatively easy to identify at about 1.5 km, as dark blue values indicating large backscatter are swiftly replaced by a very light blue color above, representing low backscatter values. During the arrival of the cold front, the PBL height collapses to only a few 100 m above ground, probably caused by precipitation. After 20 February 12 UTC, the PBL height quickly recovers, reaching its highest in the whole time series at the onset of the DI event on 20 February at 15 UTC. However, the signature for the PBL height is quite diffuse and weak at that time with large variations ranging from 1.2 to 2 km, signifying a substantial uncertainty. The PBL height signal regains clarity at 21 February 00 UTC at an altitude of about 1.6–1.7 km. After this point the PBL height starts a slow decline that continues until the end of the time series to an eventual altitude of 800 m.

The evolution of the PBL based on ceilometer data agrees reasonably well to the vertical profiles based on radiosonde data, where the PBL height can be determined by sharp gradients in potential temperature, specific humidity and relative humidity. It showcases a large variability in the PBL height during DI events with a large, albeit somewhat uncertain, PBL height at the start of the DI event and a considerably lower height at the end of the event. The clear signal that is visible in the ceilometer measurements during the DI event overall implies that such measurements could also be useful as part of the ground-based measurements during the NAWDIC campaign. Once again, the limits of radiosonde ascents with a large 12-hour interval between them are illustrated, as large variations occur already at smaller timescales.

This DI case study revealed large differences in the DI trajectories within the same DI event and a strong PBL response, mostly consistent with the expected DI impact on the PBL based on literature (Raveh-Rubin (2017), Ilotoviz et al. (2021)). Differences include a pronounced temperature inversion at the surface that was found under DIs as well as weaker temperature inversions at the top of the PBL during DIs. However, these are just the impacts of one DI event and they may not be representative for the average DI behaviour at Brest, let alone western Europe. Therefore, the next section will first focus on the climatological DI frequency in western Europe and Brest, before the section afterwards analyzes the average vertical profiles of DI events in Brest.

4.2 Climatological DI frequency in western Europe

The DI outflow frequency over western Europe exhibits a pronounced seasonal cycle and is generally highest in the winter months, as Figure 4.7 illustrates. This Figure displays the climatological mean occurrence frequency of the 3-hourly DI timesteps over the winter months December, January and February (DJF) (Figure 4.7, f) and the DI frequency anomaly with respect to (f) for the individual months from November (Figure 4.7, a) to March (Figure 4.7, e) over the period from 3 January 1979 to 31 December 2022. The radiosonde stations from Meteo-France are marked with a blue point and the stations from ECMWF with a white point. Further, each station is labelled with its respective station name.

The DI frequency in winter (Figure 4.7, f) shows a broad zone of enhanced DI activity stretching from the North Atlantic south of Ireland over southern France into the Mediterranean, with frequency values of 4 % at Brest and up to 5 % over southern France. This means that 5 % of all 3-hourly timesteps from 3 January 1979 to 31 December in the winter months DJF feature a DI that descended to altitudes lower than 700 hPa in that region. Further, the DI frequency in DJF exhibits a pronounced maximum east of Nimes-Courbessac and a second maximum in the vicinity of the station Cuneo-Levaldigi, both with a DI frequency greater than 6 %. These maxima could be caused by the Alpine mountain range due to Foehn effects. Such local effects due to topography are investigated in detail in section 4.5. Low values of DI outflow frequency are observed over mainland Spain, whereas the coastlines feature higher values, particularly over the eastern coastline to the Atlantic, including Portugal, and the western coast around the station Barcelona-Servei. A clear reduction of DI outflow frequency is visible towards northern Africa and Germany, as DI frequencies are less than 2.5 %.

This pattern can in general be seen in each month depicted in Figure 4.7, but with varying DI outflow frequency. To provide a better visualisation of the differences, the DI frequency in the individual months (Figure 4.7, a–e) is shown as anomaly with respect to the winter climatology (Figure 4.7, f). In November (Figure 4.7, a), the DI outflow frequency is substantially lower compared to the DJF average with only below average values over the whole considered region, with the highest negative anomalies over southern France, northwestern Italy and the Mediterranean.

December (Figure 4.7, b) features small positive anomalies over southern France and the North Sea, while the other regions display below average values.

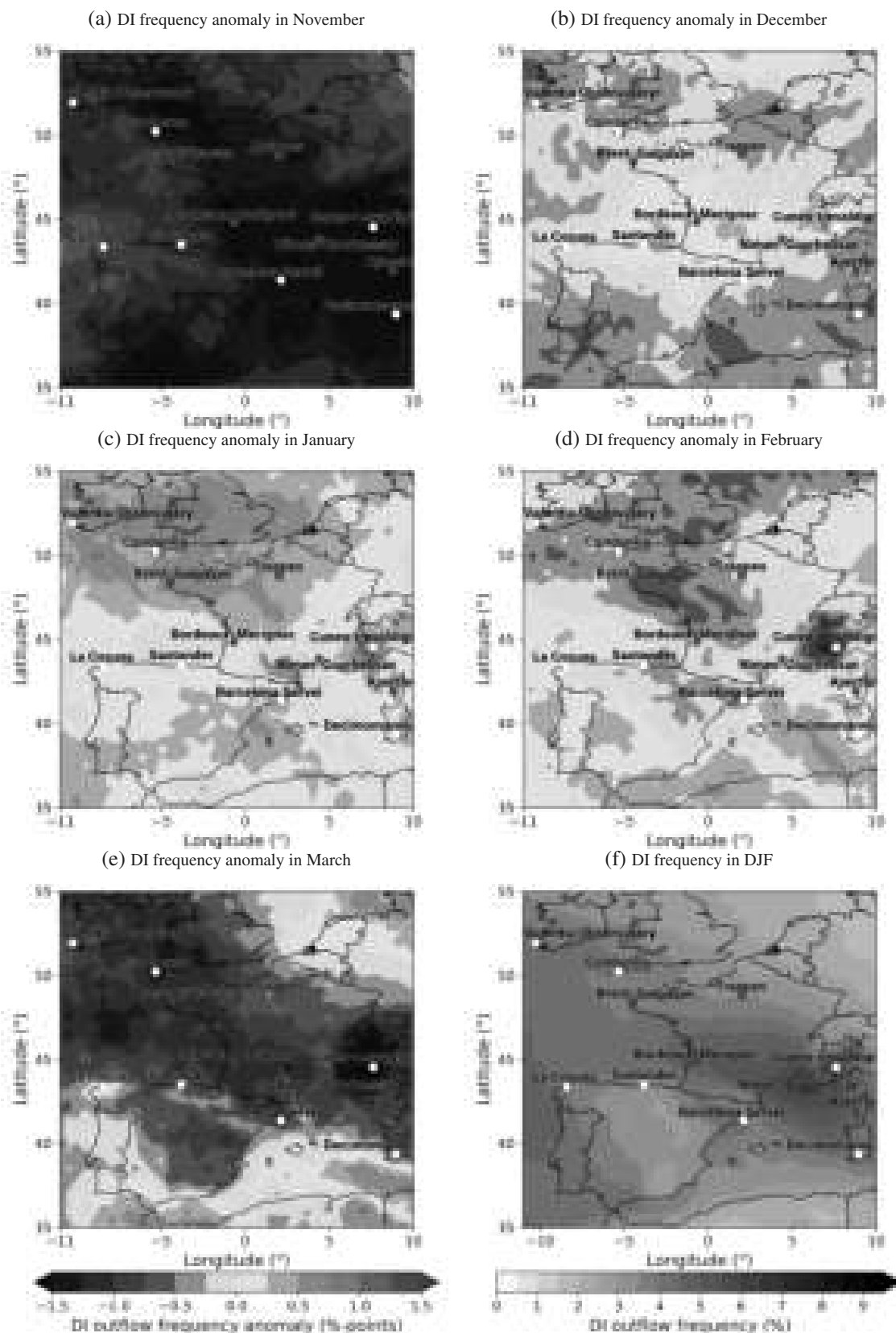


Figure 4.7: DI outflow frequency anomalies in (a) November, (b) December, (c) January, (d) February and (e) March (shading in % - points) with respect to the average over DJF (f) (shading in %) from 3 January 1979 to 31 December 2022.

January (Figure 4.7, c) is the month with the highest DI activity, exhibiting the largest positive anomalies over northern France, the UK and Ireland with some spots reaching anomalies of almost 1 %-point more than during the average winter (Figure 4.7, f). Smaller positive anomalies are observed over Spain and the region around Cuneo-Levaldigi. The largest negative anomaly in the displayed map lies west of Nimes-Courbessac and is with -0.5 to -0.025 %-points still relatively small.

February (Figure 4.7, d) shows almost the opposite anomaly pattern compared to January, with northern France, UK, Ireland and Cuneo-Levaldigi now experiencing negative anomalies. In the southern map section, south of roughly 47 °N, positive anomalies dominate, though in different locations than in January.

The last depicted month is March (Figure 4.7, e), which features mostly negative anomalies that are larger than during the winter months. Exceptions include the regions south of Spain, south of Sardinia and north of Germany, where even positive deviations are observed, indicating a higher DI activity in these locations than in the winter months DJF.

This analysis confirms the findings in the literature, that DI activity in the midlatitudes and specifically western Europe is generally highest during the winter months (Raveh-Rubin, 2017; Stohl, 2001). A sharp decrease in DI frequency is already visible by comparing the months November and March with the winter average, though there are small areas with positive anomalies in March. A similar analysis of the summer months (not shown here) yielded almost no DI frequencies. The seasonality of DIs is linked to the seasonality of extratropical cyclones (Wernli and Schwierz, 2006), albeit with variable locations and frequencies. The relationship between extratropical cyclone and DI climatology might be interesting for future research. Due to the pronounced seasonality of DIs, it is justified to focus the following analyses only on the winter months, when most DIs are expected on average.

Since the presented frequency maps only depict the average over the period from 1979 to 2022, they contain no information of the interannual variability of DI frequency. This information is pictured in Figure 4.8, showing the number of identified 3-hourly DI outflow time steps at Brest for each winter month per year. Since the data begins on 3 January 1979 and ends in December 2022, the winter months are organised by year and not coherent winter seasons. This means for the winter months of one year that, counterintuitively, January is placed left of a year number, February is centered at the year and December is right of the year number. Due to the missing first two days in January 1979, the DI frequency in this month may be an underestimation, if a DI event occurred in those missing 2 days before the data starts.

All months demonstrate a large variability without any specific patterns or immediately visible trends. In terms of extremes, January is the most prominent month, featuring both a month in 1997 with no DI occurrence at all and the month with the highest amount of DIs in 2015 with more than 70 3-h DI time steps. This implies that about 28 % of the time in January 2015 a DI at altitudes below 700 hPa was present within a 1 ° radius of Brest. February also exhibits a large variability with no single DI observed in 1986, 1987 and 2006, whereas the peaks in February 1997, 2020 and 2022 with a frequency of more than 50 are only surpassed by the aforementioned January 2015. Even though DIs are detected in all Decembers in the analyzed time period, a considerable spread

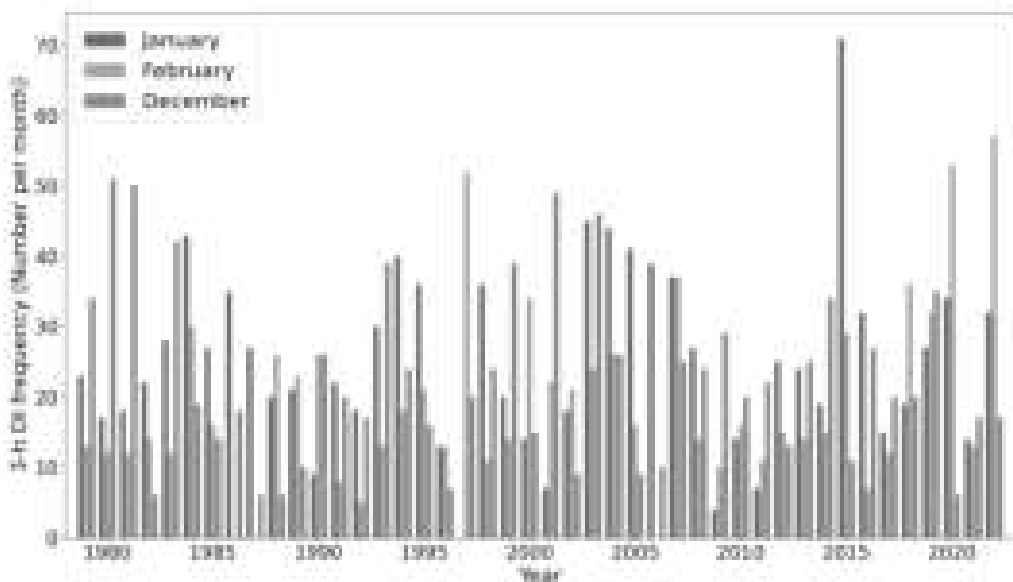


Figure 4.8: Frequency of 3-hourly DI time steps (Number per month) at Brest over the winter months DJF.
The winter months are centered around the year tick, so that the month left of the year corresponds to January and the month right of the year to December.

is still apparent with a high frequency of about 50 in 1980, 1981 and 2001 and a substantially lower frequency below 10 DI time steps per month in 1982, 1987, 1988, 1996 and 2020.

These monthly differences add up to interannual or seasonal variability. This can result in extremes such as the low DI activity in year 1996, where every month had a frequency below 15 or in high DI activity in 2019, with each month averaging a frequency of about 30. However, this demonstrates that these interannual extremes are already more moderate than the monthly extremes. Intraseasonal variability also presents big differences. While some winter seasons like 2014/15 and 2019/20 have consistently high DI frequencies, the winter 1996/1997 featured a January with no DIs at all, only to be followed by the third most active February in terms of DI number per month.

This investigation reveals large differences in the temporal distribution of DI events. Although the distribution of DI frequencies seems arbitrary, further research is required to understand how it is linked to slower varying atmospheric conditions and teleconnections. Instead of examining every DI event identified here, the next section will focus on investigating the average lower tropospheric structure during DI events at Brest.

4.3 Lower tropospheric structure during DIs at Brest

To explore the effects of DIs on the PBL and its diurnal variations, e.g. nightly inversions near the surface during DIs as seen in the case study at the beginning of this chapter, the analysis of the lower tropospheric structure is split into the profiles at 00 and 12 UTC. The different classes are calculated based on 12-hourly data and the determined numbers of the different classes are shown in Table 4.1. This Table is divided in categories identified at 00 UTC (upper part) and at 12 UTC (lower part), as well as the number of categories per year. Additionally, the total number of missing radiosonde files is specified in the last column, and the identified categories for those missing files

are stated in parenthesis behind the number of available files. The first row of each subtable states the sum of each category over the whole time period.

Table 4.1: Number of identified categories at 00 UTC (upper part) and 12 UTC (lower part) for Brest in the period 1 December 2016 to 31 December 2022. The number of categories of missing data files is given in parentheses behind the number of available files.

Time (00 UTC)	Pre-DI	DI	Post-DI	Non-DI	Pre-and Post-DI	Missing
2016–2022	34 (1)	65 (4)	32 (1)	431 (9)	5	15
2016	1	4	1	25	0	0
2017	4	5	3	77 (2)	1	2
2018	6 (1)	9 (2)	3	67 (3)	1	6
2019	11	12 (1)	7	60	1	1
2020	6	12	9	66	2	0
2021	3	7	4	76	0	0
2022	3	16 (1)	5 (1)	60 (4)	0	6
Time (12 UTC)	Pre-DI	DI	Post-DI	Non-DI	Pre-and Post-DI	Missing
2016–2022	46 (2)	55 (2)	44 (1)	422 (4)	4	9
2016	2	3	1 (1)	24	0	1
2017	4	5	4	77 (1)	1	1
2018	5	8 (2)	7	67 (1)	0	3
2019	8	13	10	60	1	0
2020	10	11	7	63	0	0
2021	7	4	6	73	0	0
2022	10 (2)	11	9	58 (2)	2	4

For the year 2016 only December is available, resulting in lower numbers than in other years, since other years include data for all winter months (DJF). It is important to note that Pre- and Post-DI classes at 00 UTC are associated with DIs at 12 UTC and vice versa. This is nicely illustrated by the number of categories for the whole time period, as the 00 UTC DI number is 10 profiles higher than the DIs at 12 UTC, whereas the opposite is true for Pre- and Post-DIs.

Naturally, the total number of DIs is much lower than in Figure 4.8, since that Figure was based on 3-hourly data. The 12-hour frequency used here leads to a massive reduction. For example, if a DI event occurred at Brest from 03 UTC to 21 UTC, it would last 7 3-h time steps but only 1 12-hourly time step at 12 UTC would be identified. Still, the interannual variability detected at 3-h based values is present here, with the years 2017 and 2021 featuring a lower DI numbers than the other analyzed years.

Based on the definition of the Pre- and Post-DI classes, the same amount of time steps would be expected for both classes when the 00 and 12 UTC values are all added. However, this is not entirely the case, as the total numbers are 80 (3) for Pre-DIs and 76 (2) for Post-DIs. This means that in total 83 Pre-DIs and 78 Post-DIs are identified in the whole time period, when missing data files are included in the categories. One reason for this mismatch is the occurrence of a DI event

right at the end of the winter season, i.e. on 28 February at 12 UTC, where the Post-DI would be on 1 March 2019 00 UTC, but is excluded since only data in the winter months is analyzed. This occurred both in 2017 and 2019. Another reason is the non-existence of DI files, since both the Pre-DI and Post-DI categories are only identified, if the file classified as DI 12-hours after or before is available.

A little more than 11 % of available Pre- or Post-DIs occur at time steps that are classified as both Pre- and Post-DI, which means a DI occurred 12 hours before and after these time steps. This could contribute to a blurred signal of typical characteristics during Pre- or Post-DIs, since the lower tropospheric structure could not recover to normal conditions before or after those categories.

The vertical profiles at 00 UTC in Brest-Guipavas of temperature T, potential temperature θ , equivalent potential temperature θ_e , specific humidity q, relative humidity RH and wind speed between 0 and 5 km height are displayed in Figure 4.9. It shows the median lines of the identified DI, Pre-DI, Post-DI and Non-DI classes plus the range between the 25th and 75th percentiles of DIs and Non-DIs, all interpolated to regularly spaced vertical levels of 10 m.

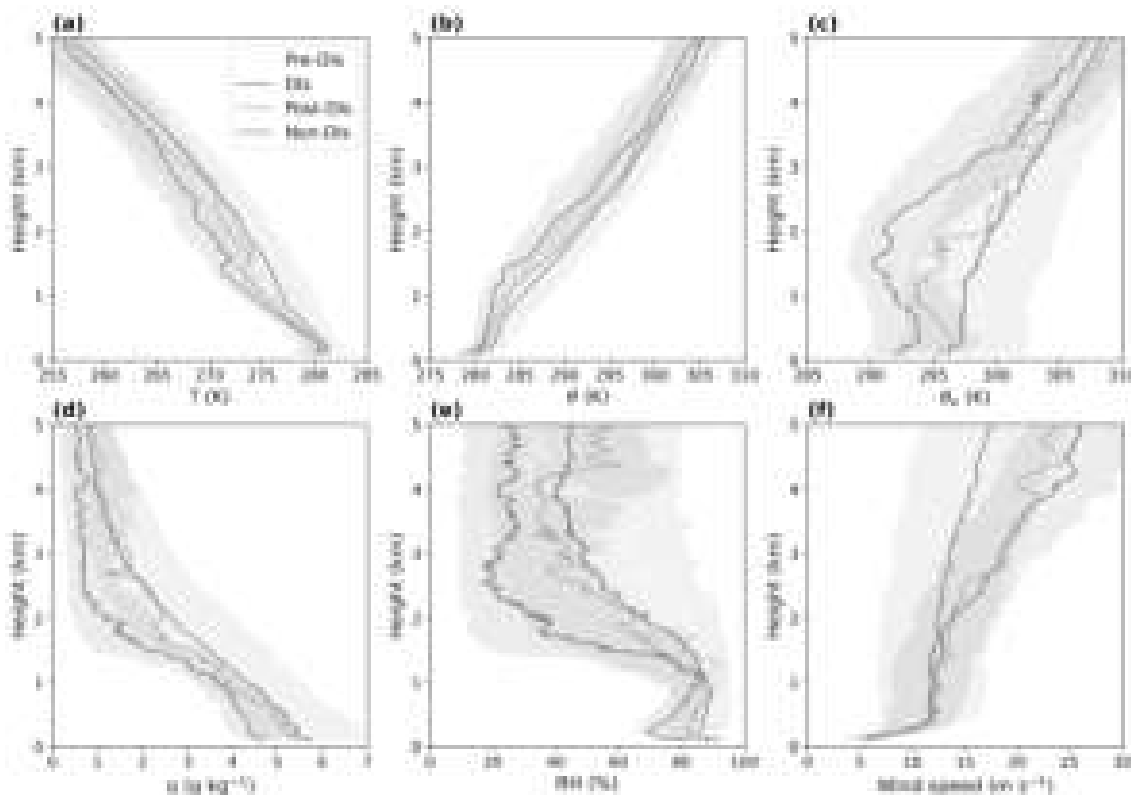


Figure 4.9: Average vertical profiles for Brest-Guipavas at 00 UTC of (a) air temperature T (K), (b) potential temperature θ (K), (c) equivalent potential temperature θ_e (K), (d) specific humidity q (g kg^{-1}), (e) relative humidity RH (%) and (f) wind speed (m s^{-1}). Solid lines are the median value at each height and category and the shaded area marks the interquartile range of DIs and Non-DIs.

In subplot a), a temperature inversion at the surface is observed that is strongest during DIs and nonexistent during Pre-DIs. The temperature of DIs is the coldest, closely followed by Post-DIs and then Non-DIs, while the temperature of Pre-DIs is the warmest at the surface. Depending on the respective timing for each DI event, Brest might be located in the warm sector of a cyclone and the cold front passage could occur between the Pre-DI and DI radiosonde ascents, leading to

warmer temperatures during Pre-DIs. On the other hand, a (masked) cold front passage can also cause a temperature increase near the surface by eliminating the temperature inversion layer at the surface, leading to colder air only at higher altitudes (Kurz, 1990). Accordingly, the DI-related temperatures are much cooler between 1 and 3 km height than the Non-DI temperature. This means that despite the adiabatic warming of DIs during their descent, the advected air is still cooler than the in-situ air, similar to the observations in Ilotoviz et al. (2021). Furthermore, all DI-related classes show an inversion between 1 and 2 km, with the Pre-DI being the smallest and lowest at roughly 1.2 km, whereas the DI and Post-DI inversions appear almost identical in strength and height at approximately 1.5 km. However, the DI temperature is a few degrees cooler than the Post-DI temperature, indicating that atmospheric conditions are starting to recover in Post-DIs. Except for the surface, Non-DIs show no notable inversion, but only a short-lived patch of constant temperature around a height of 1 km. The lack of an inversion could be explained by the averaging process, since Non-DIs occur far more frequent than DI categories and inversions at different heights may not be visible anymore in the median.

The potential temperature θ (Figure 4.9, b) shows a steeper curve in the lowest 1 km for the DI-related classes than for the Non-DIs, with the smallest gradient during DIs, indicating an almost neutral stratification. Pre-DI potential temperature exhibits larger temperature values near the surface than the other categories. The cold anomaly of DIs in the first 3 km is clearly visible in the potential temperature. In all DI-related classes, a small but sudden increase in potential temperature is observed at an altitude of about 1.2 km, probably indicating the height of the PBL for Pre-DIs. But for DIs and Post-DIs such a spike is also visible at about 1.5 km, in line with the observed temperature inversion at that height. Remarkably, these sudden increases are also visible in the shaded interquartile range (IQR) of DIs. At 1.2 km height, only the high end of the IQR that marks the 75th percentile shows a sudden increase, while at about 1.5 km height both the 25th and 75th percentile show such an increase. This is not the case for the Non-DI IQR, as it increases more gradually with height, like the Non-DI median. Under Post-DIs the θ profile shows the second strongest increase after Non-DIs, possibly hinting at a residual layer instead of a mixed layer.

Large differences are visible in the equivalent potential temperature θ_e (Figure 4.9, c). DIs exhibit smaller values through the entire 5 km. The DI minimum in 1.5 km height is especially pronounced, located at much lower θ_e values than the other cases. Moreover, the IQR of DI and Non-DI are just barely touching each other at that height. This demonstrates that the values of θ_e during DIs are highly unusual compared to Non-DIs. As expected, θ_e displays the largest differences among the categories yet, since it combines temperature and humidity. During Post-DIs, the minimum occurs around 1 km, inconsistent with the observed temperature inversion at 1.5 km and the sudden rise in θ at 1.2 km. This suggests that those features may be retained of the previous mixed layer during DIs at the daylight hours and are in the process of transitioning back to normal values. However, those inconsistencies may also be caused by the averaging process.

Specific humidity q in Figure 4.9 (d) shows that DIs possess the driest values throughout the entire considered atmospheric column. Pre-, Post and Non-DI classes are much closer together, with Post-DIs being slightly drier and Pre-DIs slightly wetter than Non-DIs in the lower 3 km. The same behaviour is generally evident in the relative humidity RH (Figure 4.9, e), with an exception around

1 km. At this height, the differences between the classes become quite small and the Post-DI is shortly drier than the DI. Above this height, the categories spread out into the same pattern as in specific humidity, but with even larger differences. The fact that larger (specific) humidity values occur during Pre-DIs than under Non-DIs could be indicative of a cold front passage, as observed in the case study at the start of this chapter. Pre-DI characteristics like warmer temperatures and higher humidity near the surface may also be related to cyclone structure, since moist and warm air is typically transported poleward in front of a cyclone (Kurz, 1990).

Moreover, Pre-DI cases show by far the greatest wind speed (Figure 4.9, f) near the surface and in the lower 3 km, supporting the theory of a cold front passage. In the first 1 km from the surface, DI and Post-DI closely follow the Non-DI median. After that, their wind speed values begin increasing with height, approaching the Pre-DI values and (partially) exceeding even the 75th Non-DI percentile above 3 km. This increasing wind speed with height under DIs is also evident in the shaded IQR. In the lower 2 km, the DI IQR is almost completely contained inside the larger Non-DI IQR. The Non-DI IQR is probably larger since it is based on 431 radiosonde profiles, whereas the DIs are based on only 65 profiles. Above 2 km, the DI IQR increasingly shifts away from the Non-DI IQR. Although the wind speed also increases with height during Non-DIs, it grows at a much slower rate than during DIs.

The profiles of the median values at 00 UTC reveal a surface inversion in all categories except the Pre-DI, which is expected due to the typical diurnal variations of the PBL (Lee, 2018). During Pre-DIs, these variations are probably superimposed by a front passage, leading to higher wind speeds at the surface that favor mixing and prevent the formation of a temperature inversion. Therefore, Pre-DIs exhibit higher temperatures than during Non-DIs near the surface and lower temperatures than during Non-DIs above 500 m. This temperature behaviour corresponds to a masked cold front (Kurz, 1990). Based on the diurnal evolution of the PBL, no surface inversion is expected to occur at 12 UTC. In order to investigate this, among other differences, the median vertical profiles of Brest at 12 UTC are shown in Figure 4.10, with the same variables as in the previous Figure for 00 UTC.

In the temperature profiles (Figure 4.10, a), the Post-DI is the coldest case, whereas Pre-DI, DI and Non-DI are relatively similar in terms of temperature at the surface. In contrast to the previous temperature profiles, at 12 UTC there is no inversion near the surface in any category, as expected. Above the surface, Pre-DI and DI decrease faster than Non-DI and are jointly with the Post-DI colder than the Non-DI case, exhibiting the same cold anomaly in DI-related classes at 1–3 km height as in the profiles at 00 UTC. However, the DI median is slightly warmer throughout the considered atmospheric column, while Pre-DI and Post-DI are slightly colder, resulting in more similar values at 1–3 km compared to the profiles at 00 UTC, where DIs were clearly the coldest class. Between 1 and 3 km altitude, there are only a few small inversions in the DI-related situations, with the lowest one in Post-DIs at approximately 1.2 km and in Pre-DIs and DIs at approximately 1.6 km. Another very weak inversion is visible during Pre-DIs at a low altitude of 900 m.

Under DIs the potential temperature θ (Figure 4.10, b) is nearly constant in the lowest 1 km, but a slow increase begins already at 800 m, followed by a more abrupt increase at 1.5 km, roughly in

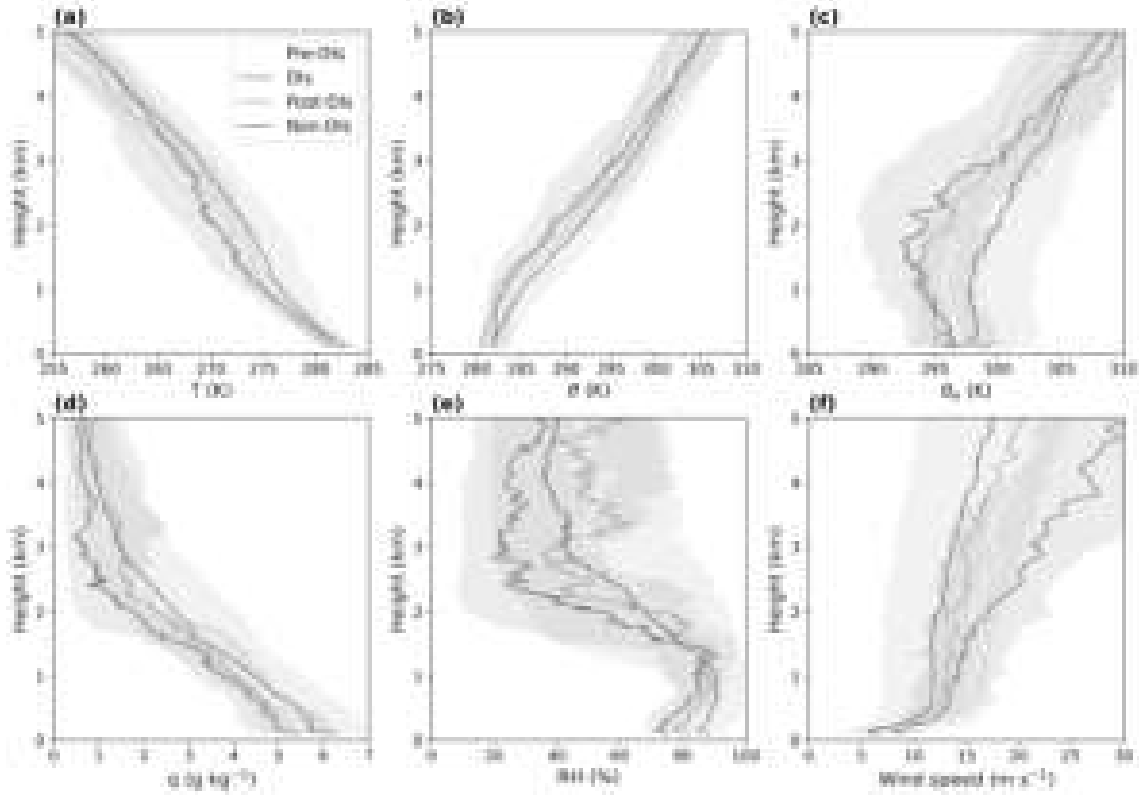


Figure 4.10: Average vertical profiles for Brest-Guipavas at 12 UTC of (a) air temperature (K), (b) potential temperature (K), (c) equivalent potential temperature (K), (d) specific humidity (g kg^{-1}), (e) relative humidity (%) and (f) wind speed (m s^{-1}). Solid lines are the median value at each height and category and the shaded area marks the interquartile range of DIs and Non-DIs.

line with the observed small temperature inversion. The DI IQR is steeper than during 00 UTC in the lowest 1 km, since no surface inversion occurred at 12 UTC, but it still shows a sudden increase at 1.5 km, almost perfectly in agreement to the DI median. Potential temperature profiles during Pre-DI and Post-DI are also steeper than during Non-DI situations, similar to the 00 UTC profiles. The Pre-DI median displays an increase in potential temperature already at about 900 m, coinciding with the barely visible temperature inversion. This occurs for Post-DIs at about 1.2 km, as expected by the temperature inversion. This suggests that the median PBL altitude in DI-related situations is highest during DIs and lowest during Pre-DIs, which is consistent with the earlier case study and the results from Ilotoviz et al. (2021), though they estimated larger values for the PBL altitude overall. Excluding the higher values at the surface due to the missing inversion, the 12 UTC θ profile under Non-DIs appears similar to the 00 UTC profile and shows only a gradual increase in θ , not allowing an estimation of the PBL height.

DIs still feature the most pronounced and lowest minimum in θ_e (Figure 4.10, c) at a height of about 1.5 – 1.8 km, although the difference to the other situations is smaller than before. This is obvious at the surface, where DIs possess larger values than Post-DIs and almost as large as Pre-DIs. Above the surface, the DI median quickly decreases, suggesting potential instability during DIs. However, the 75th DI percentile partially touches the Non-DI median during the minimum, indicating a large variability, since Non-DIs show the largest values during the first 4 km. Although all classes show

a rapid decrease immediately above the surface, DIs display a more sustained decrease until the minimum, leading to higher potential instability than in the other classes.

In the specific humidity (Figure 4.10, d) and relative humidity profiles (Figure 4.10, e), DIs are still the driest case but this dryness is almost matched by Post-DIs in the lower 1.5 km. In the same region, Pre-DIs are slightly drier than Non-DIs. Interestingly, the specific humidity values at the surface for all categories are much larger than directly above, which could be caused by humidity transport from the ocean, since Brest is located in a sheltered bay. While q values continue decreasing above the surface, the RH actually increases for all classes and starts rapidly decreasing above 1.5 km, with the strongest decrease during DIs.

Wind speed profiles (Figure 4.10, f) repeat the pattern of RH with slightly larger values near the surface than immediately above it and an increase above that small local minimum. Compared to RH profiles, the decrease from the surface is weaker, but the subsequent increase much stronger. Therefore, this pattern in humidity could be connected to the wind, if the main wind direction comes from the ocean.

The main difference to the 00 UTC wind speed profiles is that DIs feature generally higher wind speeds, while Pre- and Post-DI wind speeds are on average lower in the considered 5 km. This opposing pattern appears reasonable, since the Pre- and Post-DI categories at 12 UTC are typically identified based on DIs at 00 UTC and vice versa. However, the IQR of DIs reveal that the wind speed increase above 3 km is associated with a rising variability. The lower border of the IQR, marking the 25th percentile, stayed almost constant between 2.5 – 3.5 km, compared to the profiles at 00 UTC. On the other hand, the 75th percentile reaches 30 m s^{-1} already at about 3.2 km. Two DI events that demonstrate this large variability are investigated in section 4.4.

Another important aspect to analyze is the wind direction during the different classifications, since it might help to explain the large humidity values directly at the surface. Indeed, the wind directions at the surface reveal mostly south to southwest wind directions with the exception of DIs (not shown). These wind directions may transport humidity from the bay southwest of Brest-Guipavas to the station, possibly leading to the elevated humidity values at the surface. However, directly at the surface the wind flow may be distorted by local effects and may not be representative for the typical evolution of wind direction during DI events in the PBL. Therefore, a height of 500 m is selected for the analysis of different wind directions and speeds in the PBL of the different categories with the combined data at 00 and 12 UTC (Figure 4.11).

The Pre-DIs (Figure 4.11, a) exhibit a predominantly westerly wind direction, with only a few outliers showing easterly flow. The outliers are characterized by low wind speed, whereas the westerly wind direction displays very strong wind speeds above 24 m s^{-1} in a few instances. Overall, Pre-DIs are the class with the highest wind speeds at 500 m. A dominant western wind direction is also observed during DIs (Figure 4.11, b), though it is centered in the northwest quadrant, whereas the Pre-DI wind directions are almost distributed evenly in southwest and northwest wind directions. Additionally, a few more outliers with easterly flow are visible. Contrary to DIs, Post-DI wind directions (Figure 4.11, c) are centered in the southwest quadrant and slightly more spread out than the Pre-DI and DI cases. Lastly, the Non-DIs (Figure 4.11, d) show predominantly a southwesterly

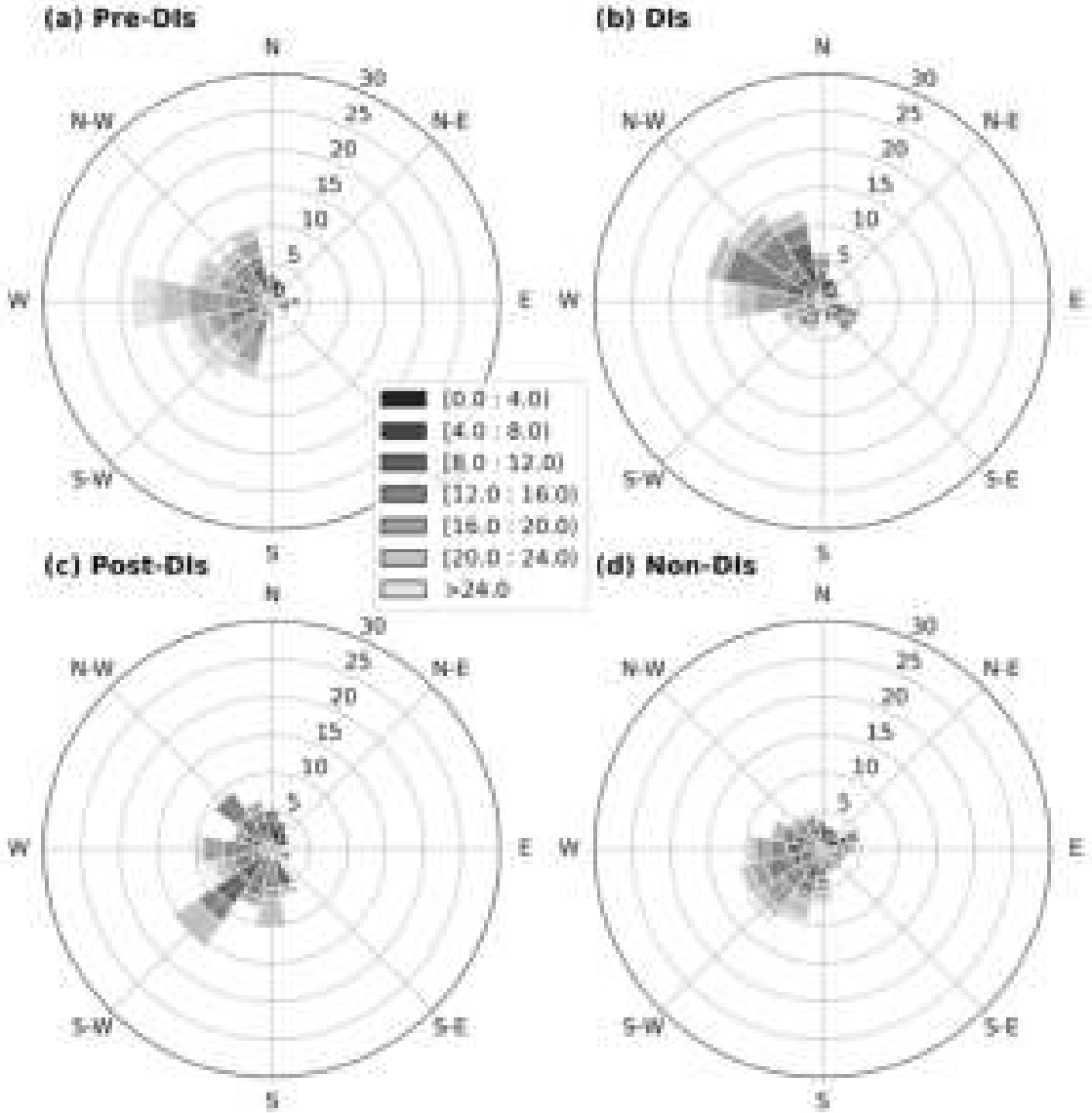


Figure 4.11: Wind roses for Brest-Guipavas in 500 m height with 00 and 12 UTC data, separated into the different categories (a) Pre-DIs, (b) DIs, (c) Post-DIs, (d) Non-DIs and colored according to the wind speed in m s^{-1} . The length of the bars indicates the wind direction frequency in %.

flow like the Post-DIs and the easterly flows are clearly the minority, with lower wind speeds than their southwestern counterparts.

In summary, during the course of a typical DI event, a slight wind shift from west during Pre-DIs over northwest under DIs and finally to southwest during Post-DIs is observed, whereby the southwest direction corresponds to the mean wind direction in Non-DIs. This matches the case study results almost perfectly. The west and northwest wind directions during Pre-DIs can be explained by a cold front passage, modifying the climatological southwest wind direction. Interestingly, the northwestern wind direction components are still retained in DIs, whereas the case study showed a quick recovery southwest wind directions.

Directly at the surface, more south-centered wind directions are measured, with DIs being the only category where northwestern directions dominate instead. Especially Pre-DIs and Non-DIs feature a large bar in the middle of south-southwest direction with a frequency of about 20%. For Non-DIs

this is more than double the frequency of any other bar, hinting at a possible distortion of the wind flow by the surface environment, since the southwest wind directions at 500 m height are distributed more evenly.

When separated into 00 and 12 UTC, the 500 m wind directions show only slight differences that do not change the interpretation presented here (not shown). While the Non-DI distribution of wind directions barely changes at all, the Pre-DI at 00 UTC features larger due west wind directions, whereas at 12 UTC the wind directions are more evenly distributed along the western half. A similar pattern as observed in Pre-DIs holds true for DIs, though with a slight rotation of about 30–45° to the north. But this pattern is not valid for Post-DIs, as both 00 and 12 UTC values show large variations, with the southwest direction being the dominant one at both times.

The average vertical profiles at Brest demonstrate a distinct PBL response to the passage of a DI that is marked by a cold, dry anomaly in the atmosphere, a deeper well mixed layer with potential instability and a wind shift with enhanced wind speeds, with the strongest winds at the surface during Pre-DIs. The separation into 00 and 12 UTC data reveals a nightly temperature inversion at the surface. However, the DI IQR showcases a large variability and in comparison to Ilotoviz et al. (2021), the temperature inversion at the top of the PBL is far weaker, in particular at 12 UTC. In order to learn, whether this difference simply arises from the averaging process due to a higher amount of identified DIs, or if such an inversion is not observed at all under some DI events, the following section investigates the variability of DIs at Brest.

4.4 DI variability at Brest

This section illustrates the variability in DIs and reveals important characteristics that are crucial for the interpretation of the averaged data. To this end, two different case studies are investigated. The first DI event is linked with the lowest specific humidity values at the surface during the entire radiosonde measurement period in the winter months from 1 December 2016 to 31 December 2022. The second DI event features the highest wind speeds associated with DIs in the winter months of the whole measurement period at the surface. Both events are identified with the 1-hourly synop data at Brest, in order to take impacts into account that occur at smaller time scales than the radiosonde interval of 12 hours. As in the average vertical profiles, only data in the winter months was analyzed.

4.4.1 DIs with lowest humidity at the surface

A visual inspection of the detected trajectories in Brest in the analyzed timeframe revealed that in a small subset of cases, trajectories are associated with anticyclones that cause strong anticyclonic curvature. In this subsection the DI event at the end of February 2018 is analyzed. This event led to the driest airmass over Brest during the whole analyzed winter period from December 2016 to December 2022.

Beginning on 25 February 2018 at 15 UTC, DIs were detected at Brest based on DI outflow data until 26 February 03 UTC. To analyze the flow of DI trajectories during that event, Figure 4.12 shows the pathway of all DI trajectories that are located in a 1° radius around Brest with a pressure value of at least 700 hPa at 21 UTC on 25 February 2018. This timestamp is selected because it features the most trajectories during the DI event.

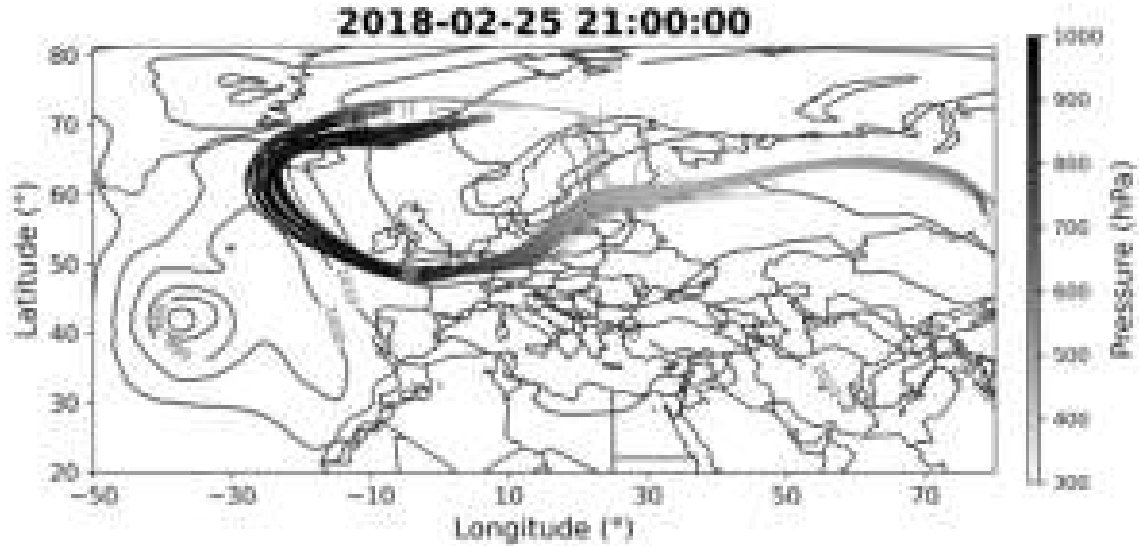


Figure 4.12: DI trajectories reaching Brest on 25 February 2018 at 21 UTC, colored according to their pressure in hPa. Additionally, isobars show the mean sea level pressure valid for the same time in blue and pressure values in hPa. The green circle marks the 1° radius around Brest.

The largest group of DI trajectories originates from continental Russia, at about the same longitude as eastern Kazakhstan. Starting originally into north- to northwestward direction at a pressure greater than 600 hPa, the trajectories quickly turn westward and gain altitude, as the pressure values decrease to about 500 hPa. On the way towards central Europe, individual trajectories that originate from Russia and northern Scandinavia join the large group of trajectories. Shortly after passing southern Finland, the trajectory flow starts to exhibit an anticyclonic curvature, as the trajectories pass over Poland, Germany, France, the North Atlantic and eventually end up over the Norwegian Sea. A strong pressure increase in the trajectories is observed between southern Finland and Brest, with pressure values rising from about 500 hPa to roughly 900 hPa. Over the ocean the trajectories remain at that height for a while, before rising back up with differing intensity. However, almost all trajectories end at a lower height than before the descending process.

This unusual trajectory course can be explained by the displayed isobars on 25 February 2018 at 21 UTC in Figure 4.12. A large high-pressure system over Scandinavia is visible, which is responsible for the anticyclonic curvature in the trajectories. Due to this system the 1020-hPa isobar is placed over Iceland, while a cyclone is displaced to the south of Iceland over the open North Atlantic ocean. This indicates a negative North Atlantic Oscillation (NAO). These abnormal circulation patterns are probably the result of a sudden stratospheric warming event and caused a severe cold spell over large parts of northern Eurasia (González-Alemán et al., 2022).

The evolution of the pressure variable (Figure 4.13) reveals a coherent set of trajectories that rises about 100–200 hPa prior to the descending period, corresponding to the large group of trajectories

that originated over central Russia. A few trajectories start with pressure values smaller than 600 hPa at -48 h. These are the trajectories that started closer to Europe. The outlier with a pressure value close to 800 hPa can be assigned to the trajectory that started in northern Sweden at the Norwegian border and cut through the other trajectories before ultimately joining them upon entering Germany. Almost the same behaviour in all trajectories is observed between -24 h and 80 h, before different groups emerge with varying ascent rates.

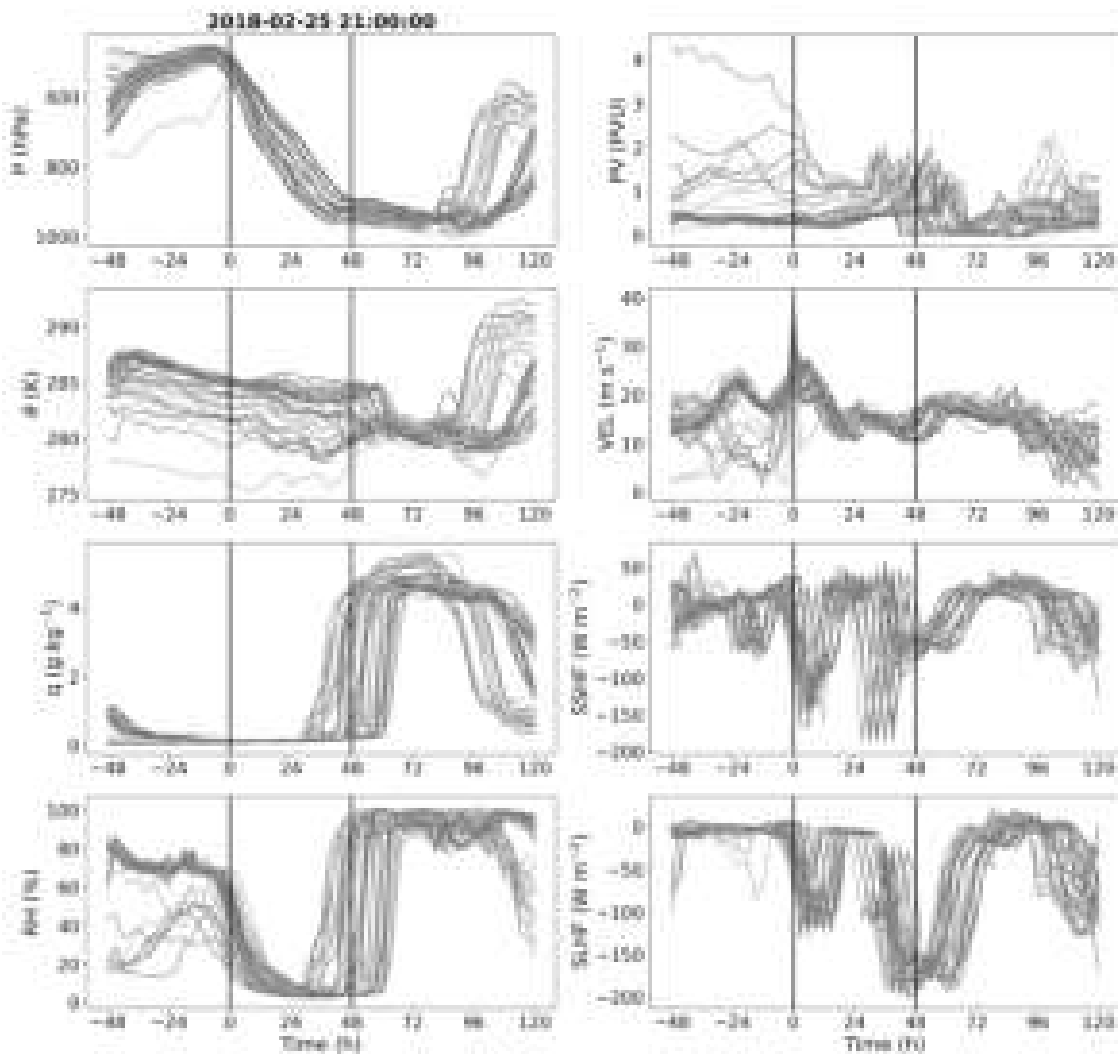


Figure 4.13: Variables traced along the DI trajectories as a function of relative time in hours with each line representing a trajectory. Variables include the pressure (hPa), potential temperature (K), specific humidity (g kg^{-1}), relative humidity (%), potential vorticity (PVU), velocity (m s^{-1}), surface sensible heat flux (W m^{-2}) and surface latent heat flux (W m^{-2}). Time 0 marks the start of the descending period and time 48 h the end of that period, both timestamps are marked with a vertical line in each plot. All shown trajectories reach Brest with a pressure of at least 700 hPa first at 25 February 2018, 21 UTC.

A small decline in potential temperature is generally evident from -40 to 48 h, probably caused by radiative cooling since it matches typical radiative cooling rates (Savijärvi, 2006). After 48 h, the variability is reduced, probably by mixing with the ambient air. Beginning at 96 h, similar ascending groups can be identified as in the pressure variable, indicating that diabatic processes like condensation occur during the ascent, thereby increasing the potential temperature of the

trajectories. This hypothesis is further supported by the specific humidity evolution that shows a strong decrease after 96 h, which is the expected outcome of condensation processes.

At the start of the specific humidity time series, very low values of $q \leq 1 \text{ g kg}^{-1}$ prevail in the trajectories, since all trajectories start relatively high in the atmosphere. However, until the start of the descending period at 0 h, the specific humidity value declines to values near 0 g kg^{-1} . After the first 24 h since the start of the descending period, some trajectories experience a rapid gain in specific humidity with values reaching above 4 g kg^{-1} before 48 h, while other trajectories remain near 0 g kg^{-1} until about 60 h. Although the timing of this humidity increase differs, the amount of this rise is similar. One explanation for this might be a different relative arrival time for the trajectories over Brest. Despite having the same actual arrival time at Brest on 25 February 2018 at 21 UTC, the relative times of this timestamp can vary, due to a differing location of the trajectories at the starting time of the descending period (0 h) and different velocities. This leads to earlier arrival in Brest in terms of relative time and consequently over the ocean for some trajectories. Since the trajectories are located over the ocean at a low elevation directly after passing Brest, ubiquitous moisture supply and thus an explosive specific humidity increase is to be expected. This implies that the trajectories with q values of more than 4 g kg^{-1} before 48 h are already located over the ocean at that time. Centering all trajectories at the time when they first reach Brest confirms this, as all specific humidity values are still below 3 g kg^{-1} at this time (not shown). Additionally, this reveals that the earliest trajectories shown in Figure 4.13 reach Brest already at a relative time of 36 h, whereas for most trajectories this is the case between 42 and 48 h.

Most trajectories display relative humidity values of about 50 % with a large spread at the starting time of the descent period at 0 h. These values decrease dramatically in the first 24 h of the descent, reaching values of below 10 % at about 24 h, indicating adiabatic warming during this phase. Afterwards, mixing with moister PBL air begins and the RH evolution displays the same behaviour as the specific humidity.

Only one trajectory exhibits PV values above 2 PVU consistently in the 48 hours before the start of the descending period, suggesting a stratospheric origin. However, in the majority of trajectories only values between 0 and 1 PVU are observed during the whole time series and almost all trajectories show PV values below 2 PVU. The PV evolution also reveals that the coherent trajectory set that originated from continental Russia has almost constant PV values of about 0.5 PVU between -48 and 0 h with small variability, whereas the other trajectories that originated closer to Europe show much higher PV values. This coherent set of trajectories is also traced in the velocity time series between -48 and 0 h, displaying small velocity fluctuations between 15 and 20 m s^{-1} , while the other few trajectories have smaller values with partially below 10 m s^{-1} . The highest velocity in the time series is reached in all trajectories at about the start of the descending period at 0 h and shortly after with values up to 25 m s^{-1} . Thereafter the speed decreases to about 15 m s^{-1} at 24 h and remains at those values until 96 h, where most trajectories show a slight decrease.

The surface heat fluxes are relatively low between -48 h and 0 h. But shortly after 0 h, both the sensible and latent heat flux are enhanced, reaching about the same magnitude of -100 W m^{-2} . This likely happens during the crossing of the Baltic Sea when cold surface air moves over the water

surface, gaining heat and moisture. Since the trajectories are still located at a high altitude during this point, this is not visible in other trajectory variables like specific humidity. At 24 h the surface heat fluxes are small again, presumably since the trajectories are located over land at this time. Subsequently, multiple trajectories show strong but isolated peaks, reaching almost -200 W m^{-2} , which is the largest value in the SSHF time series. Perhaps these peaks are caused by intense, early mixing with PBL air and an uptake of moisture, since the SLHF also shows these spikes, albeit much smaller and only reaching -100 W m^{-2} . An additional reason for higher SSHF values could be the anomalously cold air mass moving towards Brest. A much stronger signal in SLHF occurs around -48 h, when almost all trajectories drop below -150 W m^{-2} . However, the SSHF is much weaker at that time, centered at only -50 W m^{-2} . This means that the cause for the enhanced surface fluxes around -48 h is primarily the moisture uptake, also visible in specific humidity and relative humidity.

Based on the evolution of the DI trajectory variables, this appears like a normal DI event. However, the trajectory map in Figure 4.12 reveals that the trajectories are associated with an anticyclone, contrary to literature where DIs are commonly associated with cyclones (e.g. Browning (1997)). In order to analyze the impact on the PBL at Brest during this event, Figure 4.14 displays the five vertical profiles from 25 February 2018 00 UTC to 27 February 2018 00 UTC.

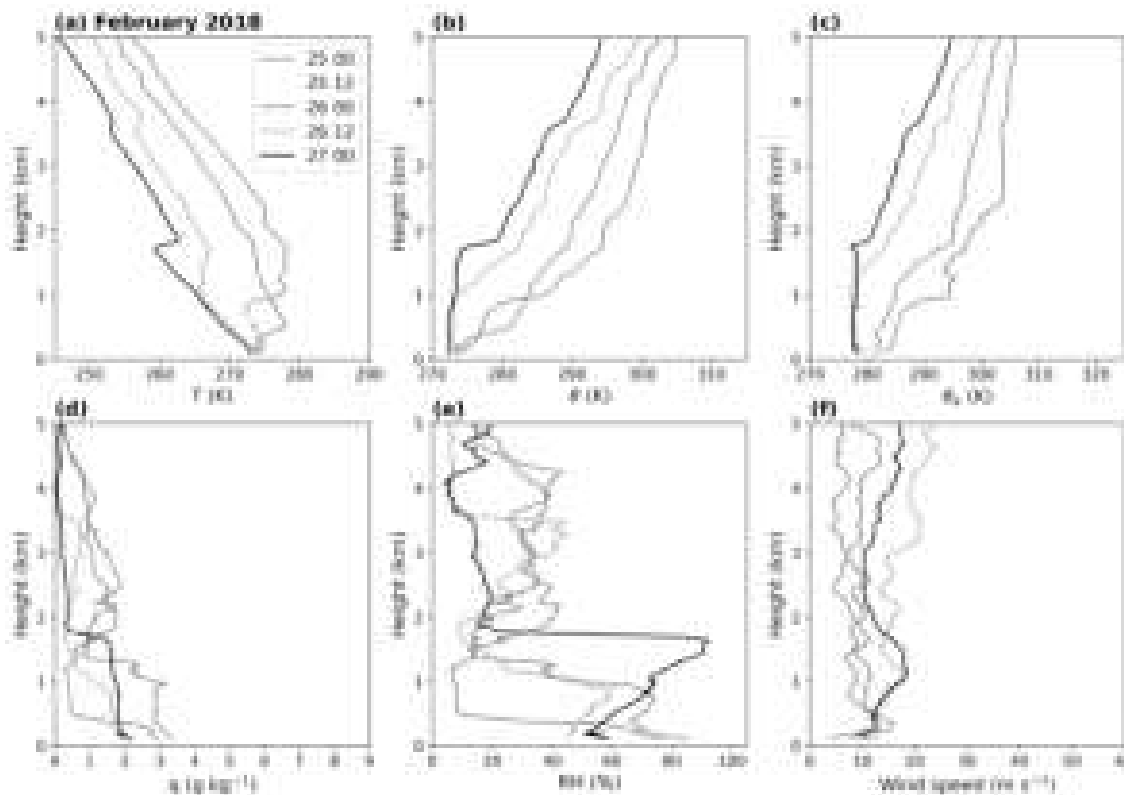


Figure 4.14: Vertical Profiles of (a) temperature (K), (b) potential temperature (K), (c) equivalent potential temperature (K), (d) specific humidity (g kg^{-1}), (e) relative humidity (%) and (f) wind speed (m s^{-1}) based on radiosonde ascents in February 2018 from 25 00 UTC to 27 00 UTC. The numbers in the legend denote day and time of the profiles in the format DD HH.

The first profile, classified as Non-DI, on 25 February 00 UTC is the only profile with a clear temperature inversion at the surface, followed by a much stronger inversion at about 1 km (Figure

4.14, a). It becomes the profile with the highest temperature values above 1.5 km. On 25 February 12 UTC the next profile, termed as Pre-DI, exhibits the warmest temperatures near the surface and shows a pronounced inversion at about 800 m. In the DI profile on 26 February 00 UTC, the temperature at the surface increases slightly with height until a rapid increase at about 400 m, marking the lowest temperature inversion of all profiles, except for the nightly surface inversion in the first Non-DI profile. The radiosonde ascent on 26 February 12 UTC, categorized as Post-DI, finds a quick reduction in temperature above the surface, forming the coolest atmospheric column observed so far. Besides, only small temperature inversions in the atmosphere can be detected, the first at about 1.1–1.2 km. The last analyzed profile on 27 February 00 UTC, classified as Non-DI, reveals the coldest airmass in the entire atmospheric column with a strong temperature inversion at a height of approximately 1.8 km. Interestingly, no temperature inversion at the surface occurred. This could indicate a moderate wind speed as cold air is advected with the easterly flow, seen in Figure 4.12.

The observed temperature inversions are also visible in the potential temperature profiles (Figure 4.14, b). Additionally, they show a well mixed layer of constant θ starting from the surface during Pre-DI, Post-DI and second Non-DI, with the shallowest layer occurring under Pre-DIs up to 600 m and the deepest layer during the second Non-DI up to 1.8 km. Slight instability is observed during Post-DIs, as θ values decline from the surface during the first 100 m. On the other hand, the DI and first Non-DI show an almost steady increase of potential temperature and a stronger increase at the height of the observed temperature inversions. Thus, these profiles indicate that the smallest PBL height occurs during the DI. This is a direct contradiction to the normal behaviour of DIs, since they are commonly associated with higher PBL altitudes (e.g. Ilotoviz et al. (2021)).

Interestingly, the profiles of equivalent potential temperature θ_e (Figure 4.14, c) appear relatively similar as the profiles of θ , suggesting a low influence of moisture. Differences include a cooler Post-DI than the second Non-DI at about 1 km, a slower increasing DI in the lowest 1 km and the Pre-DI smaller than the first Non-DI between 0.8–1.3 km. Indeed, those differences are caused by moisture differences, as the specific humidity profiles (Figure 4.14, d) reveal. Anomalously small specific humidity values are observed in all profiles, since the eastern flow advects cold and dry continental air. The first Non-DI profile still has the highest values of specific humidity of all profiles on average but exhibits a drier layer between 1.4 and 2 km. Apparently, this dry layer descends with time, as it is located at about 800 m during the Pre-DI and begins already at 400 m during the DI profile. While the Post-DI is not quite as dry as this dry layer in the DI profile, it is the driest profile at the surface and far drier than all previous profiles. This suggests that the DI air mixed with the moister PBL air at the surface. Above 1 km the specific humidity in the Post-DI radiosonde ascent decreases and is only matched by the second Non-DI. Although the second Non-DI profile shows even lower q values between 2 and 4 km than the Post-DI, at the surface a recovery to slightly higher q values is measured.

Despite the low specific humidity values, the relative humidity (Figure 4.14, e) displays relatively normal values at the surface in all radiosonde ascents, ranging from about 45 % at Post-DIs to about 85 % during the first Non-DI. These high RH values are facilitated due to the cold temperatures, since colder air can store less water vapour. The same effect in reverse causes sharp RH gradients

at the altitudes where the respective temperature inversions are observed. The DI profile is the only case with no increase in RH before the sharp reduction.

In general, all radiosonde ascents show relatively low wind speeds throughout the considered atmospheric column (Figure 4.14, f). By far the lowest wind at the surface is visible during the first Non-DI, which is presumably the reason for the temperature inversion at the surface. The strongest wind speed at the surface and also above 2 km is observed under the Post-DI, followed by the second Non-DI. Pre-DI, DI and first Non-DI show weaker values almost at every height. A comparison with the DI IQR in Figure 4.9 reveals that the wind speed values in the shown DI profile on 26 February 2018 at 00 UTC are smaller than the 25th percentile above 3 km, highlighting the rarity of this DI passage. Low wind speeds near the surface during the Pre-DI radiosonde observation suggest that probably no front passage occurred before the DI.

A detailed overview of important weather parameters at the surface is offered by the time series of station measurements during this DI event, shown in Figure 4.15. The pressure measurements (Figure 4.15, a) reveal a slight increase of about 6–7 hPa from the start of the time series on 25 February 2018 at 00 UTC to 26 February at 12 UTC. This pressure increase is caused by the retrograde expansion of the cold anticyclone over Scandinavia.

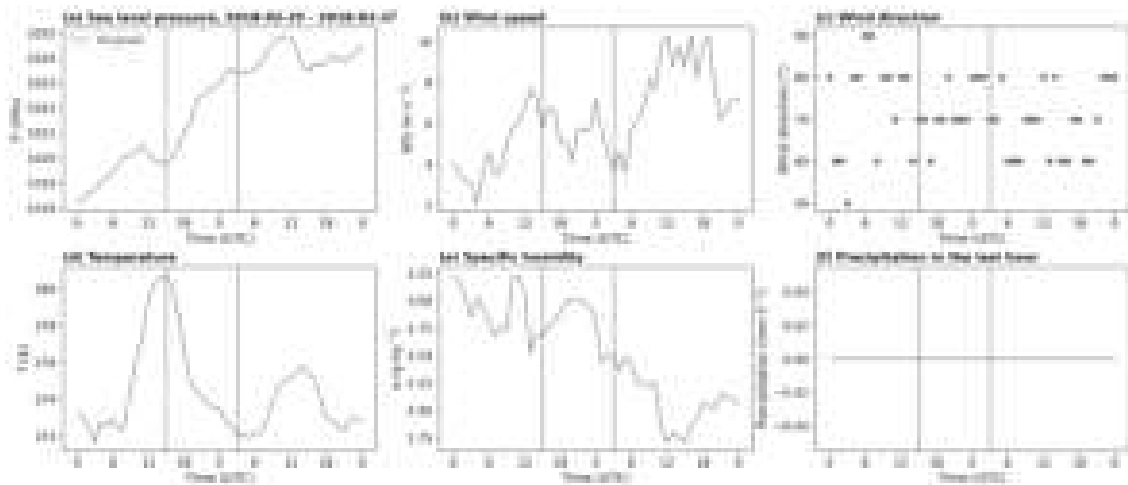


Figure 4.15: Synop observations at Brest from 00 UTC on 25 February to 00 UTC on 27 February 2018. Shown variables include (a) sea level pressure (hPa), (b) wind speed (m s^{-1}), (c) wind direction ($^{\circ}$), (d) temperature (K), (e) specific humidity (g kg^{-1}) and (f) hourly precipitation (mm h^{-1}). The onset and end of the DI event are marked by red vertical lines.

The wind speed (Figure 4.15, b) starts with a low value of 4 m s^{-1} and decreases further during the night, favoring the temperature inversion near the surface that was observed in the radiosonde ascent. Shortly before the onset of the DI event, the wind speed spikes at 13 UTC on 25 February 2018, but remains below 8 m s^{-1} . During the DI event low wind speed values between 4 and 8 m s^{-1} are measured. After the DI period, the wind increases in the course of the next day to the highest values in the time series of about 10 m s^{-1} . These observations are consistent with the radiosonde measurements and indicate an intensifying cold air advection on the second day. Advection of cold and dry continental air over the whole time series due to an almost constant east-northeast wind direction (Figure 4.15, c) is likely.

This hypothesis of a continuous continental air advection is also supported by the temperature and specific humidity time series (Figure 4.15, d,f), as the specific humidity starts at very dry values of about 3 g kg^{-1} that are already highly anomalous for Brest, because it is located in a sheltered bay close to the North Atlantic coast. On the second day, temperature and specific humidity decrease further as the cold air advection intensifies. The maximum temperature of approximately 276 K is unusually cold for Brest due to the influence of mild ocean waters during normal conditions. However, the specific humidity value at the Post-DI on 26 February 12 UTC of about 1.75 g kg^{-1} is extremely anomalous and lower values in the whole analyzed period of winter months from December 2016 to December 2022 are only observed during the following two days on 27 and 28 February 2018 as the cold spell continues to intensify.

Unsurprisingly, no precipitation occurred during the entire time series (Figure 4.15, f). The evolution of the described variables at the surface suggests that, contrary to typical DI events, no frontal passage preceded the DI or occurred at all during the time series. The lack of a surface front is also confirmed by mean sea level pressure analysis charts with fronts, air pressure and weather observations by the German Weather Service (Deutscher Wetterdienst, 2020). Additional major differences include the very stable atmosphere and the extremely low PBL altitude during DIs, as well as low wind speeds overall with a nearly constant wind direction, resulting in a highly unusual and unexpected DI event.

4.4.2 DIs with highest windspeeds at the surface

This subsection investigates the DI event related to the highest wind speed in the winter period from 2016–2022 at Brest, namely the DI event from 16 February 2020 18 UTC to 17 February 2020 03 UTC, lasting only 9 hours. On 16 February 2020 at 05 UTC, the highest 1-hourly mean wind speed in the whole analyzed winter time series was measured with 19 m s^{-1} , according to the synop data. The fact that this largest wind speed is associated with a DI event underlines the importance of DIs for high impact weather. The pressure system setup during this event is basically the opposite of the anticyclonic DI case, as it features a large Azores High and a deep extratropical cyclone, centered southeast of Iceland (Figure 4.16), resulting in a positive NAO index with strong westerly winds around Brest.

DI trajectories start mainly over the Labrador Sea at widely varying pressure levels. At this point, the isobars in Figure 4.16 should not be used for interpretation of the trajectory flow, since the isobars are only valid for the first timestamp once all trajectories reach Brest. When the trajectories exit the Labrador Sea south of Greenland, they become more compact and the pressure levels are more similar than before. However, one outlier trajectory is detected south of the main bundle of trajectories and at a higher altitude. During their way over the North Atlantic, the trajectories descend from about 500 hPa to approximately 900 hPa when they first reach Brest on 16 February 2020, at 21 UTC. The trajectory direction of motion changes from due west to west-northwest after Brest is passed. This cyclonic curvature suggests that the influence of the Icelandic Low prevails in the region around Brest. All trajectories remain at lower levels than before the descent as they reach their endpoint over northern continental Russia.

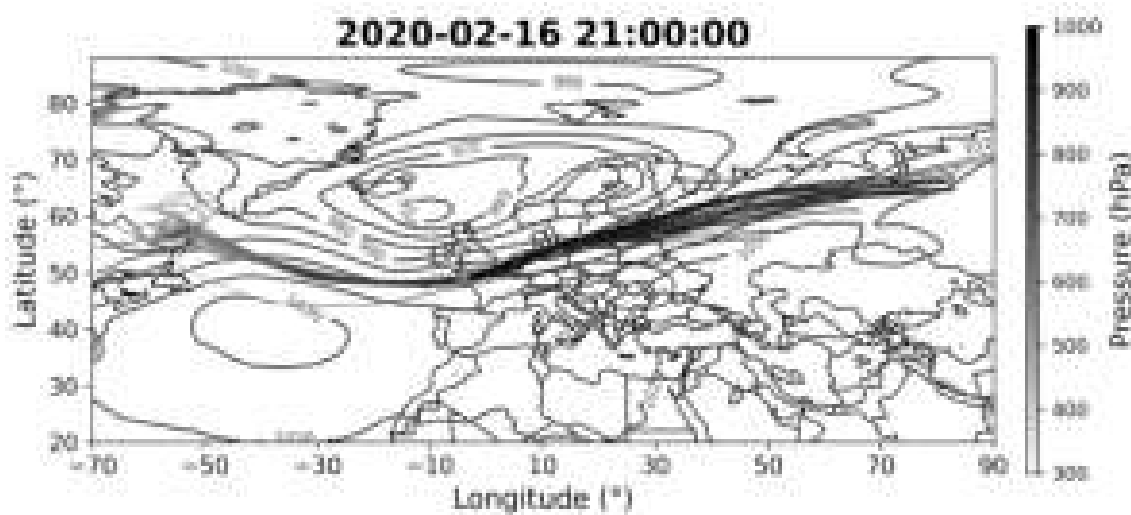


Figure 4.16: DI trajectories reaching Brest on 16 February 2020 at 21 UTC, colored according to their pressure in hPa. Additionally, isobars show the mean sea level pressure valid for the same time in blue and pressure values in hPa. The green circle marks the 1 ° radius around Brest.

The evolution of pressure along the trajectories illustrates the differences at the starting point of -48 h much clearer (Figure 4.17) and allows the identification of different groups. The largest group is located between about 700 and 900 hPa, while a smaller group of trajectories starts around 500 hPa and a single trajectory close to 300 hPa. Both the large group at the lower altitude and the single trajectory at the higher altitude merge with the other group at approximately 500 hPa at 0 h. Between 0 and 24 h a strong but unsteady descent of 400 hPa is observed, since this is exactly the DI criterion which selected those trajectories initially. Only few trajectories rise to a pressure level smaller than 800 hPa after 96 h, whereas the majority of trajectories remains at a pressure level greater than 800 hPa.

Improved visibility of the different groups is offered by the evolution of the potential temperature, as the two groups are more compact than before and the individual trajectory exhibits far higher values than all other trajectories at -48 h. Between -48 and 0 h, the large group of trajectories experiences an increase in potential temperature which merges it with the other group at 0 h. This increase is presumably caused by diabatic heating due to condensation of water vapor. Surprisingly, the potential temperature of all trajectories, except the individual trajectory, increases after the start of the descending period between 0 and 24 h. After 24 h, the potential temperature of the individual trajectory decreases strongly and reaches similar values as the other trajectories at 48 h. This decrease may be caused by diabatic cooling due to evaporation into the dry air mass. In the last period between 48 and 120 h the trajectories remain at constant values or decrease slightly, possibly indicating radiative cooling.

During the start period before the descent, the specific humidity shows two different trajectory groups, one with values close to 0 g kg^{-1} and the other one with values visibly larger than that. At 0 h, specific humidity values are close to zero in all trajectories. Unexpectedly, a gradual increase in q is observed in all trajectories already at 12 h, becoming larger with time until the maximum

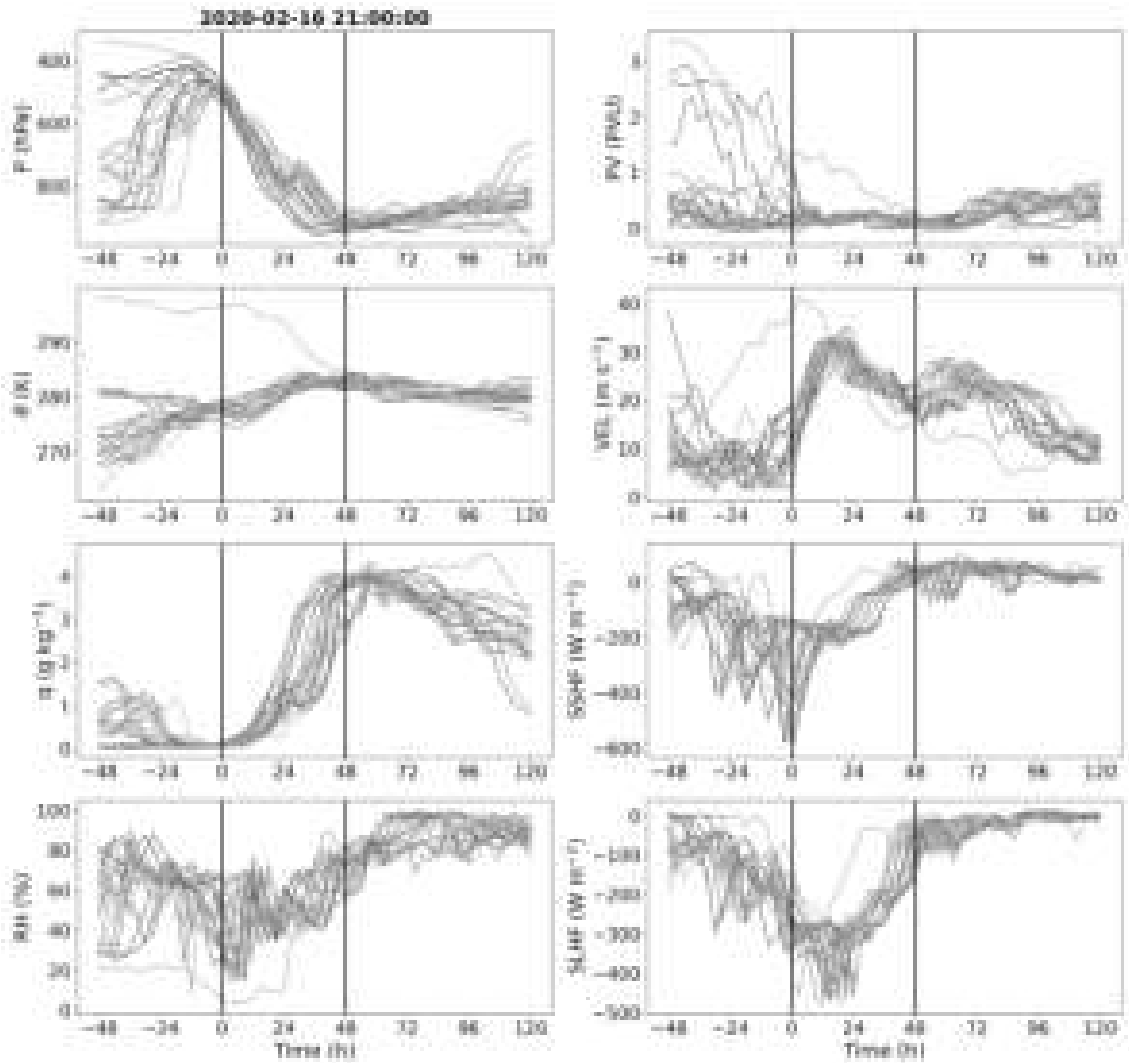


Figure 4.17: Variables traced along the DI trajectories as a function of relative time in hours with each line representing a trajectory. Variables include the pressure (hPa), potential temperature (K), specific humidity (g kg^{-1}), relative humidity (%), potential vorticity (PVU), velocity (m s^{-1}), surface sensible heat flux (W m^{-2}) and surface latent heat flux (W m^{-2}). Time 0 marks the start of the descending period and time 48 h the end of that period, both timestamps are marked with a vertical line in each plot. All shown trajectories reach Brest with a pressure of at least 700 hPa first on 16 February 2020, 21 UTC.

specific humidity values are reached at 48 h with $3\text{--}4 \text{ g kg}^{-1}$. These values stay approximately constant for about 24 h, before a small decline starts at 72 h.

While the single trajectory can also be identified in the relative humidity evolution as the trajectory with by far the lowest values between -48 and 0 h, the other two groups are mixed. A large variability between different trajectories exists from -48 h to 24 h. Remarkably, only a few trajectories reach relative humidity values below 20 % after the start of the descending period and at 12 h most trajectories exhibit relative humidity values above 40 %. During this period, a relative humidity decrease to minimal levels is expected (Raveh-Rubin, 2017), since the descending DI air parcels typically warm adiabatically. However, the evolution of θ and q suggest a non-adiabatic descent, as both show an increase of heat and moisture during the first phase of the descent. After 24 h the

relative humidity of DI air parcels increases to values between 80 and 100 % at about 72 h and remains at those levels for the rest of the time series.

The single trajectory features the highest PV values at -48 h with more than 3 PVU, but decreases to about 1.5 PVU at 0 h. Three other trajectories also show PV values partially above 2 PVU in this time period before they also decreased drastically at 0 h. Such high PV values could suggest a stratospheric origin, but since these high values are not consistent between -48 and 0 h, they do not fulfill the criterion of stratospheric DIs employed in Raveh-Rubin (2017). Most trajectories remain between 0 and 1 PVU throughout the whole time series, indicating mostly tropospheric trajectories. In terms of velocity the majority of DI air parcels moves relatively slow before the descending period (-48 h – 0 h) with 10 m s^{-1} and reach their peak at 24 h or slightly before with 30 m s^{-1} . Thereafter the velocity declines.

Surface heat fluxes show large values right from the start in some trajectories and intensify with time. The SSHF reaches the minimum at the start of the descending period, with individual trajectories reaching below -500 W m^{-2} . However, a substantial variability exists at this point, as the lowest magnitude of the SSHF is approximately -150 W m^{-2} . The magnitude of the SSHF decreases swiftly to about -200 W m^{-2} at 24 h, with only a small variability at this point, before decreasing further to values around 0 W m^{-2} at approximately 36 h. Surprisingly, the SLHF is smaller at 0 h, exhibiting values of about -300 W m^{-2} . The maximum magnitude of the SLHF is reached between 0 and 24 h, with values extending below -400 W m^{-2} . This maximum is followed by a sharp reduction, similar to the one in SSHF, that leads to values close to 0 after 72 h. One possible explanation for this reduction is that the trajectories started to move over land at that time, instead of ocean, since the surface heat fluxes are generally enhanced over the ocean compared to land. Perhaps a cold air outbreak that led to cold air moving over the warmer ocean surface favored the observed high surface fluxes.

Radiosonde profiles of the temperature in the lowest 5 km of the atmosphere (Figure 4.18, a) reveal a stark difference between the first two profiles before the DI event and the last three profiles once the DI event started. The first profile on 16 February 00 UTC, classified as Non-DI, and the second profile, termed as Pre-DI at 12 UTC on the same day, both show markedly higher temperatures throughout the entire considered atmospheric column than the later 3 profiles. This difference suggests that the DI arrival is preceded by a pronounced cold front. Additionally, the temperature decreases slower with height than in the last 3 profiles, probably indicating a moist adiabatic lapse rate. A small inversion slightly above 1 km is visible in the first profile, while the Pre-DI profile displays no inversion and is thus cooler than the first Non-DI, beginning from that altitude. The DI radiosonde ascent on 17 February at 00 UTC features a minimal surface inversion and a weak temperature inversion at a higher altitude is only observed at about 3.4 km. However, a constant gradient is shortly visible at 1.5 km. In the following profile of the Post-DI on 17 February 12 UTC no inversion is detected at all, only small parts with a near constant gradient. The last profile of the second Non-DI on 18 February 00 UTC showcases a nightly surface inversion and a weak inversion short of 5 km.

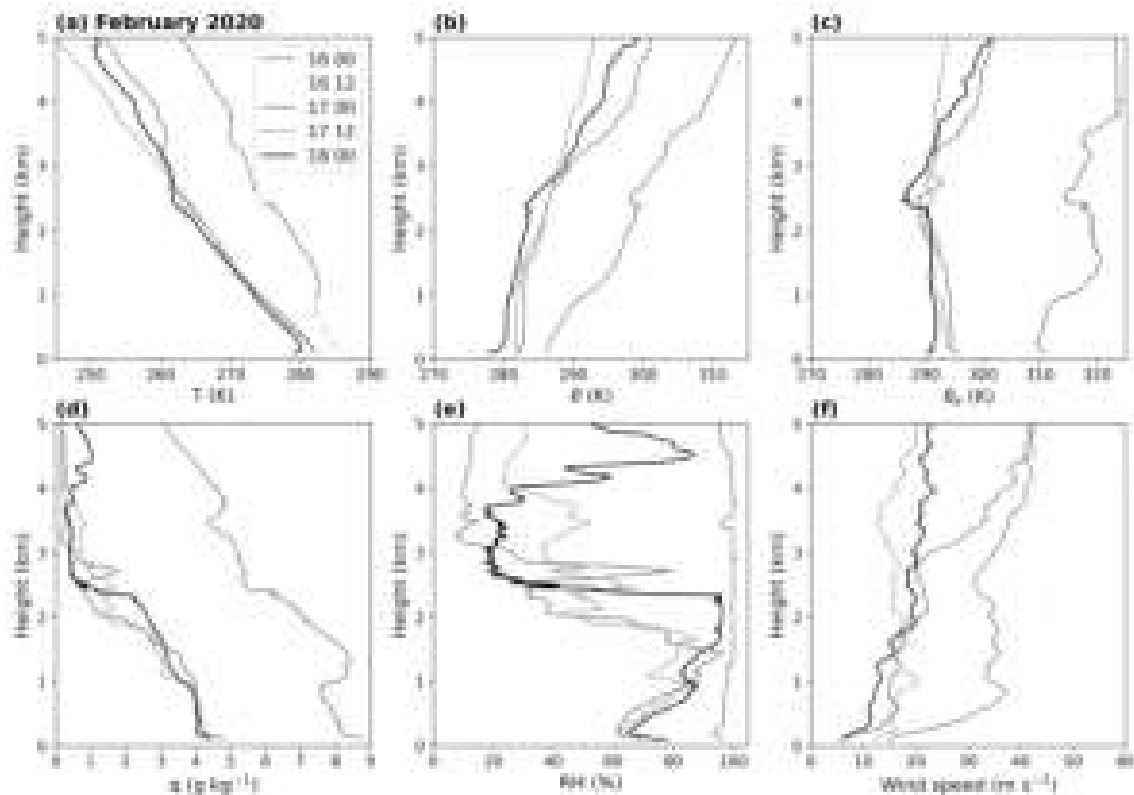


Figure 4.18: Vertical Profiles of (a) temperature (K), (b) potential temperature (K), (c) equivalent potential temperature (K), (d) specific humidity (g kg^{-1}), (e) relative humidity (%) and (f) wind speed (m s^{-1}) based on radiosonde ascents in February 2020 from 16 00 UTC to 18 00 UTC. The numbers in the legend denote day and time of the profiles in the format DD HH.

In the first two radiosonde ascents from the surface increasing potential temperature is found (Figure 4.18, b), indicating static stability. On the other hand, the later three profiles present well mixed PBLs, indicated by a near constant potential temperature. During DIs the most constant and highest layer of such a potential temperature behaviour is identified, stretching from a few hundred meters above the weak surface inversion layer to a height of about 1.5 km. In the profiles of the Post-DI and second Non-DI the constant potential temperature only reaches up to 1 km. A slight decrease is measured from the surface at the Post-DI ascent, whereas the second Non-DI shows an increase due to the nightly inversion. The non-existent temperature inversions complicate the estimation of the PBL height during the Post-DI and second Non-DI, as multiple small increases in potential temperature occur above 1 km.

An enlarged difference between the first two profiles and the last three is displayed in the θ_e profiles (Figure 4.18, c), indicating an enhanced moisture content in the first two profiles, since θ_e combines the differences in moisture and temperature. After a slight decrease above the surface, possibly caused by large humidity values due to the influence of the neighboring ocean at the surface, the first Non-DI and Pre-DI profiles increase with height. In contrast, the later three remain roughly constant and even decrease slightly with height, reaching a minimum between 2 and 2.5 km. Above that point the θ_e values during DI and second Non-DI increase. Interestingly, the largest values in the analyzed 5 km during Post-DIs are found at the surface, suggesting potential instability in the entire considered atmospheric column.

Specific humidity profiles (Figure 4.18, d) reveal the largest visible difference between the profiles before the onset of the DI event and after. The values at the surface during the first two profiles are approximately 4 g kg^{-1} larger than during the last three profiles and although this difference decreases with height, it is still apparent at 5 km height. The lower troposphere appears saturated regarding water vapor, as the relative humidity profiles (Figure 4.18, e) during the first two profiles remain mostly near 100 %. This supports the hypothesis of a moist adiabatic lapse rate, whereas the later three profiles decrease with a dry adiabatic lapse rate, explaining their larger decrease in temperature with height. After experiencing a local minimum at about 100 m above the surface, the relative humidity of the last three profiles increases. However, this increase is partially interrupted by sudden decreases with a sharp gradient, which complicates an unequivocal determination of the PBL height. Maximum RH values are reached at about 1.5 km for DI, at 1.8 km for Post-DI and at 2.4 km for the first Non-DI profile.

A marked difference is also obvious in the wind speed profiles (Figure 4.18, f), as the first two radiosonde ascents show much higher wind speeds than the later three ascents. At the surface, the highest wind speed is observed under the first Non-DI and the lowest under the second Non-DI, favoring the observed surface temperature inversion in the second Non-DI. Above the surface, the Pre-DI profile increases explosively to 40 m s^{-1} at just 800 m, closely followed by the first Non-DI. The Pre-DI wind speed increases further above 3.5 km, reaching almost 60 m s^{-1} above 4 km, which is the largest value at that height. Although the DI profile exhibits much lower values below 3 km than the first two radiosonde ascents, it is still matching or even partially exceeding the 75th percentile of all DI wind speeds (Figure 4.9), before vastly exceeding that mark above 3 km. Therefore, this event not only features the highest wind speed at the surface before a DI, but also one of the highest wind speeds during DIs, in particular above 3 km.

The observations in the vertical profiles do not allow an unequivocal height identification of the PBL layer. Another approach for this are ceilometer measurements. These measurements reveal a pronounced maximum at a height of about 200 or 300 m and no visible values above 500 m during the first 12 hours from 16 February 00 UTC to 12 UTC (not shown), similar to the measurements in Figure 4.6 shortly before 12 UTC on 20 February 2020. This indicates precipitation and is in agreement with the moist adiabatic stratification found in the first two radiosonde ascent profiles. After 12 UTC on 16 February a large variability occurs, as the signal initially rises up to 2.5 km in 2 h, just to fall below 1 km again after the next 2 h at 16 UTC. At 18 UTC the clear backscatter maximum in the atmosphere disappears. A weaker signature of the transition to lower values appears at a height between 1 and 1.5 km. From 21 UTC onwards isolated maxima occur in the atmosphere, first partially and then more frequent after 06 UTC on 17 February. However, these maxima largely remain between 1 and 1.5 km, marking the top of the PBL. Such a PBL height between 1 and 1.5 km could also be supported by the radiosonde observations, as this is one of multiple regions with a rapid decrease in relative humidity and an increase in potential temperature during the DI, Post-DI and second Non-DI profile.

Additionally, the vertical profiles reveal that the highest wind speeds near the surface are already reached in the cold front preceding the DI and quickly subside once the DI arrives. A more detailed overview over the evolution of the surface weather at Brest is given in Figure 4.19, based on

1-hourly synop data. The pressure evolution (Figure 4.19, a) displays a small decline in the first 12 hours of about 5 hPa, followed by a pressure increase that lasts through the entire time series as the pressure increases from short of 1000 hPa on 16 February 12 UTC to more than 1025 hPa on 18 February 00 UTC. These changes can be explained by the pressure systems shown in Figure 4.16. Brest is located between an extratropical cyclone southeast of Iceland and an Azores High and while the influence of the Iceland Low causes the small decline in the first 12 hours, the influence of the Azores High ultimately prevails as it expands more towards Brest, causing the increasing pressure values during the rest of the time series.

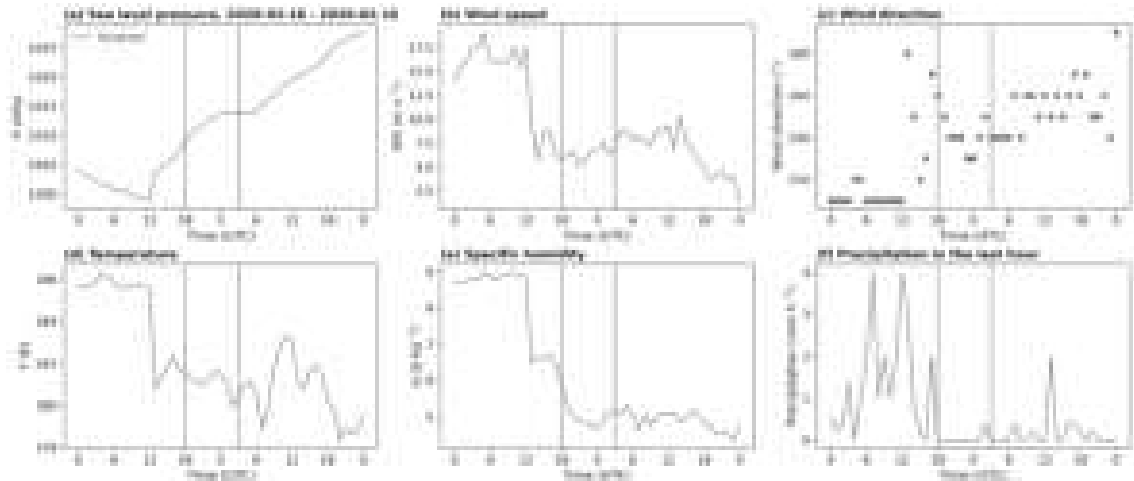


Figure 4.19: Synop observations at Brest from 00 UTC on 16 February to 00 UTC on 18 February 2020. Depicted variables include (a) sea level pressure (hPa), (b) wind speed (m s^{-1}), (c) wind direction ($^{\circ}$), (d) temperature (K), (e) specific humidity (g kg^{-1}) and (f) hourly precipitation (mm h^{-1}). The start and end of the DI event are marked by red vertical lines.

Therefore, the highest wind speeds are expected to occur in the first 12 hours when the influence of the extratropical cyclone still dominates. The highest wind speeds are indeed reached in the first 12 hours and suddenly decrease about 10 m s^{-1} after that (Figure 4.19, b). The wind speed of 19 m s^{-1} , reached at 5 UTC on 16 February, is the highest 1-hourly mean wind speed in all winter months of the whole analyzed period from December 2016 to December 2022. Even the wind speed of 17.5 m s^{-1} , which is reached four times in the first 12 hours, occurs only during this DI event. The highest wind speed not related to this DI event in the whole analyzed time period is 17 m s^{-1} . Towards the end of the time series after about 15 UTC on 17 February, the wind speed decreases further, dropping below 2.5 m s^{-1} on 18 February 00 UTC, which marks the lowest wind speed in the displayed time series. Although the radiosonde observations show that the wind speed is lowest during this time too, it is still much higher in the radiosonde ascent with 6 m s^{-1} as the lowest value of the vertical profile during that time.

During the first 12 hours a southwesterly wind direction is observed ($210\text{--}220^{\circ}$), followed by an abrupt shift to a westerly wind direction (280°) at 13 UTC on 16 February (Figure 4.19, c). However, this wind shift is not stable, as the wind direction switches between west and southwest during the next hours. Beginning at 20 UTC on the same day, a southwesterly wind direction becomes stable again, although it is turned about 30° to a more westerly wind direction compared to the start of

the time series. On the next day after about 9 UTC, the main wind direction changes to west (260°). The sudden wind shift between 12 and 13 UTC on 16 February could indicate a cold front.

The assumption of a cold front is further supported by the temperature and specific humidity time series (Figure 4.19, d,e), as both reveal a large drop at 13 UTC. Afterwards the temperature recovers slightly before a small and unsteady decrease begins, lasting until 7 UTC on the next day. A slight increase from 13 to 16 UTC on 16 February is also visible in the specific humidity, followed by a larger decrease as the DI event begins at 18 UTC on the same day to values around 5 g kg^{-1} . Specific humidity remains around those values through the rest of the time series. While the specific humidity is much lower after the onset of the DI event than during the first 12 hours of the time series, the value of 5 g kg^{-1} is still relatively high, especially compared to the anticyclonic DI event analyzed in the previous subsection which featured mostly values below 3 g kg^{-1} . These comparatively higher values are probably caused by moisture advection from the ocean near the surface due to the southwesterly to westerly wind direction. As Figure 4.16 shows, most DI trajectories penetrate below the 900 hPa level over the ocean before they reach Brest, leading to enhanced mixing with the moister PBL air over the ocean surface.

Precipitation evolution (Figure 4.19, f) confirms the previous analyses, as it exhibits rain during almost the entire first 17 hours before the DI arrival, with the exception being 4 and 16 UTC. This precipitation period caused the maximum backscatter values near the surface in the ceilometer measurements. The highest rain rate of 4 mm h^{-1} is reached at 7 and 12 UTC. After the peak at 12 UTC, the rain intensity quickly subsides, though one further peak of 2 mm h^{-1} is observed at 17 UTC. During the DI period dry conditions prevail, only a small intensity rain is observed near the end of the DI period at 2 UTC on 17 February. Afterwards precipitation returns, but the intensity values remain mostly lower than during the period before the DI occurrence. A surface front analysis (Deutscher Wetterdienst, 2020) reveals that a warm front crosses Brest as early as 18 UTC on 15 February, possibly causing the extended rain period at the start of the synop measurements. Previous assumptions about a cold front based on the measurements are confirmed, since a cold front arrives at Brest on 16 February shortly after 12 UTC (Deutscher Wetterdienst, 2020).

The two examined DI events in this section revealed substantial differences, with the most important one being the lack of a front preceding the DI in the anticyclonic DI case. Due to the missing front, the wind speeds were lowest before the anticyclonic DI event. The opposite is valid for this event which shows a larger extratropical cyclone influence, indicated by the weak cyclonic curvature in the trajectories. High impact weather, including the highest 1-hourly mean wind speeds during the whole analyzed winter period and precipitation, occurred during the frontal passage preceding the DI. Another noteworthy difference is the specific humidity, where the lowest values in all winter months from December 2016 to December 2022 occurred in association with the anticyclonic DI event, caused by an easterly flow of cold and dry continental air. While this may seem like a clear indication of a typical DI event, DIs are more commonly associated with extratropical cyclones (e.g. Carlson (1980), Browning (1997), Raveh-Rubin (2017)). The missing preceding front underlines the rarity of such an event, since Ilotoviz et al. (2021) found all DIs preceded by detectable fronts. Naturally, this could be caused by the fundamentally different synoptic environments, as their analyzed site in the Azores is unable to experience cold continental air advection. In contrast to

the anticyclonic DI event, the more typical DI events influenced by extratropical cyclones exhibit relatively larger specific humidities, due to intense mixing with the underlying moist PBL air which originates in most cases from the North Atlantic.

The stark difference between the temperature inversion during DIs in the average vertical profile at Brest in this thesis and at a station in the Azores in Ilotoviz et al. (2021) partially motivated this section. The temperature inversion above 1.5 km was one of the most prominent features in the PBL response to DIs found by Ilotoviz et al. (2021). In contrast, the temperature inversion is strongly reduced in the average vertical profile at 00 UTC and barely visible in the average profile at 12 UTC at Brest.

This section demonstrated that this difference occurs both due to the averaging process and due to the inherent lack of a temperature inversion in some DI profiles. If all temperature inversions were located at different heights, e.g. 400–500 m in the anticyclonic case instead of the 1.5 km in the average profiles, then no inversion at all could be observed in the resulting average. However, as the last DI event associated with the high wind speeds showed, some DI profiles simply do not have a temperature inversion at the height of a typical PBL altitude.

Naturally, these findings are based only on two individual DI events and may therefore not be representative of all other DI occurrences. But since it is not feasible to analyze all DI events at Brest in this depth, a coarser approach is utilized to test these findings at least partially. For the DI events in February 2020, which was the winter month with the third highest DI acitivity in Brest in the period 1979–2022 (Figure 4.8), maps of the trajectory pathway and the corresponding individual vertical profiles based on radiosonde ascents are plotted. Visual inspection reveals trajectory pathways that form an anticyclonic loop due to a high pressure system west of Brest, beginning on 4 February 2020 12 UTC and lasting with a brief interruption until 6 February 18 UTC. This suggests a clear anticyclonic influence.

Other DI trajectories during that month show more ambiguous pathways, as the trajectories exhibit only a weak anticyclonic curvature over the open North Atlantic, e.g. in the DI event on 20 February 18 UTC shown in Figure 4.1, while they are also partially influenced by an extratropical cyclone close to Iceland. Moreover, some DI trajectories travel from Newfoundland to Brest in an almost straight line.

The corresponding vertical profiles show distinct temperature inversions especially during the anticyclonic DI cases mostly spread around 1.5 km height. At the end of the anticyclonic DIs the inversion descends to lower levels of only about 400 m, analogical to the analyzed anticyclonic DI case at the end of February 2018. Multiple DI profiles that are associated with almost no curvature in the trajectories before they reach Brest show almost no inversion at all, similar to the DI case study with the highest wind speeds on 17 February 2020. However, temperature inversions near a typical PBL height are observed in the trajectories that show a weak anticyclonic curvature over the North Atlantic, as the case study at the start of this chapter illustrates (Figure 4.1 and 4.4).

Based on these results, the assumption may be formulated that temperature inversions during DIs, marking the height of the PBL, occur most frequently under the (partial) influence of a high pressure system. This hypothesis could also explain the pronounced temperature inversion at a radiosonde station in the Azores during DIs, found by Ilotoviz et al. (2021), as the Azores are often influenced

by the Azores High. While the approach of a visible inspection of the DI events might suffice for a qualitative assessment, it is still limited to the DI events in February 2020. Therefore, a quantitative assessment over a longer period would be needed to confirm the aforementioned assumption. Future work could create a sophisticated way of separating the DI events into anticyclonic and cyclonic groups, based on the curvature of the trajectories. However, this level of detail is beyond the scope of this work, since the initial focus was to analyze DI events and their differences across different stations in western Europe, which is the topic of the following section.

4.5 Lower tropospheric structure during DIs at other stations

Radiosonde observations from several other stations over western Europe are utilized in order to identify differences and similarities in the PBL response to DIs at different locations. The different stations are marked in Figure 4.7, which shows the DI frequency over western Europe in the winter months and was already discussed in section 4.2. This Figure also differentiated the two different groups of radiosonde stations, coloring the stations based on Meteo-France data blue and the stations based on ECMWF data white. However, the displayed frequency values are calculated with 3-hourly DI data, whereas the interval between available radiosonde ascents is 12 hours. The total number of identified categories based on the radiosonde ascents is provided in table 4.2, divided in the ascents at 00 UTC (upper table) and 12 UTC (lower table).

Prominent differences between the radiosonde stations with data from Meteo-France and ECMWF emerge, as the ECMWF data starts only at 1 December 2019, whereas the Meteo-France data is available from 1 December 2016. However, both datasets end on 31 December 2022 due to missing DI data after that point. Therefore, the ECMWF data is 3 years shorter and shows consequently lower numbers of identified categories in general. Unfortunately, a few radiosonde observations are missing in the Meteo-France dataset, with most files missing from Trappes (38 in total) and fewest from Nimes-Courbessac (11). The ECMWF dataset on the other hand is complete.

In the Meteo-France dataset, Nimes-Courbessac features the highest number of DI-related categories, while the lowest number is observed at Trappes. This matches the average frequency distribution displayed in Figure 4.7 (f). Interestingly, the DI number in relation to Pre- or Post-DI is highest at Nimes-Courbessac in the Meteo-France dataset, closely followed by Ajaccio, with more than double the amount of Pre- or Post-DI in total, hinting at more persistent DI events that last longer than 12 hours. Such events could possibly be supported by local flow phenomena. Nimes-Courbessac additionally exhibits a high number of radiosonde observations that are classified as both Pre- and Post-DI (15 in total) and are included in both categories. Without these cases, the DI number in relation to Pre- or Post-DIs would be higher relatively at Nimes-Courbessac than at Ajaccio, since Ajaccio only features 11 of these cases in total.

Among the seven ECMWF stations the highest number of DI-related categories is observed at Cuneo-Levaldigi and the lowest number at Santander. This is perfectly in line with the frequency

Table 4.2: Number of identified categories, namely Pre-DI, DI, Post-DI, Non-DI, Pre- and Post-DI (PaP) and missing files at 00 UTC (upper part) and 12 UTC (lower part) for all stations. Categories of the missing files are not determined. The time period in which the categories are identified starts on 1 December and ends on 31 December in the listed starting and end year for all stations, comprising all winter months in between.

Station	Time (00 UTC)	Pre	DI	Post	Non	PaP	Missing
Brest-Guipavas	2016–2022	34	65	32	431	5	15
Trappes	2016–2022	24	61	30	440	4	21
Bordeaux-Merignac	2016–2022	40	75	37	412	5	14
Nimes-Courbessac	2016–2022	48	96	47	383	11	5
Ajaccio	2016–2022	40	82	44	401	5	9
Camborne	2019–2022	21	27	26	231	5	0
Valentia Observatory	2019–2022	21	29	21	234	5	0
La Coruna	2019–2022	18	30	16	239	2	0
Santander	2019–2022	14	22	17	252	3	0
Barcelona Servei	2019–2022	11	29	18	245	2	0
Cuneo-Levaldigi	2019–2022	27	60	23	195	7	0
Decimomannu	2019–2022	15	39	20	229	2	0
Station	Time (12 UTC)	Pre	DI	Post	Non	PaP	Missing
Brest-Guipavas	2016–2022	46	55	44	422	4	9
Trappes	2016–2022	39	53	33	431	3	17
Bordeaux-Merignac	2016–2022	49	66	53	410	12	5
Nimes-Courbessac	2016–2022	43	101	43	382	4	6
Ajaccio	2016–2022	41	85	37	405	6	6
Camborne	2019–2022	20	33	15	235	2	0
Valentia Observatory	2019–2022	17	33	17	237	3	0
La Coruna	2019–2022	18	28	20	237	2	0
Santander	2019–2022	18	21	15	248	1	0
Barcelona Servei	2019–2022	22	27	13	239	0	0
Cuneo-Levaldigi	2019–2022	20	62	25	194	1	0
Decimomannu	2019–2022	24	35	19	226	4	0

distribution in Figure 4.7 (f), although those results are based on the average 3-hourly values in the winter period from 1979–2022, while the category numbers are identified 12-hourly in the period from 1 December 2019 to 31 December 2022. The total DI number at Cuneo-Levaldigi is almost triple that of Pre- or Post-DIs, indicating prolonged periods of DIs that are probably favored by the topography around the station.

The amount of DIs at 00 and 12 UTC show that the largest difference occurs at Brest with 10 DIs more identified at 00 UTC than at 12 UTC. While some stations like Trappes and Bordeaux-Merignac also show 8 and 9 DIs more at 00 UTC respectively, other stations like Nimes-Courbessac and Camborne exhibit 5 and 6 more DIs at 12 UTC, respectively. The difference at the remaining stations is smaller than 5. Thus, the number of categories appears to be distributed randomly at 00 and 12 UTC, but further research is required to know for certain. Larger diurnal variations are visible in Pre- and Post-DI category numbers. The largest difference in Pre-DIs occurs at Trappes with 15 Pre-DIs more at 12 UTC and the largest difference in Post-DIs at Bordeaux-Merignac with 16 Post-DIs more at 12 UTC. Although it is possible that individual flow conditions due to the topographic environment around a certain station favor the occurrence of DIs at a particular daytime, most of these differences are probably caused by chance. However, additional research is needed to confirm this assumption.

Vertical profiles for all stations based on radiosonde data are interpolated to 10 m vertically spaced levels and divided in 00 and 12 UTC data. The profiles and additional windroses are plotted similar as in section 4.3 for Brest. In order to save space, only the plots for the station Decimomannu, located 30 m above sea level on Sardinia, are presented and analyzed in detail. Major differences together with unique features at other stations are described afterwards. Decimomannu is selected because it is the station with the largest distance to Brest, whose DI events were already discussed in detail in the previous sections. Due to its southern location, it probably exhibits also subtropical characteristics. At 12 UTC, the average temperature profile in Decimomannu (Figure 4.20, a) shows a clear cold anomaly during DIs between 1 and 3 km, whereas all categories have similar values near the surface. Multiple small temperature inversions are observed in the DI, Pre- and Post-DI profile, starting from 800 m during the Post-DI and ranging to shortly above 3 km in the DI profile. Although the Non-DI median line also displays multiple inversions in that region, they are barely visible due to their minimal size.

The potential temperature (Figure 4.20, b) shows a sudden increase in the DI profile at about 1.5 km, in the Post-DI shortly above and in the Pre-DI shortly below 1 km, which could mark the median PBL height. Below that height, these profiles exhibit only a weak gradient, suggesting a well-mixed layer. The Non-DI profile on the other hand displays an almost steady increase in potential temperature. Potential instability is revealed in all categories, as the equivalent potential temperature (Figure 4.20, c) decreases from the surface and reaches a minimum between 1 and 1.5 km height. The largest decrease and thereby highest potential instability is observed during DIs. Interestingly, small potential instability is also evident during normal conditions in Non-DI profiles. This characteristic may be caused due to the influence of the Mediterranean with high moisture and relatively high temperatures at the surface.

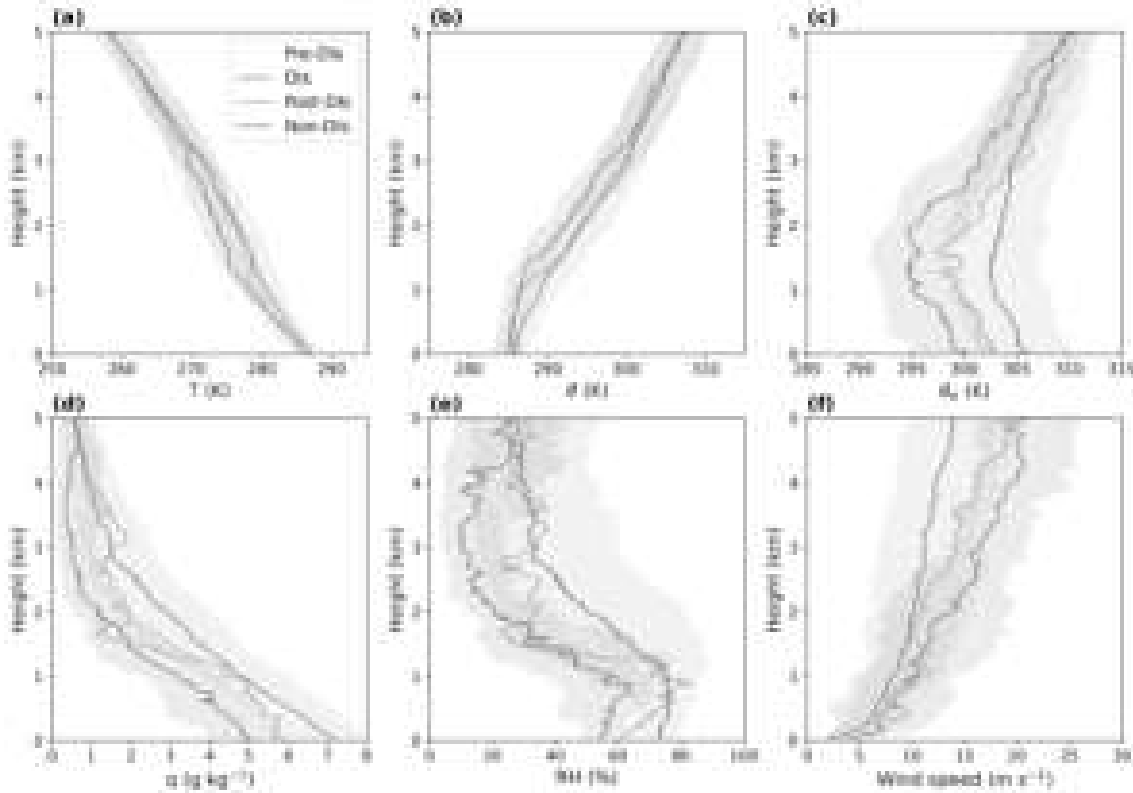


Figure 4.20: Average vertical profiles for Decimomannu at 12 UTC of (a) air temperature (K), (b) potential temperature (K), (c) equivalent potential temperature (K), (d) specific humidity (g kg^{-1}), (e) relative humidity (%) and (f) wind speed (m s^{-1}). Solid lines are the median value at each height and category and the shaded area marks the interquartile range of DIs and Non-DIs.

Indeed, the moisture values near the surface are very high during Non-DIs, reaching specific humidity values above 7 g kg^{-1} at the surface (Figure 4.20, d). The DI profile is about 2 g kg^{-1} drier at the surface and remains the driest profile throughout almost the entire considered 5 km. Pre- and Post-DI both show about 6 g kg^{-1} at the surface, but the decrease in specific humidity with height is stronger during Post-DIs, leading to briefly drier values than during DIs at about 1.7 km, before the Post-DI specific humidity increases sparsely. Nonetheless, during the first 1 km from the surface, the relative humidity values in all classes (Figure 4.20, e) increase and start to decline above 1 km, following approximately the same ranking as in specific humidity. Similar to the profiles in Brest, DI-related classes display larger wind speeds than Non-DIs (Figure 4.20, f) and DIs become the class with the highest wind speeds near 5 km, but with almost 10 m s^{-1} slower winds than at Brest. Below a height of 2 km, the largest wind speeds are measured during Pre-DIs.

A comparison with the data at 00 UTC shows a nightly surface inversion in all temperature profiles (Figure 4.21, a) that was not observed in the profiles at 12 UTC. The cold anomaly during DIs between 1 and 3 km is maintained and, in contrast to the profiles at 12 UTC, also visible in the Pre- and Post-DI classes. In the atmosphere above the surface, the profiles show even smaller inversions than at 12 UTC. The strongest one is observed during Post-DIs at approximately 1.6 km, which is located at a different altitude than the small inversions at 12 UTC were. Both Pre- and Non-DIs exhibit a relatively steady increase in potential temperature (Figure 4.21, b), especially from the surface up to 1.5 km. During DIs this increase is smallest, which would normally indicate

a well-mixed PBL layer. However, since this layer does not extend to the surface, this feature could also be retained from the PBL on the previous day and therefore indicate that turbulent mixing is nearly absent (Lee, 2018). After the strong and sudden increase in θ_e above the surface, which is opposed to the profiles at 12 UTC, all categories experience a decline to a minimum located between 1 and 2 km height (Figure 4.21, c). Similar to the profiles at 12 UTC, the smallest minimum is observed under DIs.

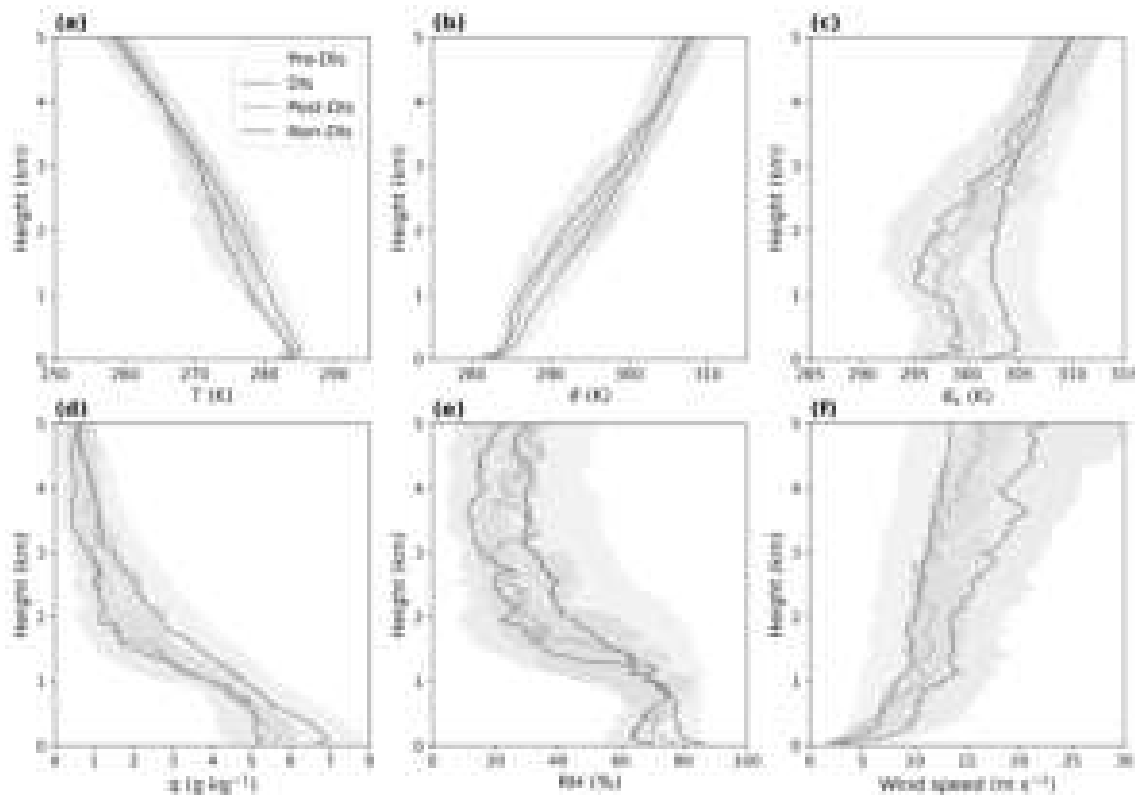


Figure 4.21: Average vertical profiles for Decimomannu at 00 UTC of (a) air temperature (K), (b) potential temperature (K), (c) equivalent potential temperature (K), (d) specific humidity (g kg^{-1}), (e) relative humidity (%) and (f) wind speed (m s^{-1}). Solid lines are the median value at each height and category and the shaded area marks the interquartile range of DIs and Non-DIs.

Due to the surface inversion a slight increase in specific humidity is visible above the surface, followed by a strong decrease (Figure 4.21, d). The distribution of the categories is basically the same as in the 12 UTC data, with Non-DIs as the wettest class followed by Pre-DIs. The driest class overall are DIs, closely followed by Post-DIs. In contrast to the specific humidity, the relative humidity profiles exhibit a decrease right above the surface because of the temperature inversion (Figure 4.21, e). Interestingly, the wind speeds at the station surface are all rather small and the largest ones occur during Pre-DIs and DIs with up to 3 m s^{-1} (Figure 4.21, f). These slow wind speeds support the formation of an inversion layer at the surface in all categories. Directly above the surface the wind speeds increase strongest during DIs and Pre-DIs, while Post-DIs feature smaller values closer to Non-DIs. After a wind speed maximum of about 20 m s^{-1} at 2 km, the wind speeds decrease during Pre-DIs and DIs become the class with the largest wind speeds above 2.5 km for the remaining profile.

In order to avoid the influences of the surface inversion layer and local flow features due to topography, the wind direction and speed at both 00 and 12 UTC is illustrated in detail at 500 m height (Figure 4.22). During Non-DIs (d) the dominant wind direction is northwest, but also west and southeast wind directions are observed. A slightly more western focused wind direction is measured under Pre-DIs (Figure 4.22, a). In contrast, DIs (Figure 4.22, b) feature a larger north-northwest component that also contains the largest wind speeds of all categories with more than 24 m s^{-1} . During Post-DIs (Figure 4.22, c) the wind direction is centered around northwest, analogous to Non-DIs, though Post-DIs lack due west wind directions. Therefore, these measurements indicate a slight wind jump during some DI events from west (Pre-DIs) to north-northwest (DIs) before the PBL recovers and normal northwest wind directions dominate during Post-DIs. This wind jump was more obvious at Brest, since the normal main wind direction during Non-DIs was different from DIs, whereas it is superimposed on the wind direction patterns at Decimomannu.

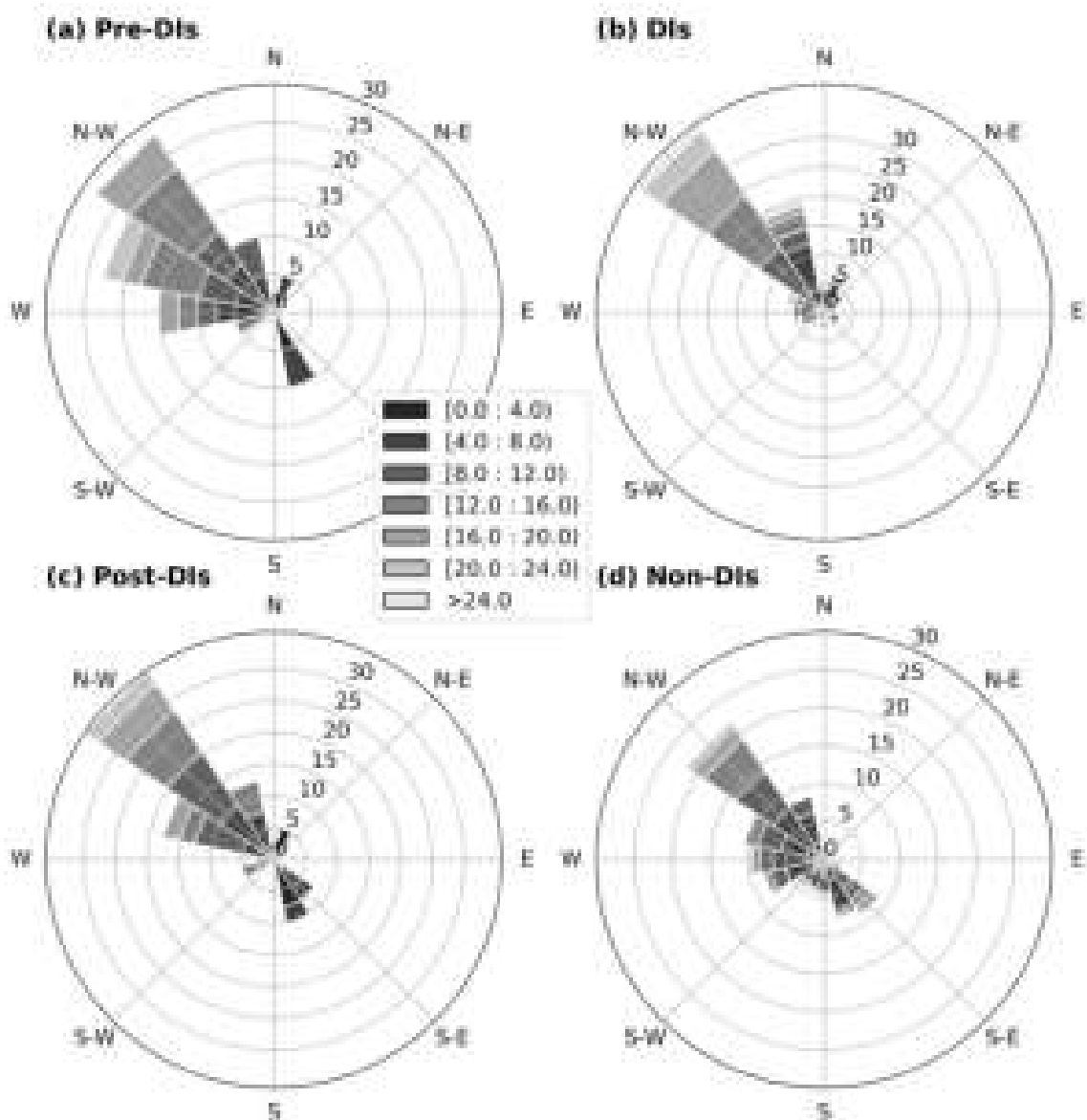


Figure 4.22: Wind roses for Decimomannu in 500 m height with 00 and 12 UTC data, separated into the different categories (a) Pre-DIs, (b) DIs, (c) Post-DIs, (d) Non-DIs and colored according to the wind speed in m s^{-1} . The length of the bars indicates the wind direction frequency in %.

However, the datasets at Brest and Decimomannu may differ slightly due to the different data origin from Meteo-France and ECMWF, respectively. But a comparison at Brest, for which both datasets are available, revealed that only isolated, small changes occur in the windroses (not shown), indicating that these differences are almost negligible. Such subtle changes in individual radiosonde ascents are likely the result of converting the pressure levels of the ECMWF dataset in altitude in m. The effects of this y-axis conversion for the vertical profiles are described in section 3.2.2.

During the description of vertical profiles at a station, the different categories are often sorted, for example by specific humidity or wind speed values at the surface. Overall, the exact rankings of the classes for different variables vary from station to station. However, a list of important, recurring features and similarities is provided below:

- Cold anomaly during DIs compared to Non-DIs, most pronounced between 1 and 3 km (visible at 11 of 12 stations). While Pre- and Post-DI often feature a cold anomaly at that height as well, it is typically smaller than during DIs and occasionally Pre- and Post-DIs are even warmer than observed Non-DI temperatures.
- Diurnal temperature variations near the surface. A pronounced nightly temperature inversion at the surface in at least one class occurs at the majority of stations (visible at 7 of 12 stations). In the potential temperature profiles, all stations show at least a slight increase directly above the surface at 00 UTC, whereas a slight decrease above the surface is often observed at 12 UTC (visible at 8 of 12 stations).
- Weakest gradient in potential temperature during DIs below 1.5 km with differing vertical extent, indicating a better-mixed layer than during the other categories (visible at 10 of 12 stations). This feature is superimposed by the diurnal cycle of the PBL, as it is usually much clearer at noon.
- Lowest minimum in equivalent potential temperature during DIs between 1 and 2 km, suggesting potential instability at noon (visible at 11 of 12 stations). At 00 UTC the potential instability is often capped by a surface inversion.
- Lowest specific humidity values at the surface during DIs (visible at 9 of 12 stations) that are often closely matched by Post-DIs. Highest values during Pre-DIs or Non-DIs (each visible at 6 of 12 stations). This ranking is generally valid to a height of 2.5 – 3 km.
- Larger wind speeds during DI-related classes at all stations in general. Largest wind speeds at the surface occur mostly during Pre-DIs (visible at 8 of 12 stations), while the highest wind speeds at 5 km occur usually under DIs (visible at 7 of 12 stations).
- Wind direction shift from approximately west during Pre-DIs to northwest under DIs and back to west to southwest during Post-DIs (visible at 9 of 12 stations).

These bullet points summarize the most important similarities at all stations. If one of the mentioned features occurs at 00 UTC, but not at 12 UTC or vice versa at a certain station, then this station

is counted as 0.5 in the number of stations that show this feature. Individual peculiarities at each station are described in the following text.

Naturally, average temperature values near the surface are warmer at the southern stations and Decimomannu is therefore one of the warmest stations, only minimally surpassed by Ajaccio, located due north of Decimomannu on Corsica. The station Ajaccio is located 5 m above sea level on an airport that borders directly upon the Mediterranean to its southwestern side. Interestingly, the temperatures at the surface level at Ajaccio are about 1–2 K higher than at 20–40 m above in all categories at 12 UTC, indicating a superadiabatic lapse rate. In contrast, the data at 00 UTC features the most pronounced surface temperature inversion in all categories of any station. Directly towards the surface at 12 UTC, a strong specific humidity increase is observed in all categories, compared to levels only 20–40 m above. In contrast, the specific humidity values remain relatively constant from the surface up to 0.5 km at 00 UTC. Surprisingly, the wind speed exhibits median values lower than 5 m s^{-1} in the first 1 km in all categories. Such low wind speed values favor the formation of the found nightly surface inversion.

Wind roses directly at the station surface reveal a dominating southwesterly wind direction during the day (12 UTC) and an opposing northeasterly wind direction during the night (00 UTC) during all categories. Based on the station's location, the measured wind directions indicate a well established circulation: a sea breeze at 12 UTC and a land breeze at 00 UTC, although the wind speeds stay mainly below 5 m s^{-1} at both times. The sea breeze at 12 UTC may explain the enhanced temperature and specific humidity values directly at the surface during that time.

However, at 500 m the strong signature of this land-sea breeze circulation disappears in the windroses. Southwesterly wind directions dominate instead during normal conditions, while DI-related categories feature more northwest centered wind directions in total, subtly indicating the typical wind direction change during the DI passage.

The station following next according to temperature values at the surface, at least during Non-DIs, is Barcelona-Servei, situated in northwestern Spain at the Mediterranean coast. During Post-DIs, a clear temperature inversion is found at about 1.2 km both at 00 and 12 UTC, though it is preceded by a smaller temperature inversion approximately 200 m lower. DIs and Pre-DIs display less clear, multiple inversions at different altitudes. All DI-related situations reveal obvious increases in potential temperature already at 800 m, possibly marking the PBL height at one of the lowest altitudes among all stations. Specific humidity profiles showcase the lowest values in the DI and Post-DI profiles at 12 UTC, but unexpectedly the Pre-DI class exhibits the driest values near the surface at 00 UTC. In addition, the highest nightly wind speeds at the surface occur during DIs and the highest wind speeds at 5 km during Pre-DIs, switching the typical ranking which is observed at the majority of stations and also during noon at this station. Another interesting aspect of the profiles at 00 UTC is the lack of visible temperature inversions at the surface, despite the wind speeds at the surface being as low as $2\text{--}4 \text{ m s}^{-1}$. Nevertheless, an increase in potential temperature at the surface is observed during DIs and a slight increase also during Post-DIs and Non-DIs, suggesting stable conditions. Although the nightly inversion at the surface might not be directly visible in the temperature, such an increase in potential temperature is a sign of a surface inversion layer (Lee, 2018).

The nearest other station to Barcelona-Servei is Nimes-Courbessac, which is located in Southern France near the Mediterranean coast. In the temperature profiles all classes exhibit a strong temperature inversion at the surface at 00 UTC. After an immediate short decrease in 12 UTC data, the potential temperature increases in all categories, but slowest during DIs below 1 km. At about 1 km, a sudden small increase is observed in the DI-related classes, hinting at the PBL height, whereas the Non-DI continues its gradual increase in potential temperature. In contrast, due to the nightly surface inversion, an almost monotonous increase in potential temperature is measured during all categories at night.

Thanks to enhanced temperature and especially moisture near the surface at 12 UTC, similar as in Ajaccio, a shallow layer of potential instability reaching up to approximately 300 m is visible in the θ_e profiles of Pre-DIs, Post-DIs and Non-DIs. During DIs this layer reaches up to 1.5 km, as this is the only category that experiences a minimum in θ_e shortly above 1 km. Interestingly, an opposed pattern is visible at 00 UTC, as DIs feature the most steady increase in θ_e of all classes.

The wind speed profiles reveal DIs as the category with the highest wind speeds in the lowest 2 km (00 and 12 UTC). This is unusual behaviour, since the highest wind speeds during a DI passage are observed under Pre-DIs at most stations. The nightly surface inversion during Pre-DIs and the steady increase of θ_e during DIs are additional irregularities. While the typical wind direction shift during the DI passage from west (Pre-DI) to northwest (DI) and back to southwest or southeast (Post-DI) is seen in windroses at about 500 m height in a few radiosonde ascents, the vast majority of radiosonde ascents show a wind direction from due north in all categories. This dominant wind direction is probably caused by the mistral wind, which is a northerly low-level jet that blows through the Rhône valley and down to the Gulf of Lion, transporting relatively cold and dry continental air masses (Givon et al., 2021). The superposition of DIs with the mistral wind may explain the differences to typical DI characteristics at Nimes-Courbessac. Perhaps the mistral wind is sometimes even misidentified as DI or could increase the persistence of existing DI events, leading to the maximum in DI frequency observed east of Nimes-Courbessac over the Rhône valley.

Cuneo-Levaldigi, east of Nimes-Courbessac, is located inside the Alpine arch and thus surrounded by mountains except to the east. With a height of about 385 m above sea level, Cuneo-Levaldigi possesses by far the highest elevation of all stations. Contrary to all other stations, all DI-related categories display higher temperature values than Non-DIs below 2 km and the highest temperatures are observed during DIs. Unexpectedly, a nightly temperature inversion is found during Pre-DIs, whereas DIs only exhibit a smaller inversion and Post- or Non-DIs display no visible temperature inversion at the surface. Non-DIs display an increase in potential temperature with height at 12 UTC, starting at the station surface height (385 m), whereas this increase begins for the DI-related situations first at about 700 m, indicating a shallow well mixed layer with a height of only 300 m above the station surface. Due to a fast reduction of specific humidity above the surface during DIs at 12 UTC, the θ_e profile of DIs uniquely exhibits a small decrease above the surface, indicating a layer of weak potential instability reaching up to 900 m. At 00 UTC, a more continuous increase in all classes is observed, superimposed by small fluctuations. The profile distribution in specific humidity and relative humidity is in line with other stations, with DIs as the driest, followed by Post-DI, Pre-DI and Non-DI as the moistest profile (both at 00 and 12 UTC). Interestingly, the relative humidity profiles decrease from the surface, whereas an increase below 1 km was observed

at the previous stations. An abnormal behaviour is visible in the wind speed profiles in all categories, as all values remain lower than 5 m s^{-1} below 2 km (both at 00 and 12 UTC), probably caused by the high mountains of the Alpine arch surrounding Cuneo-Levaldigi.

Overall, the radiosonde observations suggest a strong topographic influence and the unique warm anomaly during DIs at the surface could be the result of weak Alpine foehn winds, as those winds are typically marked by a temperature rise and a decrease of humidity (Drechsel and Mayr, 2008). Due to the local modification of DI events, typical characteristics like a deep, well-mixed layer during DIs are missing. Since Figure 4.7 (f) shows a local maximum in DI frequency near Cuneo-Levaldigi, surrounded by the Alpine arch, some of the Alpine foehn winds might be mistaken as DIs, causing a higher frequency than in the surrounding area. However, further research is required to understand the relationship between DIs and Alpine foehn winds.

The station with the second highest elevation of 168 m is Trappes, southwest of Paris. Based on average surface temperatures, Trappes is the coldest station, in particular at 00 UTC. The reason for this is probably the more continental location, as Trappes is farther away from mild ocean waters than any other station, while also being positioned relatively far north. This is the only station that features the strongest nightly temperature inversion at the surface during DIs, while Pre-DIs and Non-DIs show no visible temperature inversion at the surface. Sudden potential temperature increases at noon are observed at approximately 1.2 km during DIs, 1 km at Post-DIs and 900 m at Pre-DIs, while Non-DIs exhibit an almost constant increase. However, below those heights the θ profile also increases during the DI-related categories, with the lowest increase during DIs. At night the potential temperature increases more steadily during all categories, but slowest during DIs for the first 1.2 km, indicating that the typical DI characteristic of a well-mixed PBL is superimposed by the diurnal variations of the PBL. The remaining considered variables depict basically the typical behaviour of DIs, described in the above list of typical features.

Bordeaux-Merignac is located in southwestern France, close to the Atlantic coast. An outstanding feature in the temperature profiles at 00 UTC is the occurrence of a sharp inversion with a sudden temperature increase of slightly more than 2 K during Post-DIs at a height of about 1.5 km. This is similar to the temperature inversion during Post-DIs found by Ilotoviz et al. (2021) at a station in the Azores. However, DIs and Pre-DIs present much smaller temperature inversions above the surface and at noon this temperature inversion during Post-DIs virtually disappeared. In addition, this is the strongest and sharpest temperature inversion above the surface of all stations among all categories. The DI passages at the considered stations therefore do not indicate a sharp temperature inversion at the top of the PBL as a typical feature. One possible explanation of this difference to Ilotoviz et al. (2021) is the usage of a different dataset for the identification of DI trajectories, since Ilotoviz et al. (2021) used ERA-Interim and this thesis employed ERA5 data as input wind field to LAGRANTO. Further, the DI characteristics may differ due to different dynamical influences in the Azores and western Europe, as elucidated at the end of subsection 4.4.2. Lastly, the longer observation period and thus higher number of considered DIs in this thesis may contribute to a dilution of the inversion structure in the median, for example if they occur at different altitudes for different DI events.

Another noteworthy difference at Bordeaux-Merignac is that the layer of weak potential temperature

gradient in the Post-DI profile during 00 UTC appears to be larger than during DIs above the surface inversion, but the opposing pattern is observed in the 12 UTC profiles. This illustrates the variability among different DI-related classes that can occur at each station, although the expected behaviour with a larger, better mixed-layer during DIs is still visible at 12 UTC.

The remaining four stations are all located directly at the coast of the North Atlantic ocean. La Coruna sits at Spain's northwestern Atlantic coast. Near the surface, the DI median line of specific humidity is just slightly below Non-DIs at 12 UTC, while Pre-DI and Post-DI are the wettest and driest class, respectively. A faster decrease in DIs widens the difference to Non-DIs above 1.5 km. Surprisingly, DIs feature slightly higher RH values in the lowest 1.5 km than Non-DIs during 12 UTC. This high humidity might be explained by the fact that winds during DIs advect moist air from the ocean, which is mixed with the DI air near the surface. This assumption is supported by the wind direction observations near the surface, as the dominant wind direction during normal conditions (Non-DIs) is southwest, transporting inland air to the station. In contrast, DIs exhibit more westerly and easterly wind directions that advect coastal air to the station. However, at 00 UTC the usual category ranking in specific humidity returns, but the differences between the categories are small.

The most peculiar characteristic at this station are the wind directions during DIs at 500 m height, as DIs show directly opposing west and east directions with an almost equal proportion. Instead, the other classes display mainly west (Pre-DI) or southwest wind directions (Post-DI and Non-DI). The large amount of eastward wind directions during DIs is unique at this station and the exact causes are unclear.

Due east of La Coruna is the station Santander, which actually shows considerable inversions in the DI-related temperature profiles. However, the location of those inversions does not always coincide with the results at other stations, as the largest inversion during Post-DIs at 12 UTC is located already at about 200–300 m. This underlines the variability that occurs among the different classes at the various stations.

An odd behaviour is evident in the lowest 1 km of specific humidity profiles at 00 UTC. The lowest specific humidity values are observed during Pre-DIs and the highest during DIs. Typically this ranking is reversed, which is also the case in the profiles at 12 UTC at the same station. The wind directions directly at the surface provide an explanation for this exception at 00 UTC. During Pre-DIs the dominant wind direction is southwest, indicating a transport of dry inland air to the station. But since this is also the case for Post- and Non-DIs, it is not entirely clear why Pre-DIs are the driest category at 00 UTC. In contrast, DIs feature mostly west to west-northwest wind directions that flow parallel to the coastline, advecting moister air from the North Atlantic. At 12 UTC the Pre-DI wind at the surface turns to westward centered wind directions while the DI wind directions are almost evenly distributed. In spite of these irregularities at the surface, the wind directions at 500 m present a more familiar behaviour. Both at 00 and 12 UTC a dominating western wind direction is observed under Pre-DIs, followed by mainly a west-northwest wind direction during DIs. Post-DIs return to a dominant wind from west to southwest, which matches the normal conditions (Non-DIs) at Santander.

Camborne is located at the southwestern tip of England and Valentia-Observatory sits on the southwestern coast of Ireland. Both stations are highly influenced by the North Atlantic due to their exposed location near the coast, which results in the highest median wind speeds of all stations at Valentia-Observatory and the second highest at Camborne at the surface. A pristine influence of DIs on the PBL is observed at both stations, fulfilling almost all typical characteristics in the list of similarities at all stations. Diurnal variations in the PBL at those stations are minimal, which may be caused by the influence and close proximity of the North Atlantic, since virtually no diurnal variations occur in a maritime PBL over the ocean (Medeiros et al., 2005; von Engeln and Teixeira, 2013). The influence of the North Atlantic might contribute to the large wind speeds that are also observed at night, preventing the formation of a temperature inversion at the surface. However, a slight increase in potential temperature directly above the surface is visible at both stations, which is a sign of a (very weak) inversion layer (Lee, 2018). Above this very weak surface inversion layer the vertical gradient of potential temperature is almost constant up to 800–900 m during DIs, closely followed by Post-DIs, indicating a well-mixed layer. At Camborne the gradient in this layer during DIs and Post-DIs is even smaller at 00 UTC than at 12 UTC, suggesting that this feature at 00 UTC is real and not retained from the PBL on the previous day. Since the observed behavior is based on median values, this assumption needs to be confirmed by analyzing individual DI events in more detail. Therefore, additional research and measurements are required to clarify the influence of DIs on the PBL during the night.

This section elucidated the various differences and common features among the different stations. Most notable differences are caused by local topography, which modifies the local wind flow and may lead to varying DI characteristics, for example a positive temperature anomaly during DIs at Cuneo-Levaldigi or a lacking wind shift during the DI passage at Nimes-Courbessac. The following section investigates the ability of global ECMWF model data to accurately predict the vertical profiles and thus the typical DI features within them.

4.6 Evaluation of numerical weather prediction model data

In addition to the observation, the ECMWF radiosonde dataset also offers a background and an analysis value. This section analyzes the difference of those two values to the observation, with the goal to identify systematic model biases. For this purpose data at Brest is utilized, since this station was already analyzed in detail in previous sections. However, the ECMWF data only starts in December 2019, implying that the total number given in table 4.1 is notably reduced. Although the yearly number of categories at Brest is also listed in this table, it cannot provide the exact amount of categories in the ECMWF data, since this data starts in December 2019 and the category numbers for 2019 also contain data from January and February. Therefore, the category number for Brest during December 2019 is additionally calculated and yields 6 Pre-DIs, 9 DIs, 6 Post-DIs, 42 Non-DIs in total and no missing files. One Pre-DI is simultaneously classified as Post-DI. Based on this, the total number of categories in the period from 1 December 2019 to 31 December 2022 is

Table 4.3: Number of identified categories at 00 UTC (upper part) and 12 UTC (lower part) for Brest in the period starting at 1 December 2016 and 1 December 2019 to 31 December 2022. The number of categories of missing data files is written in parentheses behind the number of available files.

Time (00 UTC)	Pre-DI	DI	Post-DI	Non-DI	Pre-and Post-DI	Missing
2016–2022	34 (1)	65 (4)	32 (1)	431 (9)	5	15
2019–2022	17	38 (1)	22 (1)	222 (4)	3	6
Time (12 UTC)	Pre-DI	DI	Post-DI	Non-DI	Pre-and Post-DI	Missing
2016–2022	46 (2)	55 (2)	44 (1)	422 (4)	4	9
2019–2022	28 (2)	32	24	216 (2)	2	4

calculated and compared with the larger period in the Meteo-France dataset, starting on 1 December 2016 in Table 4.3. Those results show that the number of categories is considerably reduced in the period of the ECMWF dataset to slightly more than half of the total amount in the Meteo-France data, both at 00 and 12 UTC.

The vertical profiles of innovation (O-B) and residual (O-A) during the different categories in the variables temperature, specific humidity and wind speed at 00 UTC at Brest are depicted in Figure 4.23. Negative values indicate larger values in the model data, whereas positive values imply lower than observed values in the model data. For the interpretation of the calculated differences, the average vertical profiles of the observations in section 4.3 are used.

During normal Non-DI conditions, the largest bias in both the background and analysis occurs at the surface, indicating an overestimation of temperature in the model data. The average temperature profiles reveal a surface temperature inversion during Non-DIs, DIs and Post-DIs (Figure 4.9 a), which probably causes this departure. The magnitude of the innovation is almost twice as high as the residual, suggesting a clear improvement in the analysis. After briefly reaching similar values to the observation, both in the background and the analysis as observed at 500 m, negative differences prevail for the rest of the considered 5 km. Around 2 km, the magnitude of the innovation is briefly smaller than the residual. However, the residual remains small during the rest of the profile with a value of approximately 0.1 K, while the innovation partially features values of up to -0.2 K.

Both DIs and Post-DIs also reveal a warm bias at the surface, with the largest values during Post-DIs. However, the magnitude of the innovation at the surface during DIs is smaller than during Non-DIs. This indicates that the temperature inversion at the surface is better represented in the model during DIs than during Post-DIs. At about 1.5 km during Post-DIs the background exhibits a cold bias, with the innovation reaching almost 0.6 K. The average profiles reveal a temperature inversion at that height during Post-DIs, which is probably not well represented in the background. In contrast, the analysis values are more similar to the observations and even show a small warm bias around 1.5 km.

During DIs the innovation and residual vary around the observations, showing a slight cold bias between 0.5 and 1 km and a slight warm bias around 2.5–3 km. But since the slight warm bias is also observed under normal conditions during Non-DIs, the lower cold bias might be more noteworthy. This could imply that the model overestimates the cold anomaly during DIs between

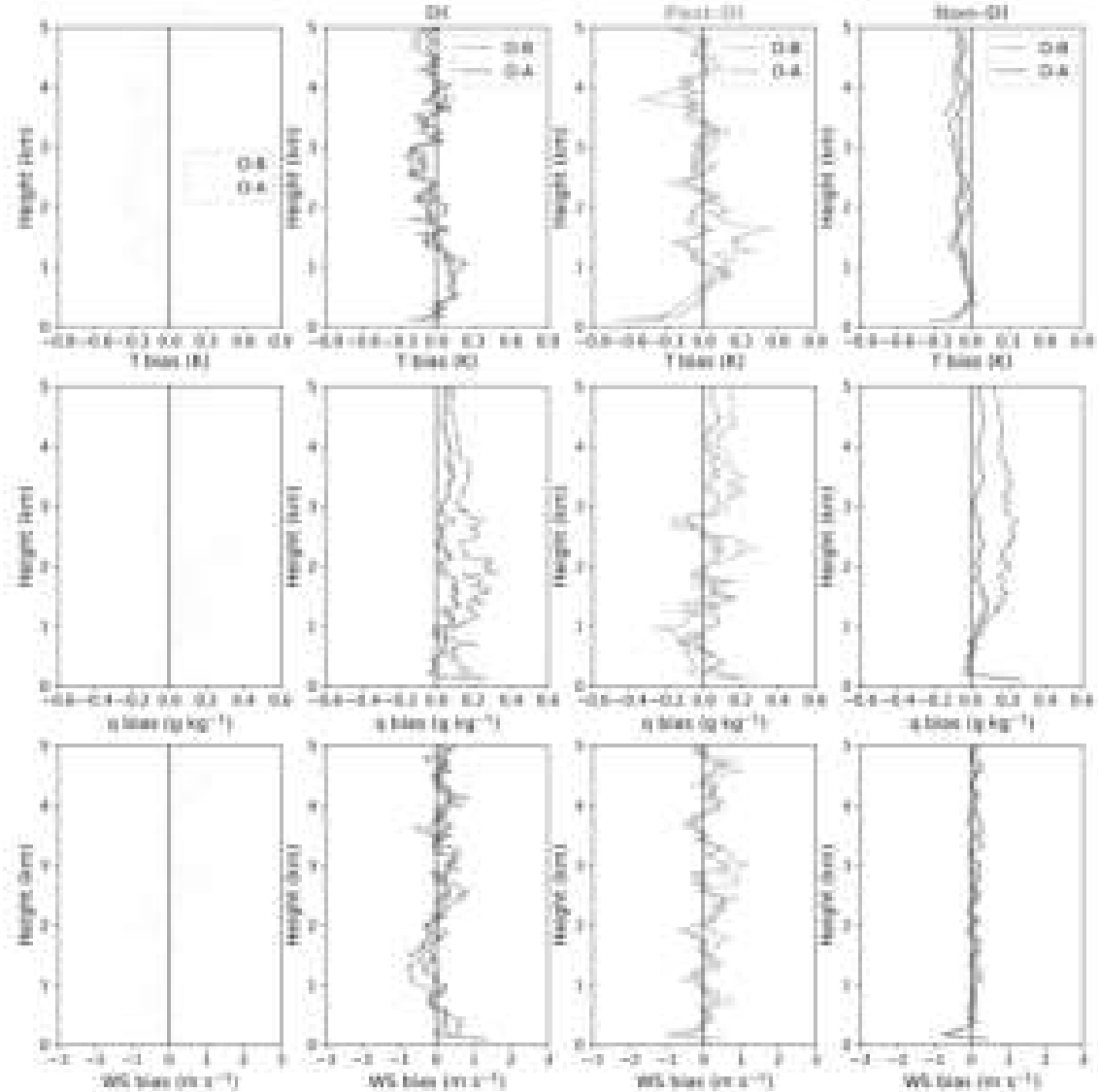


Figure 4.23: Median Temperature (K), specific humidity (g kg^{-1}) and wind speed (m s^{-1}) bias during Pre-DI, DI, Post-DI and Non-DI categories at 00 UTC at Brest. In each subplot, the difference between observation and background (O-B) is drawn with a dashed line and the difference between observation and analysis (O-A) is drawn with a solid line.

0.5 and 1 km. Pre-DIs are the only class without clear biases at the surface, probably owing to the lack of a temperature inversion at the surface. A similar cold bias as during DIs is visible in the background, but not in the analysis. Above 1.8 km a warm bias is displayed, as both innovation and residual exhibit mostly negative values up to 4 km, albeit with interruptions.

Overall, the largest differences are visible during Pre- and Post-DIs, but this might be caused by their lower number, compared to DIs and Non-DIs. The primary reason for this could be the averaging process. However, even the largest difference observed, which is about -0.7–0.8 K in the analysis at the surface during Post-DIs, is still relatively small, considering the coarse horizontal resolution of 9 km of the utilized global ECMWF model.

Normal conditions (Non-DIs) in the specific humidity profiles reveal positive innovation and residual values at the surface, indicating a dry bias. Between 0.5 and 1 km a brief section of

minimal innovation and residual values follows, before a dry bias above 1 km returns and remains throughout the considered troposphere. The dry bias above 1 km is much larger in the background. In general, the innovation and the residual show the same behaviour, but the residual is mostly smaller in all categories, as expected.

At the station surface, the observed dry bias is also evident during the DI-related categories, even with almost the same magnitude around 0.2 g kg^{-1} . Considering the average vertical profiles of specific humidity at 00 UTC at Brest, this dry bias is hardly surprising, as all categories show a sudden increase at the surface compared to the levels above (Figure 4.9 d). During Pre-DIs a short wet bias is found above the surface, reaching up to 500 m. Apart from this, Pre-DIs mainly show a dry bias in the remaining profile, with isolated peaks in the innovation reaching above 0.4 g kg^{-1} . DIs feature the most persistent dry bias in the background, while the analysis exhibits almost the same behaviour as during Non-DIs. This could imply an underestimated mixing of DI air with moist PBL air in the background. However, since Non-DIs also display a dry bias above 1 km, this difference may also be station inherent. The most wet biases occur during Post-DIs, though dry biases still outweigh. These differences may be caused by random fluctuations in the observed profile. Such small perturbations are visible in the Post-DI median in Figure 4.9 (d).

Wind speed appears to be represented best by model data, as both the background and the analysis exhibit only a slight slow wind bias during Non-DIs, after a short fluctuation near the surface. This impression is largely caused by the larger range of the x-axis, which was selected to accommodate most innovation and residual values of all ECMWF stations. Thus, wind speed biases at Brest are rather small compared to other stations, for example La Coruna that exhibits the largest magnitude of innovation and residual with almost -3 m s^{-1} at the surface (not shown). The fluctuation at the surface at Brest is basically visible in all categories, but strongest during Pre-DIs. At the station surface, observations show a higher wind speed than model data, while the observations immediately above are smaller than the model data.

Interestingly, the wind speed observations in Figure 4.9 (f) reveal a similar behaviour. During Pre- and Non-DIs, the wind speed minimum is located immediately above the surface. This is likely a station specific feature, due to local flow conditions created by the station environment. Besides that, the most notable difference to observations during Pre-DIs is a slow wind bias in the background above 4 km, with innovation values reaching $1\text{--}1.5 \text{ m s}^{-1}$. Slightly too high wind speeds are estimated by the model data during DIs between 1 to 1.6 km, mainly in the background, while above 2 km slightly too low model values prevail. During Post-DIs, the innovation displays predominantly positive values wind , whereas the residual varies more around the observations. Overall, the observed wind speeds are well captured by the model data, especially in the analysis, since the described biases are all relatively small.

This analysis revealed that the strongest biases are often found near the surface. As the surface conditions are strongly modified by diurnal PBL variations, different biases may occur near the surface at daytime (12 UTC). Indeed, an opposite temperature bias is detected at the surface in all categories with warmer observed temperatures than in the model data (Figure 4.24). Surprisingly, the residual is higher at the surface than the innovation, indicating a higher bias in the analysis.

However, above 1 km a slight warm bias emerges during Non-DIs, analogous to the profiles at 00 UTC.

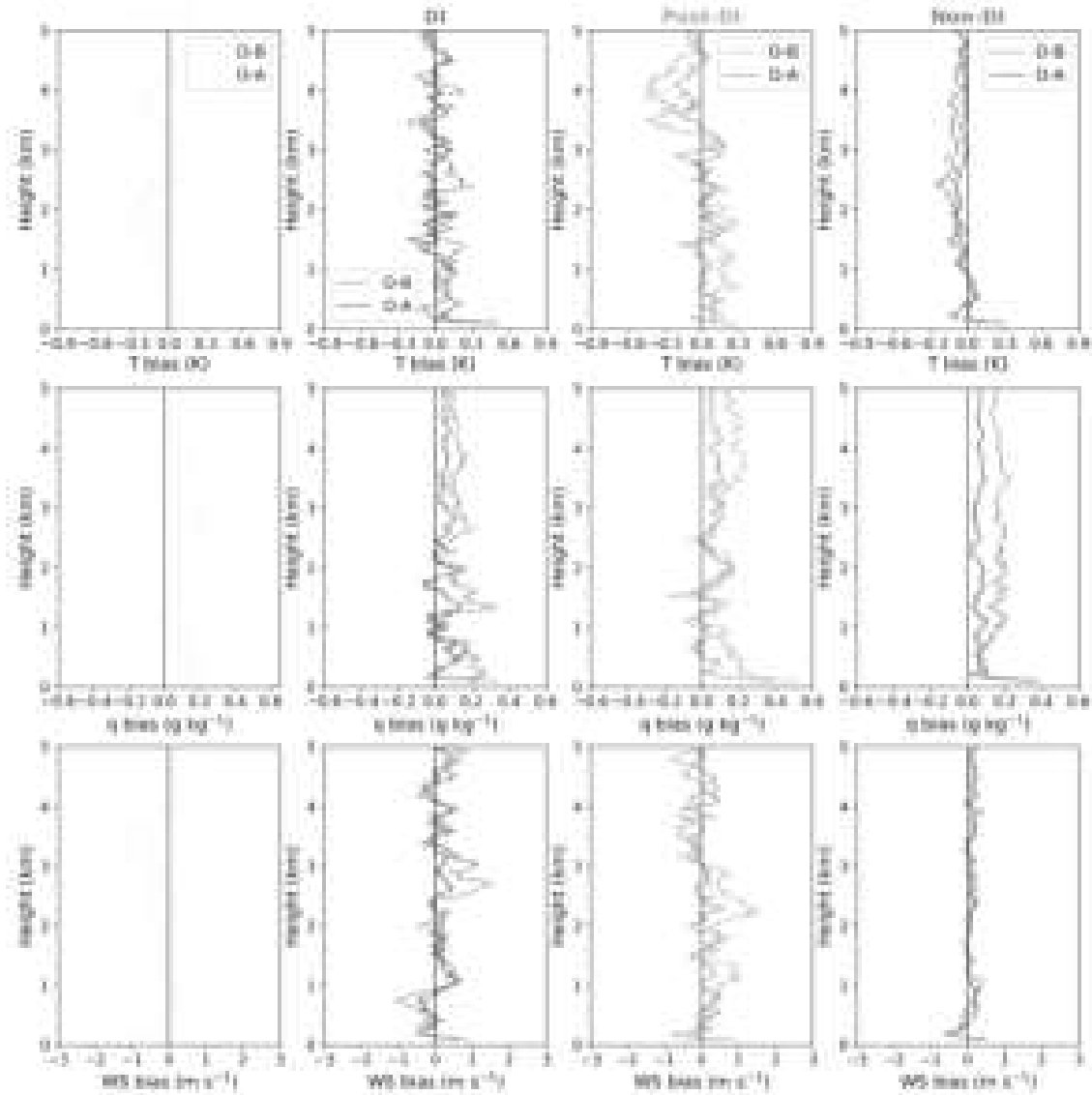


Figure 4.24: Median Temperature (K), specific humidity (g kg^{-1}) and wind speed (m s^{-1}) bias during Pre-DI, DI, Post-DI and Non-DI categories at 12 UTC at Brest. In each subplot, the difference between observation and background (O-B) is drawn with a dashed line and the difference between observation and analysis (O-A) is drawn with a solid line.

By far the largest cold bias at the surface occurs during DIs with a residual value of about 0.5 K, while the innovation value is slightly above 0.3 K. This remains the highest value in the DI profile. Above the surface, a small cold bias is indicated by the innovation for the most part of the profile, whereas the residual displays small variations around the observations. The same behaviour is generally evident in the first 3 km during Post-DIs, but above that the innovation switches to a warm bias. This is the largest bias in the Post-DI profile, reaching its maximum around 4 km with -0.4 K and also the residual exhibits a warm bias at that height, though with only about -0.2 K. The vertical profiles of the observations in Figure 4.10 (a) reveal the Post-DI as the coldest class at that height due to a strong decrease before, which is probably not captured well by the background and analysis. Nevertheless, this is not a typical feature during Post-DIs as vertical profiles at other

stations do not show this behavior. The innovation during Pre-DIs shows the only warm bias near the surface and this bias prevails to approximately 2.5 km. In contrast, the residual depicts a cold bias near the surface up to 1 km and then switches to mainly a small warm bias.

In the specific humidity profiles a dry bias dominates over the whole considered 5 km in all classes with the maximum at the station surface, which is larger than in the profiles at 00 UTC. This difference is explained by Figure 4.10 (d), since the sudden jump in specific humidity at the surface exceeds those observed at 00 UTC. As previously mentioned in the description of those profiles, this humidity increase could be caused by moisture advection from the ocean near the surface. Therefore, it would be a station specific feature and not a typical DI feature. During Non-DIs, only positive values are observed both in the innovation and residual, indicating a dry bias in the entire considered lower troposphere up to 5 km. The same pattern is generally evident in the DI-related categories, although they also display a few negative values, especially during DIs and Post-DIs below 3 km.

The Non-DI profile of wind speed looks almost identical to the profile at 00 UTC, depicting a fluctuation near the surface followed by only a minimal slow wind bias. Similar to the 00 UTC profiles, the DI-related categories display fluctuations near the surface that are also visible in the corresponding vertical profile of wind speed observations (Figure 4.10 f). In contrast to Non-DIs, biases are detected above the fluctuations near the surface, with the highest values in the innovation. Pre-DI profiles show predominantly a high wind bias between 1 and 4 km, albeit mostly in the background. Above 1 km negative values, indicating a slow wind bias, outweigh during DIs. Post-DIs feature a slow wind bias between 1 and 3 km, followed by a switch to a high wind bias in the innovation, while the residual displays only small oscillations around the observations. These biases in the DI-related classes appear non-systematic and random, since these patterns are not entirely consistent with the patterns at 00 UTC.

While some of the found bias patterns are consistent with the average vertical observations, this is mainly the case for station specific features. Overall, the magnitude of detected biases is relatively small, therefore it is possible that some of the biases are caused by random perturbations. This point is supported by the fact that the largest biases occur generally during Pre- and Post-DIs, which are the two categories with a lower number of cases. Normally, random perturbations become smaller when they are averaged over a higher number of cases.

Since the vertical profiles of Decimomannu were examined in detail in the previous section, this station is utilized to illustrate differences among the stations. To this end, Figure 4.25 shows the biases in temperature, specific humidity and wind speed at Decimomannu similarly as in the previous figures at Brest, but with both 00 and 12 UTC data combined in this Figure. The largest temperature bias during Non-DIs occurs at the surface, both in the innovation and residual. This bias is especially pronounced in the 00 UTC data, where the innovation and residual display a value of approximately -1 K, indicating a warm bias, whereas the 12 UTC data only reaches values short of -0.3 K (not shown). Approximately 200 m above this bias at the surface, both the innovation and residual become positive for the remaining profile, with the only exception being the innovation around 1.5 km. The warm surface bias is also observed during the DI-related categories

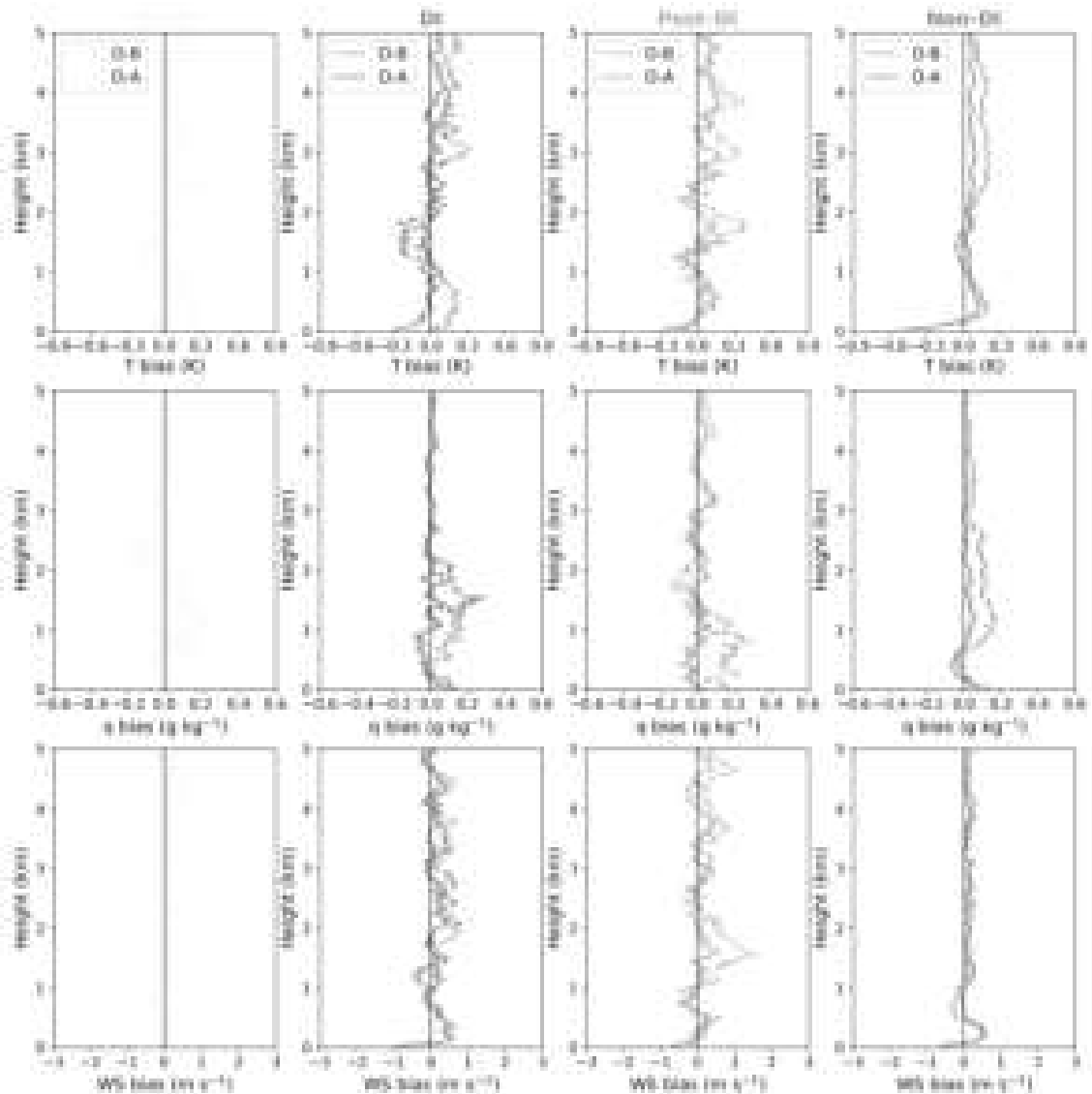


Figure 4.25: Median Temperature (K), specific humidity (g kg^{-1}) and wind speed (m s^{-1}) bias during Pre-DI, DI, Post-DI and Non-DI categories at 00 and 12 UTC at Decimomannu. In each subplot, the difference between observation and background (O-B) is drawn with a dashed line and the difference between observation and analysis (O-A) is drawn with a solid line.

with decreased strength, except for the innovation during DIs which shows small positive values. Innovation and residual exhibit generally the same bias behaviour as observed during Non-DIs, though with partially larger biases. This could be caused by the lower number of DI categories compared to Non-DIs, due to the averaging process.

Specific humidity profiles during Non-DIs reveal oscillating innovation and residual values near the surface, starting with positive values and followed by negative values centered around 400 m, before switching back to positive values for most of the remaining profile. A clear dry bias is visible between approximately 0.8 and 2.8 km, but mainly in the background. The DI profile exhibits a similar progression, albeit with a lower located dry bias in the background and an analysis that is even closer to the observations than during Non-DIs. During Pre- and Post-DIs the dry bias in the background is largest below 1.5 km. Although this dry bias during Pre- and Post-DIs at this altitude

is also observed at Brest, it is less strong and follows the course observed during Non-DIs in the combined 00 and 12 UTC data at Brest. Thus, the observed biases here at Decimomannu could also be random. During Pre- and Post-DIs the analysis deviates more from the observations than during DIs and Non-DIs, but those biases remain small and appear random. As previously mentioned, the larger variations during Pre- and Post-DIs are likely caused by the lower number of categories, since a median based on a higher number would probably smooth those variations.

Similar to the specific humidity profiles, the wind speed profiles during Non-DIs exhibit oscillating values in the innovation and residual below 1 km. At the surface both start with negative values, indicating a fast wind bias. Positive values centered around 300 m of approximately 0.5 m s^{-1} are observed for the innovation and reanalysis, followed by switch back to negative values at 0.5 – 1 km, before eventually both stay slightly positive above 1 km for the rest of the profile. The surface bias is visible with a similar extent during Post-DIs and with an even larger extent during DIs and Pre-DIs. However, this surface bias is not consistent with the measurements at Brest, since the observed surface biases of wind speed are opposed. In both cases the DI-related categories present the same bias at the surface as during normal conditions (Non-DIs), suggesting that station specific biases outweigh DI-related biases. Biases above the surface during DI-related categories follow basically the same pattern as described previously. During DIs the bias type mostly follows the Non-DI biases, but with larger innovation and residual values and more variability in the residual. Largest biases are found during Pre- and Post-DIs, for example a slow wind bias around 1.5 km mainly in the background and a fast wind bias during Pre-DIs at approximately 2.6 km, also mainly in the background. These biases are not observed in the combined 00 and 12 UTC data at Brest (not shown, only separated data at 00 UTC in Figure 4.23 and at 12 UTC in Figure 4.24), which could mean that they occur by chance.

Moreover, DI-related biases at the other ECMWF stations (not shown) are also not consistent with the ones observed here and instead often follow the bias distribution during Non-DIs, highlighting the key role of station specific biases. Possible DI-related biases are thus outweighed by station specific biases, indicating that DI-related biases are relatively small. In summary, the modification of the PBL during DIs is well represented by model data on average, whereby the analysis performs expectedly better than the background. Nonetheless, due to the elucidated high variability of DI impacts on the PBL at Brest, large and opposing biases could occur at different DI events that are not detected in the analyzed median. The averaging process probably smoothed occurring biases additionally, if they are located at varying altitudes as for instance temperature inversions. Therefore, future work could investigate model biases in individual DI case studies or analyze data of different models that have a less sophisticated data assimilation than the one from ECMWF.

5 Conclusions

This thesis employs a Lagrangian approach first created by Raveh-Rubin (2017) to identify DIs over western Europe from 3 January 1979 to 31 December 2022. Based on gridded DI outflow data, the DI frequency over western Europe is calculated. The influence of DIs on the vertical structure of the PBL is analyzed with radiosonde data from several stations across western Europe, with data from Meteo-France and ECMWF. The Meteo-France data encompasses the time period from 1 December 2016 to 31 December 2022 and the ECMWF data the time period from 1 December 2019 to 31 December 2022. Additionally, synop and ceilometer data are used to investigate DI variability in more detail at the station Brest. For this purpose, raw DI trajectory data are also utilized. Lastly, the observations during DIs are compared to global ECMWF model background and analysis data that are available in the ECMWF dataset. The key findings are summarized here based on the research questions posed in the introduction.

1. What is the climatological occurrence frequency of DIs over western Europe and how variable is it over different regions and seasons?

The average DI frequency over the time period from 3 January 1979 to 31 December 2022 exhibits a strong seasonality, with the maximum in winter and negligible DI frequencies in summer. January features the highest DI frequency overall, followed by December and February. Months adjacent to these winter months already display an obvious decline. Highest DI frequencies in winter are generally observed along the North Atlantic coastlines and over southern France, extending into the Mediterranean. Observed maxima at Cuneo-Levaldigi and east of Nimes-Courbessac could be caused by local wind phenomena due to topography, such as the Alpine foehn and the mistral, respectively. Seasonality in DI frequency over western Europe matches findings in literature (Stohl, 2001; Raveh-Rubin, 2017) and is generally in line with the seasonality of extratropical cyclones (Wernli and Schwierz, 2006), albeit with different locations and frequencies. The total number of identified DIs is higher than in other studies, such as Raveh-Rubin (2017), which is most likely caused by the difference in underlying wind data and thus a different starting grid for trajectories.

2. How is the PBL modified during the passage of DIs at Brest and how does it depend on the large-scale circulation?

DIs display a wide variety of characteristics and differing behaviour at the station Brest. This is exemplified in the case studies of the DI events associated with lowest specific humidity and highest wind speed at the surface at Brest.

The case study coupled with the lowest specific humidity reveals the connection of DIs with an anticyclone. The PBL response is therefore distinctly different than for typical DIs that are directly linked to cyclones over the Atlantic. While it features typical DI characteristics like enhanced surface heat fluxes, due to an intense cold and dry anomaly, the atmospheric stability remains stable to neutral. Contrary to typical DI modifications, the wind speed at the surface increases after the DI passage and the wind direction stays approximately constant at east-northeast, indicating the lack of a preceding cold front.

Aniticipated DI effects are observed in the first DI case study and the DI event with the highest observed wind speeds. Both DI events display potential instability, visible as a minimum in equivalent potential temperature and feature large changes in temperature, humidity and wind during the DI passage. Temperature and especially humidity both decrease at the occurrence of the DI. In combination with the highest precipitation, highest wind speeds and a wind direction shift shortly before the DI arrival, those variable evolutions show that both DI events are preceded by a cold front. However, the DI event with the highest wind speeds features almost no temperature inversions in the radiosonde observations above the surface, contrary to the first DI case study on 20 February 2020.

Further differences are observed in the variables traced along the DI trajectories, as the strongest surface fluxes in the different analyzed DI events occur at varying relative times with different intensity. Those differences are difficult to explain, because the exact surface conditions are unknown, since the other variables are only traced at the height of the trajectories. The trajectory data reveal large variability in all variables, even among the individual DI trajectories of one coherent DI event. This variability stems mainly from the differing position and vertical location of each trajectory.

Average vertical profiles at Brest show that DIs feature a cold, dry anomaly in comparison to Non-DIs. They also exhibit a well-mixed PBL with potential instability. Post-DIs generally indicate a recovery to Non-DI conditions. On the other hand, a higher humidity is observed during Pre-DIs and this class is also associated with the highest wind speed at the surface. Remarkably, the wind direction shift during DIs observed in two of the case studies is also visible in the average radiosonde profiles at 500 m height. Separation of radiosonde ascents in 00 and 12 UTC reveals surface inversions in all classes except Pre-DIs at 00 UTC, due to enhanced wind speeds during Pre-DIs that prevent the formation of a temperature inversion at the surface. The fact that a temperature inversion at the surface is also observed during DIs is notable and suggests that DI effects are superimposed by diurnal PBL variations.

3. How does the DI influence on the PBL vary across different regions in western Europe?

The typical DI characteristics, such as a well-mixed PBL, potential instability and a cold and dry anomaly are observed at most other stations, though with varying strength. The cold anomaly is usually most pronounced between 1 and 3 km, whereas the dry anomaly extends to the surface. Many other stations feature nightly temperature inversions at the surface like Brest, but none show such inversions at noon, suggesting that the diurnal cycle of the PBL often overrides the effect of the DI.

The DI characteristics at each station differ slightly due to local wind flow influences. This is

well illustrated at the stations Nimes-Courbessac and Cuneo-Levaldigi. The wind influence may lead to a higher DI frequency in the case of Nimes-Courbessac due to the mistral wind, without losing typical DI characteristics. However, this is not the case for Cuneo-Levaldigi, as the DI-related categories exhibit a unique warm anomaly in the lowest 1.5 km. A possible explanation for this might be that the Alpine foehn generates additional DIs or modifies existing DIs correspondingly. In contrast to Ilotoviz et al. (2021), no large temperature inversions at the top of the PBL are observed at the considered stations. On the one hand this could be caused by the averaging process due to averaging inversions at different heights but on the other hand this could be a real dynamical difference, as the DI event with the highest wind speeds reveals (Figure 4.18). One reason for the existence of such pronounced inversions may be the influence of anticyclones, as assumed in section 4.4.

4. Is the modification of the PBL during DIs accurately represented in numerical weather prediction models or can systematic biases be identified?

The structure of deviations between observations and model data during DI-related classes follows often the same pattern as during Non-DIs. This indicates that the station specific bias generally outweighs any biases during DI passages. However, even those station inherent biases are in general not particularly large. Since the model data is based on the global ECMWF model with a coarse horizontal resolution of 9 km, such station biases are bound to happen. As expected, the analysis matches the observations usually much better than the background. Other than that, no systematic differences can be identified in the background or the analysis and the modification of the PBL during DIs is therefore well represented by global ECMWF model data on average.

Overall, the employed DI definition scheme yields coherent, typical DI characteristics in the PBL at almost all stations with varying strength. However, the identified DIs demonstrate a large variability which could obscure the observed average signals. The largest variability stems from the fact that the employed DI identification scheme also recognizes DIs that are dominated by anticyclonic flow conditions, which was unknown before this study, leading to a distinctly different PBL response. These results underline the importance of analyzing individual DI events, as those yield much clearer signals than the averaging approach. For this purpose, the already planned, detailed synop and ceilometer measurements during NAWDIC are useful. Furthermore, this thesis provides DI frequencies over western Europe as part of preparatory work for the NAWDIC campaign and finds suitable locations for ground-based measurements along the North Atlantic coastline, since they feature both relatively high DI frequencies and an environment that is mostly undisturbed by topography. Thus, the continental influence on DIs that NAWDIC aims to analyze is minimal, since those DIs are associated with extratropical cyclones coming from the North Atlantic.

Future research could group identified DIs according to different criterions such as anticyclonic or cyclonic trajectory curvature to explore the varying PBL responses of those different groups quantitatively. Another criterion could be based on the potential temperature that is traced along the DI trajectories. As the DI case studies revealed, the potential temperature increases along some trajectories during the ascent before the 48 h descending period, suggesting diabatic heating that

could indicate the position of trajectories inside a warm conveyor belt. Based on the dynamical phenomenon to be analyzed, those criterions could filter out other identified DIs that do not belong to the desired group, thereby reducing variability and perhaps yielding clearer signals in the PBL response. However, the DI case studies unveil large variabilities already in a coherent DI trajectory set of one event and a sharp time dependence of the most notable PBL modifications during the cold front and DI passage. This highlights the value of DI case studies, since large DI composites may blur clear DI signals in the PBL.

Additionally, it could be investigated if there are visible biases in model data for individual DI events, perhaps also with higher resolution model data. One approach to eliminate the prevailing station biases might be to calculate the differences between model data and observation for the whole averaged dataset and subtract those from the differences during the individual categories. Another interesting aspect would be the examination of model data from other global models with a less sophisticated data assimilation than the one from ECMWF.

Bibliography

- Bell, B., and Coauthors, 2021: The era5 global reanalysis: Preliminary extension to 1950. *Quarterly Journal of the Royal Meteorological Society*, **147** (741), 4186–4227, <https://doi.org/https://doi.org/10.1002/qj.4174>.
- Bolton, D., 1980: The computation of equivalent potential temperature. *Monthly Weather Review*, **108** (7), 1046 – 1053, [https://doi.org/10.1175/1520-0493\(1980\)108<1046:TCOEPT>2.0.CO;2](https://doi.org/10.1175/1520-0493(1980)108<1046:TCOEPT>2.0.CO;2).
- Bouttier, F., and P. Courtier, 2002: Data assimilation concepts and methods march 1999. *Meteorological training course lecture series. ECMWF*, **718**, 59, URL https://twister.caps.ou.edu/OBAN2019/Assim_concepts.pdf.
- Browning, K. A., 1993: Evolution of a mesoscale upper tropospheric vorticity maximum and comma cloud from a cloud-free two-dimensional potential vorticity anomaly. *Quarterly Journal of the Royal Meteorological Society*, **119** (513), 883–906, <https://doi.org/https://doi.org/10.1002/qj.49711951302>.
- Browning, K. A., 1997: The dry intrusion perspective of extra-tropical cyclone development. *Meteorological Applications*, **4**, 317–324, <https://doi.org/10.1017/S1350482797000613>.
- Browning, K. A., and B. W. Golding, 1995: Mesoscale aspects of a dry intrusion within a vigorous cyclone. *Quarterly Journal of the Royal Meteorological Society*, **121** (523), 463–493, <https://doi.org/https://doi.org/10.1002/qj.49712152302>.
- Browning, K. A., and R. Reynolds, 1994: Diagnostic study of a narrow cold-frontal rainband and severe winds associated with a stratospheric intrusion. *Quarterly Journal of the Royal Meteorological Society*, **120** (516), 235–257, <https://doi.org/https://doi.org/10.1002/qj.49712051602>.
- Browning, K. A., and N. M. Roberts, 1994: Structure of a frontal cyclone. *Quarterly Journal of the Royal Meteorological Society*, **120** (520), 1535–1557, <https://doi.org/https://doi.org/10.1002/qj.49712052006>.
- Cao, N., C. Zhu, Y. Kai, and P. Yan, 2013: A method of background noise reduction in lidar data. *Appl. Phys. B*, **113**, 115 – 123, <https://doi.org/https://doi.org/10.1007/s00340-013-5447-9>.
- Carlson, T. N., 1980: Airflow through midlatitude cyclones and the comma cloud pattern. *Monthly Weather Review*, **108** (10), 1498 – 1509, [https://doi.org/https://doi.org/10.1175/1520-0493\(1980\)108<1498:ATMCAT>2.0.CO;2](https://doi.org/https://doi.org/10.1175/1520-0493(1980)108<1498:ATMCAT>2.0.CO;2).
- Carr, F. H., and J. P. Millard, 1985: A composite study of comma clouds and their association with severe weather over the great plains. *Monthly Weather Review*, **113** (3), 370 – 387, [https://doi.org/https://doi.org/10.1175/1520-0493\(1985\)113<0370:ACSOCC>2.0.CO;2](https://doi.org/https://doi.org/10.1175/1520-0493(1985)113<0370:ACSOCC>2.0.CO;2).
- Catto, J. L., and S. Raveh-Rubin, 2019: Climatology and dynamics of the link between dry intrusions and cold fronts during winter. part i: global climatology. *Climate Dynamics*, **53**, 1873–1892, <https://doi.org/https://doi.org/10.1007/s00382-019-04745-w>.

- Centre for Environmental Data Analysis (CEDA), 2023: Eumetnet e-profile. URL https://data.ceda.ac.uk/badc/eprofile/data/france/brest/meteofrance-vaisala-cl31_B, last accessed: 15-10-2023.
- Danielsen, E., 1964: Project springfield report. URL <https://apps.dtic.mil/sti/citations/AD0607980>.
- Danielsen, E. F., 1968: Stratospheric-tropospheric exchange based on radioactivity, ozone and potential vorticity. *Journal of Atmospheric Sciences*, **25** (3), 502 – 518, [https://doi.org/https://doi.org/10.1175/1520-0469\(1968\)025<0502:STEBOR>2.0.CO;2](https://doi.org/https://doi.org/10.1175/1520-0469(1968)025<0502:STEBOR>2.0.CO;2).
- Dee, D. P., and Coauthors, 2011: The era-interim reanalysis: configuration and performance of the data assimilation system. *Quarterly Journal of the Royal Meteorological Society*, **137** (656), 553–597, <https://doi.org/https://doi.org/10.1002/qj.828>.
- Deutscher Wetterdienst, 2020: Dwd-bodenanalyse. URL https://www.wetter3.de/archiv_gfs_dt.html, last accessed: 15-01-2024.
- Drechsel, S., and G. J. Mayr, 2008: Objective forecasting of foehn winds for a subgrid-scale alpine valley. *Weather and Forecasting*, **23** (2), 205 – 218, <https://doi.org/https://doi.org/10.1175/2007WAF2006021.1>.
- ECMWF, 2023a: Changes to the forecasting system. URL <https://confluence.ecmwf.int/display/FCST/Changes+to+the+forecasting+system>, last accessed: 03-01-2024.
- ECMWF, 2023b: Ifs documentation. URL <https://www.ecmwf.int/en/publications/ifs-documentation>, last accessed: 03-01-2024.
- Emeis, S., K. Schäfer, and C. Münkel, 2009: Observation of the structure of the urban boundary layer with different ceilometers and validation by rass data. *Meteorologische Zeitschrift*, **18** (2), 149–154, <https://doi.org/10.1127/0941-2948/2009/0365>.
- Gao, S., S. Yang, and B. Chen, 2010: Diagnostic analyses of dry intrusion and nonuniformly saturated instability during a rainfall event. *Journal of Geophysical Research: Atmospheres*, **115** (D2), <https://doi.org/https://doi.org/10.1029/2009JD012467>.
- Givon, Y., D. Keller Jr., V. Silverman, R. Pennel, P. Drobinski, and S. Raveh-Rubin, 2021: Large-scale drivers of the mistral wind: link to rossby wave life cycles and seasonal variability. *Weather and Climate Dynamics*, **2** (3), 609–630, <https://doi.org/10.5194/wcd-2-609-2021>.
- González-Alemán, J. J., C. M. Grams, B. Ayarzagüena, P. Zurita-Gotor, D. I. V. Domeisen, I. Gómara, B. Rodríguez-Fonseca, and F. Vitart, 2022: Tropospheric role in the predictability of the surface impact of the 2018 sudden stratospheric warming event. *Geophysical Research Letters*, **49** (1), e2021GL095464, <https://doi.org/https://doi.org/10.1029/2021GL095464>.
- Grams, C., J. Quinting, S. Raveh-Rubin, and A. Schäfler, 2021: North atlantic waveguide, dry intrusion, and downstream impact campaign (nawdic). international science plan. URL <https://internal.wavestowweather.de/campaign/projects/nawdic/wiki>.
- Ilotoviz, E., V. P. Ghate, and S. Raveh-Rubin, 2021: The impact of slantwise descending dry intrusions on the marine boundary layer and air-sea interface over the arm eastern north atlantic site. *Journal of Geophysical Research: Atmospheres*, **126** (4), e2020JD033879, <https://doi.org/https://doi.org/10.1029/2020JD033879>.
- Itoh, H., and Y. Narazaki, 2016: Fast descent routes from within or near the stratosphere to the surface at fukuoka, japan, studied using ^{7}Be measurements and trajectory calculations. *Atmospheric Chemistry and Physics*, **16** (10), 6241–6261, <https://doi.org/10.5194/acp-16-6241-2016>.

- James, R. P., and J. H. E. Clark, 2003: The diagnosis of vertical motion within dry intrusions. *Weather and Forecasting*, **18** (5), 825 – 835, [https://doi.org/https://doi.org/10.1175/1520-0434\(2003\)018<0825:TDOVMW>2.0.CO;2](https://doi.org/https://doi.org/10.1175/1520-0434(2003)018<0825:TDOVMW>2.0.CO;2).
- Kachelmann GmbH, 2020: Satellite water vapor. URL <https://meteologix.com/uk/satellite/europe/satellite-water-vapor-15min/20200220-1530z.html>, last accessed: 2023-12-05.
- Kotthaus, S., E. O'Connor, C. Münkel, C. Charlton-Perez, M. Haeffelin, A. M. Gabey, and C. S. B. Grimmond, 2016: Recommendations for processing atmospheric attenuated backscatter profiles from vaisala cl31 ceilometers. *Atmospheric Measurement Techniques*, **9** (8), 3769–3791, <https://doi.org/10.5194/amt-9-3769-2016>.
- Krüger, K., A. Schäfler, M. Weissmann, and G. C. Craig, 2023: Influence of radiosonde observations on the sharpness and altitude of the midlatitude tropopause in the ecmwf ifs. *EGUsphere*, **2023**, 1–28, <https://doi.org/10.5194/egusphere-2023-2094>.
- Kurz, M., 1990: *Synoptische Meteorologie; Mit 189, häufig mehrteiligen Abbildungen im Text*. Selbstverlag des Deutschen Wetterdienstes.
- Lagouvardos, K., and V. Kotroni, 2000: Use of meteosat water-vapour images for the diagnosis of a vigorous stratospheric intrusion over the central mediterranean. *Meteorological Applications*, **7** (3), 205–210, <https://doi.org/https://doi.org/10.1017/S1350482700001596>.
- Langford, A. O., R. B. Pierce, and P. J. Schultz, 2015: Stratospheric intrusions, the santa ana winds, and wildland fires in southern california. *Geophysical Research Letters*, **42** (14), 6091–6097, <https://doi.org/https://doi.org/10.1002/2015GL064964>.
- Lee, X., 2018: *Fundamentals of boundary-layer meteorology*. Springer International Publishing.
- Lin, M., A. Fiore, L. Horowitz, A. Langford, S. Oltmans, D. Tarasick, and H. Rieder, 2015: Climate variability modulates western us ozone air quality in spring via deep stratospheric intrusions. *Nature Communications*, **6** (7105), <https://doi.org/https://doi.org/10.1038/ncomms8105>.
- McGrath-Spangler, E. L., and A. S. Denning, 2013: Global seasonal variations of midday planetary boundary layer depth from calipso space-borne lidar. *Journal of Geophysical Research: Atmospheres*, **118** (3), 1226–1233, <https://doi.org/https://doi.org/10.1002/jgrd.50198>.
- Medeiros, B., A. Hall, and B. Stevens, 2005: What controls the mean depth of the pbl? *Journal of Climate*, **18** (16), 3157 – 3172, <https://doi.org/https://doi.org/10.1175/JCLI3417.1>.
- Meteo-France, 2023: Altitude observations (radiosondes). URL https://donneespubliques.meteofrance.fr/?fond=produit&id_produit=97&id_rubrique=33, last accessed: 15-10-2023.
- Mills, G., 2008: Abrupt surface drying and fire weather part 2: A preliminary synoptic climatology in the forested areas of southern australia. *Australian Meteorological Magazine*, **57**, URL <http://www.bom.gov.au/jshess/docs/2008/mills2.pdf>.
- Münkel, C., N. Eresmaa, J. Räsänen, and A. Karppinen, 2007: Retrieval of mixing height and dust concentration with lidar ceilometer. *Boundary-Layer Meteorology*, **124**, 117 – 128, <https://doi.org/10.1007/s10546-006-9103-3>.
- NAWDIC planning wiki, 2021: URL <https://internal.wavestoweather.de/campaign/projects/nawdic/wiki>, last accessed: November 27, 2023.

- NOAA, National Centers for Environmental Information, 2018a: Federal climate complex data documentation for integrated surface data (isd). URL <https://www.ncei.noaa.gov/data/global-hourly/doc/isd-format-document.pdf>.
- NOAA, National Centers for Environmental Information, 2018b: Global hourly - integrated surface database (isd). URL <https://www.ncei.noaa.gov/products/land-based-station/integrated-surface-database>, last accessed: 15-10-2023.
- Pollina, J. B., B. A. Colle, and J. J. Charney, 2013: Climatology and meteorological evolution of major wildfire events over the northeast united states. *Weather and Forecasting*, **28** (1), 175 – 193, [https://doi.org/https://doi.org/10.1175/WAF-D-12-00009.1](https://doi.org/10.1175/WAF-D-12-00009.1).
- Raveh-Rubin, S., 2017: Dry intrusions: Lagrangian climatology and dynamical impact on the planetary boundary layer. *Journal of Climate*, **30** (2), 6661–6682, <https://doi.org/10.1175/JCLI-D-16-0782.1>.
- Raveh-Rubin, S., and J. L. Catto, 2019: Climatology and dynamics of the link between dry intrusions and cold fronts during winter. part ii: Front-centred perspective. *Climate Dynamics*, **53**, 1893–1909, [https://doi.org/https://doi.org/10.1007/s00382-019-04793-2](https://doi.org/10.1007/s00382-019-04793-2).
- Raveh-Rubin, S., and H. Wernli, 2016: Large-scale wind and precipitation extremes in the mediterranean: dynamical aspects of five selected cyclone events. *Quarterly Journal of the Royal Meteorological Society*, **142** (701), 3097–3114, [https://doi.org/https://doi.org/10.1002/qj.2891](https://doi.org/10.1002/qj.2891).
- Reed, R., 1955: A study of a characteristic tpye of upper-level frontogenesis. *Journal of Atmospheric Sciences*, **12** (3), 226–237, [https://doi.org/10.1175/1520-0469\(1955\)0122.0.CO;2](https://doi.org/10.1175/1520-0469(1955)0122.0.CO;2).
- Reed, R., and E. Danielsen, 1958: Fronts in the vicinity of the tropopause. *Arch. Met. Geoph. Biokl. A.*, **11**, 1 – 17, <https://doi.org/10.1007/BF02247637>.
- Roca, R., J.-P. Lafore, C. Piriou, and J.-L. Redelsperger, 2005: Extratropical dry-air intrusions into the west african monsoon midtroposphere: An important factor for the convective activity over the sahel. *Journal of the Atmospheric Sciences*, **62** (2), 390 – 407, [https://doi.org/https://doi.org/10.1175/JAS-3366.1](https://doi.org/10.1175/JAS-3366.1).
- Rodgers, D. M., M. J. Magnano, and J. H. Arns, 1985: Mesoscale convective complexes over the united states during 1983. *Monthly Weather Review*, **113** (5), 888–901, [https://doi.org/10.1175/1520-0493\(1985\)1132.0.CO;2](https://doi.org/10.1175/1520-0493(1985)1132.0.CO;2).
- Savijärvi, H., 2006: Radiative and turbulent heating rates in the clear-air boundary layer. *Quarterly Journal of the Royal Meteorological Society*, **132** (614), 147–161, [https://doi.org/https://doi.org/10.1256/qj.05.61](https://doi.org/10.1256/qj.05.61).
- Sprenger, M., and H. Wernli, 2015: The lagranto lagrangian analysis tool – version 2.0. *Geoscientific Model Development*, **8** (8), 2569–2586, <https://doi.org/10.5194/gmd-8-2569-2015>.
- Steyn, D. G., M. Baldi, and R. M. Hoff, 1999: The detection of mixed layer depth and entrainment zone thickness from lidar backscatter profiles. *Journal of Atmospheric and Oceanic Technology*, **16** (7), 953 – 959, [https://doi.org/https://doi.org/10.1175/1520-0426\(1999\)016<0953:TDOMLD>2.0.CO;2](https://doi.org/10.1175/1520-0426(1999)016<0953:TDOMLD>2.0.CO;2).
- Stohl, A., 2001: A 1-year lagrangian “climatology” of airstreams in the northern hemisphere troposphere and lowermost stratosphere. *Journal of Geophysical Research: Atmospheres*, **106** (D7), 7263–7279, [https://doi.org/https://doi.org/10.1029/2000JD900570](https://doi.org/10.1029/2000JD900570).

- Stohl, A., and Coauthors, 2000: The influence of stratospheric intrusions on alpine ozone concentrations. *Atmospheric Environment*, **34** (9), 1323–1354, [https://doi.org/https://doi.org/10.1016/S1352-2310\(99\)00320-9](https://doi.org/https://doi.org/10.1016/S1352-2310(99)00320-9).
- Stull, R. B., 1988: *An introduction to boundary layer meteorology*. Kluwer Academic Publishers.
- von Engeln, A., and J. Teixeira, 2013: A planetary boundary layer height climatology derived from ecmwf reanalysis data. *Journal of Climate*, **26** (17), 6575 – 6590, <https://doi.org/https://doi.org/10.1175/JCLI-D-12-00385.1>.
- Škerlak, B., M. Sprenger, and H. Wernli, 2014: A global climatology of stratosphere–troposphere exchange using the era-interim data set from 1979 to 2011. *Atmospheric Chemistry and Physics*, **14** (2), 913–937, <https://doi.org/10.5194/acp-14-913-2014>.
- Wernli, H., 1997: A lagrangian-based analysis of extratropical cyclones. ii: A detailed case-study. *Quarterly Journal of the Royal Meteorological Society*, **123** (542), 1677–1706, <https://doi.org/https://doi.org/10.1002/qj.49712354211>.
- Wernli, H., and H. C. Davies, 1997: A lagrangian-based analysis of extratropical cyclones. i: The method and some applications. *Quarterly Journal of the Royal Meteorological Society*, **123** (538), 467–489, <https://doi.org/https://doi.org/10.1002/qj.49712353811>.
- Wernli, H., and C. Schwierz, 2006: Surface cyclones in the era-40 dataset (1958–2001). part i: Novel identification method and global climatology. *Journal of the Atmospheric Sciences*, **63** (10), 2486–2507, <https://doi.org/https://doi.org/10.1175/JAS3766.1>.
- Wood, R., and Coauthors, 2015: Clouds, aerosols, and precipitation in the marine boundary layer: An arm mobile facility deployment. *Bulletin of the American Meteorological Society*, **96** (3), 419 – 440, <https://doi.org/https://doi.org/10.1175/BAMS-D-13-00180.1>.
- Yang Shuai, C. X., and R. Lingkun, 2009: Analyses of dry intrusion and instability during a heavy rainfall event that occurred in northern china. *Atmospheric and Oceanic Science Letters*, **2** (2), 108–112, <https://doi.org/10.1080/16742834.2009.11446779>.
- Young, M. V., G. A. Monk, and K. A. Browning, 1987: Interpretation of satellite imagery of a rapidly deepening cyclone. *Quarterly Journal of the Royal Meteorological Society*, **113** (478), 1089–1115, <https://doi.org/https://doi.org/10.1002/qj.49711347803>.

Acknowledgments

I would like to express my deepest gratitude to my supervisor Julian Quinting for his excellent support during the whole Master's thesis. Whether it was help at the first data analysis steps, specific questions about the topic or just general guidance, I could always count on you. Thank you!

For providing me the DI data I want to thank Shira Raveh-Rubin. Thank you also for your help with upcoming questions about this data. In addition, I want to thank David Lavers for sending me the ECMWF radiosonde data.

Moreover, I would like to thank my co-supervisor Peter Knippertz for his valuable feedback when I presented my work. I am also grateful to Christian Grams, who was my initial supervisor and gave me important advice during the first phase of my Master's thesis.

I want to thank the members of our working group for the valuable discussion, feedback and advice. For the presentation and subsequent discussion of model biases during DIs at a station in the Azores, I want to thank Andreas Schäfler. I am also grateful to the members of our NAWDIC meetings at IMK-TRO for discussion and feedback.

Finally, I would like to express my profound gratitude to my parents for their unwavering support and their belief in me.

Erklärung

Ich versichere wahrheitsgemäß, die Arbeit selbstständig verfasst, alle benutzten Hilfsmittel vollständig und genau angegeben und alles kenntlich gemacht zu haben, was aus Arbeiten anderer unverändert oder mit Abänderungen entnommen wurde sowie die Satzung des KIT zur Sicherung guter wissenschaftlicher Praxis in der jeweils gültigen Fassung beachtet zu haben.

Karlsruhe, den 30.01.2024

A handwritten signature in black ink, appearing to read "Christian Sperka". The signature is fluid and cursive, with some loops and variations in letter height.

(Christian Sperka)